SPECTROSCOPIC STUDY OF ACETYLENE AND HYDROGEN CYANIDE

HOIMONTI IMMACULATA ROZARIO
Master of Science, Mathematics, Jahangirnagar University, 2010
Bachelor of Science, Mathematics, Jahangirnagar University, 2009

A Thesis
Submitted to the School of Graduate Studies
of the University of Lethbridge
in Partial Fulfillment of the
Requirements for the Degree

MASTER OF SCIENCE

Department of Physics and Astronomy
University of Lethbridge
LETHBRIDGE, ALBERTA, CANADA

SPECTROSCOPIC STUDY OF ACETYLENE AND HYDROGEN CYANIDE

HOIMONTI IMMACULATA ROZARIO

Approved:

*	*Print Name*	*Signature*	*Date*
*	Dr. Adriana Predoi-Cross Supervisor		
*	Dr. Arundhati Dasgupta Committee Member		
*	Dr. Brant Billinghurst Committee Member		
*	Dr. Craig Coburn Chair, Thesis Examination Committee		

Abstract

High-resolution molecular spectroscopy has been used to study acetylene line parameters and emission spectra of hydrogen cyanide. All acetylene spectra were recorded in our laboratory at the University of Lethbridge using a 3-channel tuneable diode laser spectrometer. N_2-broadened line widths and N_2-pressure induced line shifts have been measured for transitions in the $\nu_1+\nu_3$ band of acetylene at seven temperatures in the range 213–333K to obtain the temperature dependences of broadening and shift coefficients. The Voigt and hard-collision line profile models were used to retrieve the line parameters.

The line-broadening and line-shift coefficients as well as their temperature-dependent parameters have been also evaluated theoretically, in the frame work of a semi-classical approach based on an exponential representation of the scattering operator, an intermolecular potential composed of electrostatic quadrupole–quadrupole and pairwise atom–atom interactions as well as on exact trajectories driven by an effective isotropic potential. The experimental results for both N_2-broadening and shifting show good agreement with the theoretical results.

We have studied the line intensities of the $1v^{l}_{2}0 \leftarrow 0v^{l}_{2}0$ band system from the HCN emission spectrum. The infrared emission spectrum of $H^{12}C^{14}N$ was measured at the Justus-Liebig University, Giessen, Germany. The emission spectrum was analyzed with the spectrum analysis software Symath running using Mathematica as a platform. This approach allowed us to retrieve information on band intensity parameters.

Acknowledgements

I would like to express my gratefulness to all who helped me accomplish this work. First of all, I would like to give my special thanks to my supervisor Dr. Adriana Predoi-Cross for giving me this opportunity and accepting me to be a part of her workgroup. I am very grateful to her for the help, encouragement and being supportive to me. She has been a very good supervisor.

I was very lucky to work with Dr. Georg Mellau who was my research supervisor during the internship that I did in Germany from May to August, 2012. He was very helpful in improving my knowledge with scientific information. I am thankful to him for all his help.

My thanks go to both my committee members, Dr. Arundhati Dasgupta and Dr. Brant Billinghurst. They have been always interested in my research progress.

I am very thankful to Chad Povey, a PhD student in the Department of Physics and Astronomy, University of Lethbridge, for all the help and technical support, sharing his ideas and knowledge on spectroscopy. I would like to thank Jolene Garber, an undergraduate summer student, for assisting in my research work. I am also thankful to Dr. Jeanna Buldyreva who helped me with the of theoretical calculations. I want to thank all the co-authors of my journal paper published in Molecular Physics 2012 which is included as a chapter in this thesis. Last but not least, I want to thank my family for their support and love, and friends for the encouragement.

This study was conducted within the Alberta Terrestrial Imaging Center (ATIC) of the University of Lethbridge and supported primarily by the Natural Sciences and

Engineering Research Council of Canada's (NSERC's) Collaborative Research and Training Experience (CREATE) Advanced Methods, Education and Training in Hyperspectral Science and Technology (AMETHYST) program and the University of Lethbridge.

Contents

List of Figures

List of Tables

1 Introduction

Molecular structure and dynamics are an important branch of physics. Spectroscopic studies reveal the characteristics of molecules present in the atmosphere of Earth and other planets. High resolution molecular spectroscopy is the study of the structure and spectra of molecules of practical importance to the environment, astronomy, and fundamental science by examining the frequencies of light that these molecules absorb and emit. Infrared (IR) remote sensing has long been used to learn about the composition and structure of planetary atmospheres [1].

Laboratory-based high-resolution molecular spectroscopy is a sophisticated tool for obtaining highly accurate information on the intrinsic properties of gas phase molecules as well as properties resulting from the interaction between molecules. The measured data render possible the analysis of molecular spectra in environments such as the upper layers of the terrestrial atmosphere, interstellar space, the atmospheres of comets and cool stars. Science Advisory Groups for the spectroscopic remote sensing missions have strongly recommended that new laboratory studies using the best experimental techniques and/or sophisticated theoretical models are required. In order to supply laboratory/theoretical data required for the accurate retrieval of the concentration profiles, accurate measurements of absolute line positions and intensities for molecules of atmospheric relevance have to be undertaken.

An important result of laboratory spectroscopic research is the compilation of spectroscopic databases (HITRAN[1], GEISA[2]) containing information about spectral line positions, intensities and line shapes, aimed at facilitating the analysis of spectra from remote environments. Ongoing technological developments produce remote spectra of increasingly higher quality. Analysis and interpretation of these improved remote spectra call for a substantial increase in the amount and quality of spectroscopic database information.

The recent launch of infrared space missions draws specific attention to the vibrational bands of trace gas atmospheric constituents. These instruments cover wide spectral ranges at high spectral resolutions with excellent signal-to-noise ratios. As a consequence, the accuracy of the analysis of the corresponding atmospheric spectra performed to retrieve the concentration profiles depends highly on the quality of the spectroscopic parameters, such as line positions and intensities. IR spectroscopy employs the IR region of the electromagnetic spectrum which is particularly useful for distinguishing atmospheric trace gases [2]. Pressure broadening of acetylene of the $\mathbf{\nu_1+\nu_3}$ (ν is a vibrational quantum number) band located in the 1550 nm region was first observed in 1960 [3].

Acetylene is a gas molecule present as a trace constituent in the atmospheres of Earth, the giant planets and of Titan. Acetylene has been found in trace amounts in stellar atmospheres and also interstellar medium. This molecule is a reactant as well as a product of chemical reactions in the Earth atmosphere. Moreover, being stable, simple, and light,

[1] High Resolution Transmission
[2] Gestion et Etude des Informations Spectroscopiques Atmosphériques

C_2H_2 becomes an object of study needed to understand complex intra-molecular mechanisms of larger species in organic and physical chemistry. It is an ideal target subject to interpret macroscopic properties at the microscopic level in order to describe quantum mechanics models, and to produce reliable spectroscopic data [4].

Due to its importance, many experimental techniques are used to study and monitor acetylene. Laboratory studies are required to guarantee that accurate information on this molecule is available for remote applications and to properly interpret aircraft, telescope and spacecraft observations. New high-quality laboratory spectra have to be recorded and analyzed at gas temperatures and pressure conditions as close as possible to those expected for the original gas source.

Based on the combined information from spectra obtained in the laboratory and those obtained directly from remote objects, the chemical composition of the remote environments, as well as other properties such as the temperature, can be determined. From such information, supplemented by the results of theoretical calculations performed in my lab, we can deepen our knowledge about molecular structures, the dynamical properties of molecules, and the pathways and energetics of molecular reactions. By using the intense and highly collimated light from a laser source, we can record spectra with an astonishingly high signal-to-noise ratio in a relatively short time, and this advantage puts us currently in the best position in the world to acquire spectra with resolved rotational structure even from large molecules.

A wide variety of spectroscopic studies have been carried out to deduce spectral line parameters of acetylene self-broadening and broadening by air and other gases (e.g.,

N_2 and O_2 for Titan and Earth atmosphere [2,5,6] and H_2 for Jupiter and Saturn [7-9]), using good models of spectral line shapes. The temperature dependencies of N_2 pressure broadening were also measured at low temperature in selected studies [5, 10-12].

1.1 Polyatomic Linear Molecules

Alkynes such as acetylene (C_2H_2) are hydrocarbons that contain one or more triple bonds per molecule. C_2H_2 is a polyatomic chemical compound of two carbon and two hydrogen atoms with a carbon-carbon triple bond. It is a linear molecule of four atoms with the following structure: H-C≡C-H. The bond length is 120 pm for CH and 106 pm for CC. The atoms are placed in a straight line.

Linear polyatomic molecules are either $D_{\infty h}$ or $D_{\infty h} = C_{\infty v}$ symmetry according to point group (character table is given in Table A.1 in Appendix A). For example, H-C-N is $C_{\infty v}$ symmetry. Hydrogen cyanide possesses 3N-5 = 4 vibrational modes, one of them with a doubly degenerate bending mode [13].

Acetylene was first discovered in 1936 and it had been known as a "*new carburet of hydrogen*" until a French chemist Marcellin Berthelot discovered, coined and named it as acetylene in 1960. On the basis of the triple point in the phase diagram, the melting point of acetylene at 1.27 atm is -80.8°C, acetylene can be found as liquid. At atmospheric pressure (1atm) acetylene sublimes at -84°C.

1.2 Review of Previous Line Shape Studies on Acetylene

The self-broadening coefficients of C_2H_2 lines have been studied experimentally and theoretically for different absorption bands. The first study on record of self-broadened

line parameters in acetylene was by Varanasi and Bangaru at 171 K, 200 K, 250 K and 295 K in the $\nu_1+\nu_3$ band of C_2H_2 at 1525 nm [14]. The self-broadening coefficients for 27 lines were first measured using the basic concept of two semi-classical impacts [15]. This experiment was carried out on the transitions in the P and R branches of the ν_5 band using a diode laser spectrometer. Self-broadened acetylene has been observed for the combination band $\nu_1+\nu_5$ in the infrared region of frequency 4091 cm^{-1} [16] and for the band $\nu_1+\nu_3$ infrared region of 1550 nm or 6451 cm^{-1} in frequency [10, 17]. A recent study [18] was focused on the transitions in the $\nu_1+\nu_{2+}\nu_4+\nu_5$ band of self-broadened C_2H_2 over a wide range of temperatures, and considered the effects of molecular speed dependence on broadening coefficients for the first time.

Transitions in different branches, such as P, Q and R branches, have frequently been used for the detection and quantitative measurement of trace species by utilizing the measurements of infrared vibration-rotation bands. Room temperature N_2 broadening measurements were performed in the P and R branches of the ν_5 band using a tunable diode-laser spectrometer and the Voigt profile [2, 7, 19, 20] also at low temperature for 22 lines using the Rautian profile [5]. The calculation of N_2 broadening coefficients have been theoretically shown for the Q branch of the $\nu_4+\nu_5-\nu_4$, $2\nu_5-\nu_5$ band [11, 21] and compared with experimental values for the P and R branches [5, 19, 20]. The measurement of 29 lines in the $\nu_4+\nu_5$ band of P and R branches were determined and modelled using the Voigt profile by V. Malathy Devi *et al*. [22] and the Rautian [12, 23] profile at 173.2 - 298 K. Foreign broadening by N_2 and Ar line parameters in the $\nu_1+\nu_5$ band were studied in [16] using tunable difference-frequency laser system and the profile model of Rautian.

Studies have been carried out in the combination $\nu_1+\nu_3$ band with the spectral profiles modelled by the Voigt [10, 24, 25], Rautian and Galatry [25] using cavity diode-laser system at 1.5μm [10, 24, 25]. This is a strong combination band of two fundamental bands typically used for near-infrared frequency calibration. The measurements were done with a spectrometer based on a semiconductor diode laser and with the technique of direct absorption spectroscopy [17]. Transitions in the P and R branches of $\nu_1+\nu_3$ band have been analyzed from the spectra obtained at room temperature [24, 25] and at low 195K or high 373K, 473K temperature. Spectra of $\nu_1+3\nu_3$ band of acetylene broadened by N_2, O_2, He, Ar, Ne, Kr and Xe were recorded at 298K using the Rautian (hard-collision) and Galatry (soft-collision) spectral model and a diode-laser system at 0.788μm [26]. Biswas *et al.* [27] implemented diode-laser spectroscopy to retrieve self- and nitrogen-broadening for transitions belonging to overtone $\nu_1+3\nu_3$ band located in the region of 782 cm^{-1}.

In a recent study, the authors were interested in pressure-induced line self-shift coefficients in the $\nu_1+\nu_2+\nu_4+\nu_5$ band of acetylene determined using the Voigt profile and speed dependent Voigt profile [18]. Pressure induced shifts have been previously measured [17, 24-26]. The authors have studied N_2-shifts in the $\nu_1+3\nu_3$ band [26] and in the $\nu_1+\nu_3$ band [17, 24, 25]; and self-shifts in the $\nu_1+\nu_3$ band [17, 25]. High resolution diode laser spectroscopy was used by N. T. Campbell *et al.* [10] to measure the pressure-induced self-shifts at 195 K, 373 K and 473 K for several transitions in the $\nu_1+\nu_3$ band. At elevated pressures there is a mechanism that produces line mixing effects and affects the retrieved pressure-induced line shifts.

1.3 Tunable Diode Laser Spectroscopy

Absorption spectroscopy in the infrared region plays an important role in atmospheric chemistry since most molecules have vibrational fundamentals in this region.

The semiconductor diode laser was first developed in 1962. A diode, or semiconductor, laser can operate in the infrared and in the visible region of the spectrum. According to the spectral region diode laser spectroscopy is divided into two categories, namely: i) *near-infrared* or *overtone* for room temperature operating diodes that emit in the spectral range below 2 μm and ii) *mid-infrared* for *fundamental* transitions for operation in the region from 3 μm to 25 μm. Transitions in mid-infrared are stronger than in near-infrared and the detector is sensitive in monitoring in this region that it allows the detection, identification, and measurement of trace gas molecules and atoms. Diode lasers performing in the infrared range can provide continuous wave (CW) radiation with an output power of about 100 μW whereas those operating in the near-infrared range can deliver up to tens of mW of optical power.

Most of the semiconductor diode lasers are constructed by following the p- and n-type properties of different semiconductor materials. Many optical structural designs have evolved such as AlGaAs[3], InGaAs[4], GaAlAs[5] and GaAlAsP. There are three advantages of using diode lasers, namely: i) line width, ii) unique combination of tunability, excellent power conversion efficiencies, small size, modulation capabilities, and iii) are excited by electric current to produce laser wavelength. VCSEL diode lasers, antimonite diode lasers,

[3] Aluminium gallium arsenide
[4] Indium gallium arsenide
[5] Gallium aluminum arsenide

lead salt diode lasers, grating-tuned external-cavity and monolithic tunable semiconductor lasers are some examples of diode lasers.

Laser spectroscopy can be used to improve our understanding of molecular structure in gas phase by rotation-vibration analysis; their dynamical behaviour; and analytical applications such as for example, spectroscopic remote sensing.

In this thesis, we will discuss the spectral line parameters of forty-seven transitions in the P and R branches of the $\nu_1+\nu_3$ band of acetylene broadened by nitrogen. The gas mixture has been selected to be 10% acetylene and 90% nitrogen. Line-shape simulations have been performed on the $\nu_1+\nu_3$ band using data obtained from the HITRAN database to determine both the pressure range as well as the lines that could be correctly measured. The spectra were recoded using a 3-channel tunable diode laser spectrometer described in detail in Chapter 3. The retrieved N_2-broadened widths, pressure-induced N_2-shifts over a range of temperature between 213 - 333 K and different pressures, the temperature dependencies of N_2 broadening and shifting coefficients are all part of the objective of this experimental work. Results obtained in molecular theoretical calculations will be compared with the values that were found experimentally.

1.4 Emission Spectroscopy in the Infrared Region (HCN)

HCN is a linear, polyatomic molecule considered as a quantum system [H, C, N] of 17 particles (^{1}H, ^{12}C, ^{14}N nuclei and 14 electrons). This molecular system is one of the most important model systems of molecular chemical physics as it possesses the largest number of accurately characterized rovibrational states [28]. By translation of the H atom from one side of the CN core to the other side of the hydrogen cyanide HCN transforms

into a chemically different molecule hydrogen isocyanide HNC. This H atom translation is the simplest chemical reaction and is called isomerisation. These atoms of the isomerisation process in the HCN → HNC reaction is one of the most studied model systems of uni-molecular reactions [29, 30].

The most successful studies on this system have been done using hot gas molecular spectroscopy. The high-temperature near-infrared (NIR) emission spectra of HCN and HNC allowed the determination up to very high J of the rotational manifold for all low lying vibrational combination states. The experimental data together with rovibrationally assigned *ab initio* data provide information about vibrational and rotational structure of HCN and HNC molecules up to the isomerisation [28, 31].

HCN has become the subject of many millimeter-wave laboratory measurements since it was discovered by accident in radio telescope observations of interstellar space. Two studies have been dedicated to the rotation-vibration spectrum of $H^{12}C^{15}N$ [31, 32] and *ab initio* calculations were used to predict the spectroscopic properties of the ground states. Rovibrational constants have been recorded for fifty states by Maki *et al*. [31]. After that twenty more states were added in a later paper [32]. In this thesis the emission spectra of hot band $H^{12}C^{14}N$ will be discussed in chapters 5.

2 Theoretical background

Molecular spectroscopy is the study of the interaction between molecules and electromagnetic radiation. Spectroscopy is a well-known and established field with a variety of scientific applications. A light source, a cell filled with sample gas and a detector unit are the main components of basic spectroscopic instruments.

At the microscopic level of molecular system, molecular energies are divided into four major components which can generate different types of spectra in different region of the electromagnetic spectrum. These components are rotational, vibrational, electronic and translational energies. For most molecules, the pure rotational absorption spectra in the microwave and far-infrared (FIR) region are the result of energy transitions between rotational levels in the same vibrational level. Vibrational-rotational spectra that appear mainly in the infrared region are the result of simultaneous energy transitions due to the vibrational and rotational motion of the molecule. Electronic spectra cover the visible and ultra-violet regions, which appears because of the transition in the electronic energy levels.

The rotational transitions between two different vibrational energy levels form branches in the spectra, and are organized in P-, Q- and R-branches. The rotational and vibrational energy states of the molecules are quantized; however, the translational energy is the external energy associated with the motion of the molecule and is not quantized.

2.1 Basic of Molecular Spectroscopy

By definition light is an "*electromagnetic radiation of any wavelength that travels in a vacuum with a speed of* 3×10^8 *m/s*". Starting from the radio waves (λ ~1 m), and then

microwave, infrared, visible, ultra-violet, x-ray, the electromagnetic spectrum ranges up to the gamma-rays (λ ~1×10^{-11} m). They occupy the different region of an electromagnetic spectra in the order of the increasing frequency (or wavenumber or energy) or decreasing wavelength. Electromagnetic waves propagate through a vacuum constructed by magnetic and electric components. The strength of the oscillating electric and the magnetic field components are denoted by $\vec{E}$ and $\vec{H}$, respectively. Figure 2.1 [33] shows the direction of the electric and magnetic fields that are at 90 degrees to each other and to the direction of propagation as periodic sinusoidal functions in time with the frequency ν [33]. The electric field is in the y-axis direction, the magnetic field is the z-axis direction and both are perpendicular to the x-axis.

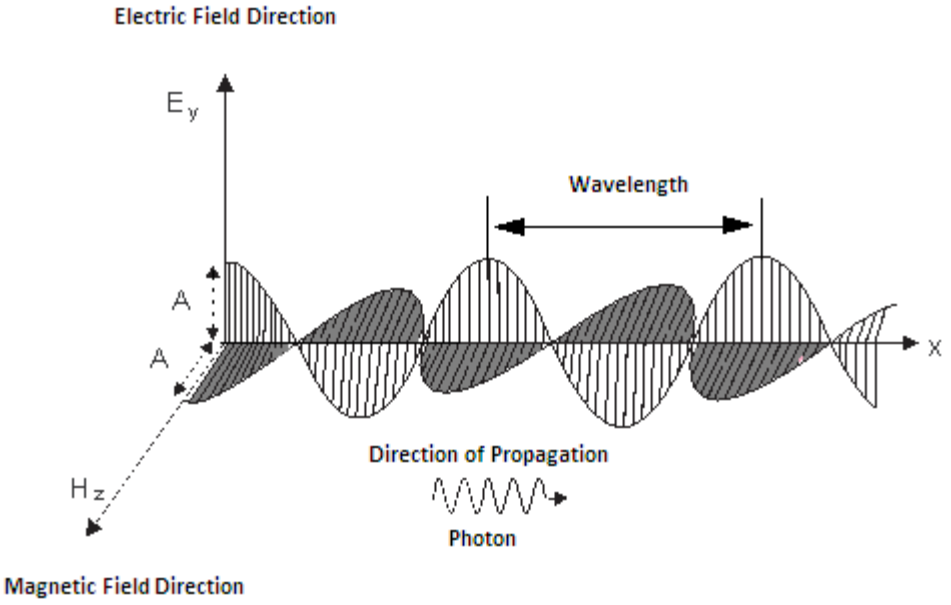

Figure 2.1: Electromagnetic radiation [33].

The electromagnetic wave (radiation) can be described by the following equations.

$$E_y = E_{y_0} Sin(2\pi\nu t - kx) \tag{2.1}$$

$$H_z = H_{z_0} Sin(2\pi\nu t - kx) \quad (2.2)$$

In the equation (2.1) and (2.2), E_{y_0} is the amplitude of $\overrightarrow{E}$ and H_{z_0} is the amplitude of $\overrightarrow{H}$ components of the electromagnetic wave [33]. Both equations represent a sinusoidal periodic function where ν is the frequency at time *t*, *x* is the position and *k* is the number of wave ($k = 2\pi/\lambda$).

The infrared region of the electromagnetic spectrum is the most important for the spectroscopic studies of linear polyatomic molecules. Linear polyatomic molecules, for example H-C≡C-H and H-C≡N shows vibrational-rotational spectra in the infrared region. The infrared range covers the near-infrared range (0.8 - 2.5 μm wavelength or 4000-14000 cm^{-1}) that is adjacent to the visible, the mid-infrared range (2.5 - 25 μm or 400-4000 cm^{-1}) and the far-infrared (2.5 - 1000 μm or 10-400 cm^{-1}) range that is adjacent to the microwave region. The relation between wavenumber (cm^{-1}) and frequency unit is $\tilde{\nu} = {}^{\nu}/_{c}$ (cm^{-1}). Micrometer (μm) is the unit of wavelength, which has an inverse relation with frequency, $\lambda = {}^{c}/_{\nu}$.

Base on the quantum mechanical theory, the interaction between matter and electromagnetic radiation can be described using a set of two quantum states energy level system. Electromagnetic radiation gets absorbed or emitted when interacting with matter by the transition between two energy levels (states) as shown in figure 2.2. Figure 2.2 shows a two level energy system where eigenenergies E_m belongs to the lower energy state *m* and E_n belongs to the upper energy state *n*. A photon absorbed at certain energy is proportional to the difference between the energy values of these two states. Let's consider

the energy difference is ΔE between the eigenenergies E_n and E_m, and the photon energy absorbed by the lower state m at frequency, v_{nm} (or wavenumber, $\tilde{\nu}_{nm}$) is $hc\tilde{\nu}_{nm}$,

$$\Delta E = E_n - E_m = hv_{nm} = hc\tilde{\nu}_{nm} \tag{2.3}$$

Where c is the speed of light with the value of 299792458 ms^{-1} and h is the Planck constant, $6{:}62606896\times10^{-34}$ Js.

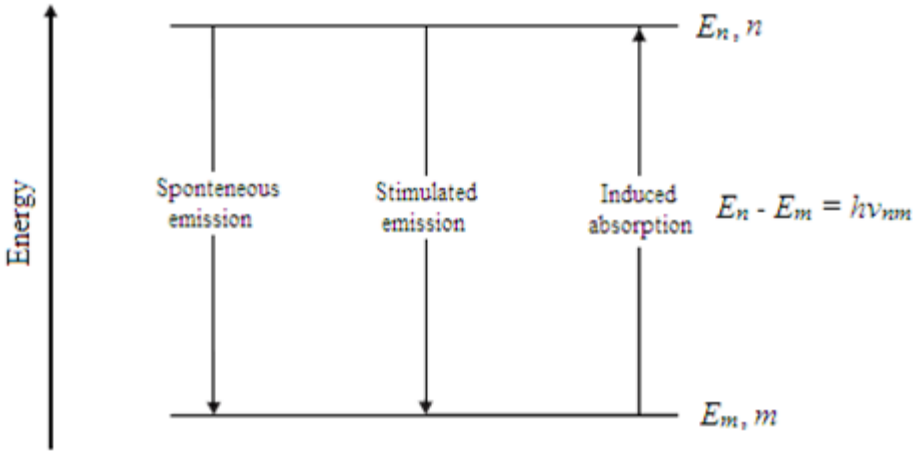

Figure 2.2: 1. Spontaneous emission, 2. stimulated emission, 3. induced absorption [13, 33].

The energy difference is equal to the absorption position multiplied by the two constant values c and h. A spectral transition occurs between two sets of quantized energy levels, restricted by selection rules. This absorption may take place in any region of the electromagnetic spectra. A molecule with a permanent dipole moment ($\mu \neq 0$) shows pure rotational spectra in the microwave region. The dipole moment of a molecule must change in order for a molecule to be active in the infrared region. Infrared spectroscopy studies the interaction of the infrared (IR) radiation and matter.

One of the following three possible processes may take place during the interaction of the electromagnetic radiation with this two state system [13, 33]. All three emissions and absorption processes that are described here must be taken into account while discussing the interaction of the electromagnetic radiation with matter.

Induced absorption: A photon is absorbed by the system in the lower state m and makes a transition to the excited state n.

Spontaneous emission: In the two-state system the initially excited state n spontaneously emits a photon of frequency v_{nm} and makes a transition to the lower state m.

Stimulated emission: A photon with frequency v_{nm} induces a transition from the excited state n to the lower eigenstate m. A second photon of frequency v_{nm} is emitted, which is coherent to the first photon.

2.2 The Theory of Spectral Line Shapes

An absorption/emission transition that appears in any experimental spectra is normally known as 'line'. The theory behind modeling and analysis of these lines fitted using mathematical line shape models will be discussed in this section. Several physical effects are considered when spectral data are fitted to a mathematical line shape, such as broadening (for example; natural broadening, Doppler broadening, pressure broadening) [13, 33], shifting and Dicke narrowing. Speed-dependent effect and line mixing are taken into account directly or indirectly when modeling the absorption or emission spectra. Collisional broadening and shifting are the most important effects. This section will also

discuss the dependency of the pressure broadening effect at various temperature conditions using the theoretical basis for the temperature scaling law.

2.2.1 Intensity of Spectral Lines

The intensity of any transition is related to the rate of absorption or emission at a given frequency, i.e the amount of energy which is absorbed or emitted per unit time. The intensity for any transition is equal to the number of transitions between two energy states per unit time multiplied by the energy of the transition. Intensity of spectral lines depends on the population of the lower state of a transition, the transition probability between these (lower and upper) two states and the transition moment square [13, 33]. The transition probability between two energy states depends on the relative population between the lower and the upper states. The transition dipole moment is a vector quantity that can be determined from the wavefucntions corresponding to the lower and the upper energy state and from the electric dipole moment.

$$R^{nm} = \int \Psi_n^* \boldsymbol{\mu} \Psi_m d\tau \tag{2.4}$$

where the electric dipole moment $\boldsymbol{\mu} = \sum_i q_i r_i$ is also a vector quantity; q_i and r_i are the charge and the position of the i^{th} particle. The transition intensity is proportional to the numerical square value of the transition moment. In absorption spectra, the intensity of absorbed lines depends on the sample path length and the gas concentration.

2.2.2 Natural Line Broadening

Natural broadening is a homogeneous line broadening that appears due to the fact that all excited states have a finite lifetime, even in the absorption line of isolated stationary molecules [13]. Having finite decay time (life time or the absorption time) of an excited

state n will result in a small spread in energy values. According to the Heisenberg uncertainty principle, $\tau \Delta E \geq \hbar$ [33], the frequency at which the absorption occurs, is actually a frequency distribution which can be known to a finite degree of accuracy. Consequently, the frequency distribution of energy levels give rise to the small line width. Due to the natural broadening effect the spectrum appears with very small measurable line width $\Delta\nu$, which is normally modeled using the Lorentzian line shape function.

The photon can be considered as "packets" of frequencies and wave trains of finite length around the line center because of the finite lifetime (finite time of absorption or emission process). Having a very small width, the natural line broadening is not expected to be as important as the other broadening effects in this experiment.

2.2.3 Doppler Broadening

The Doppler effect relates the motion, velocity and the temperature of the gas molecules. Atom or molecules that make up gases are in motion. According to the Doppler effect, when gas molecules are in motion relative to a fixed or moving light source (frame of reference), then the wavelength/frequency at which the absorption occurs is shifted (seen by an observer) and is not the same as the wavelength/frequency of the source. The frequency absorbed by a moving molecule is different than the wavelength of the source. Suppose that a source is emitting light waves of frequency ν_0 then the atoms/molecules moving towards or away from the light source will absorb at a lower or at a higher frequency than ν_0, respectively. So, a frequency shift will be observed in the absorption line position, and the shifting of the rest frequency will result in the line's being broadened.

Austrian scientist Christian Doppler has described this phenomenon in the 19th century and since then it is known as the Doppler effect.

The velocity of the molecules varies with the temperature of the gas. The Maxwell-Boltzman velocity distribution function describes these molecular velocity components and the distribution of absorption frequencies. In thermal equilibrium the Doppler half width at half maximum (HWHM) (figure 2.3), $\Delta\nu$ and the Doppler effect can be modeled using the Gaussian law in the line profile as [13, 34]:

$$\Delta\nu = \frac{2\nu_0\sqrt{8kTln2/m}}{c} \tag{2.5}$$

Here m is the mass of atom or molecule, T is the temperature of the gas, k is Boltzmann's constant, c is the speed of light and ν_0 is the centre position of the absorption line. It is clear from the above formula that the Doppler width has linear relation with temperature and wavenumber/frequency. The width increases if temperature increases and decreases if the temperature decreases, similarly for the frequency [33].

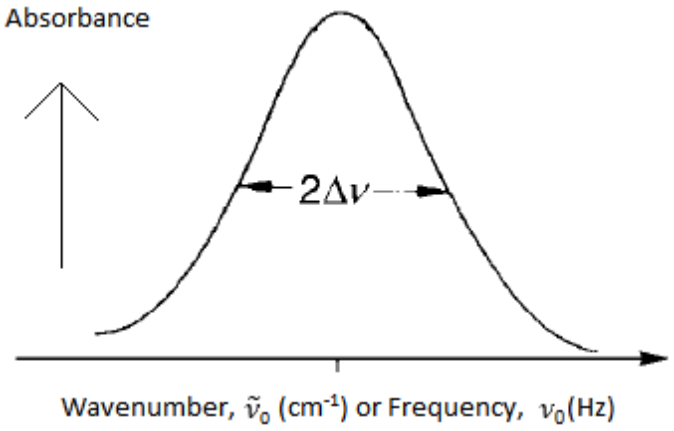

Figure 2.3: Absorption line with Doppler half width at half maximum (HWHM) [33]

Doppler broadening is expected to be higher than the natural line broadening and inhomogeneous. At high pressure and low temperatures, the Doppler broadening is not as important as the collisional broadening. However, the low-pressure spectra of room temperature reference cell show an exceptionally significant amount of Doppler broadening.

2.2.4 Collisional/Pressure Broadening and Shifting

Collisional broadening is also known as pressure broadening because it shows a linear relation with the pressure of the gas. Pressure broadening increases and decreases with increasing and decreasing pressure, respectively. A two level energy system is appropriate to explain the collisional effect because the elastic collision between two molecules ends up causing an exchange of energy [34], which in return cause broadening by the frequency spread (frequency distribution) that corresponds to the difference between the lower and upper energy level [33]. After the collision of the molecules the phase of the vibrational and rotational oscillating dipole moment of colliding molecules may remain altered and energy levels may not return to the same phase as it was before the collision but the energy levels go back to normal. Due to these collisional phase shifts, any constant frequency wave of random phase produces a frequency distribution when Fourier transformed into the frequency domain, therefore producing a frequency spread in the lower and upper energy level transitions and causing line shape broadening. In the case of collisional broadening, the radiative transitions can be discounted by assuming that the collision time is much smaller than the time between collisions. This assumption gives rise to an 'impact approximation' which expected to be 5 cm^{-1} of line centre for the present

experimental conditions. Also, by assuming that the radiative transition is very much quicker than the collision, so that the transitions can be considered to be instantaneous.

Molecular collision theories are studied and explained in detail using mathematical interpretation and lineshape models [35, 36]. The pressure shifting in the center of the line position is also a result of the abovementioned phase shifts. This shifting is also linearly related to the pressure. To understand mechanism of the collisional broadening and shifting is not as simple as the Doppler broadening since it depends on the interaction potentials of the colliding molecules and the nature of the collision process (elastic/inelastic). Thus, the mathematical description is much more complex. In the case of inelastic collision which can also be modeled using a Lorentzian profile [13], one needs to account for the non-radiative transition; non-radiative transitions occur because some of the collisional energy converts into internal energy.

2.2.5 Dicke Narrowing

The average velocity of molecules is sometimes reduced and becomes less than the speed of molecule because the total displacement of the molecule is less than the distance of travel. Generally, the mean free path of molecules moving in a straight line is sufficiently large when compared with the incident wavelength. During the lifetime of an excited molecular state and due to several collisions, this mean free path can become equal to or less than the transition wavelength of the molecule (wavelength of molecular transition), hence the molecular motion becomes Brownian. The smaller mean path and velocity creates a small amount of Doppler shift, and thus this reduces the width of broadening and causes narrowing. These effects affect the Doppler broadening only if the Doppler width is less than the pressure-broadened width. This effect is known as Dicke narrowing effect

[37]. One can observe this narrowing effect in the spectral line when the Doppler width becomes smaller than the pressure-broadened width. For infrared frequency region and low pressure regime, the Dicke narrowing effect exhibits this reduction effect on the Doppler broadening. In this experiment, the Dicke narrowing effect is expected to significantly decrease the Doppler width even though it is a very small effect; however, it will not effect the pressure broadening. A study by Povey *et al.* [38] reported Dicke narrowing coefficient for 20 transition in the *R*- branch of acetylene molecule.

2.2.6 Speed-Dependent Effects

Taking the speed dependent effect into account while modeling the line shape profile such as Lorentzian profile is important because the speed/velocity of the molecules affect the collisional broadening and shifting of the spectral lines. The theory of collisional broadening states that molecules must be classified into groups according to their speed in order to calculate/guess the average speed value, because the collision rate and the collision cross-section of colliding molecules are determined from these average speed values. After that the calculated collision rate and collision cross-section can be used for determining the collisional broadening and the Lorentzian width. Making an assumption of the molecular average speed in order to determine the Lorentzian width is a form of approximation. These speed classes are characterised using a Maxwellian Boltzman distribution function (thermal motion of gaseous molecules follows the Boltzman distribution law), and then calculate a profile for each class. On the other hand, molecules of one class may switch into another speed class due to the collisional changes in the molecular speed. Nevertheless, a weighted sum of Lorentzian profile can be applied to take the speed-dependent effect into account while calculating the broadening and line shifting parameters. A speed dependant

profile is given and described by Berman [39] in 1972. The speed dependence effects in the CO_2 molecule has been observed by Devi *et al.* [40, 41].

Normally, if the perturbing molecule is heavier than the active molecule then the speed-dependence is more important for the active molecule because the perturbing molecules can be assumed to be at rest. However, speed-dependence become unimportant if the active molecule is heavier than the perturber, so one assumes that the active molecule is nearly stationary. For our experimental line shape study of C_2H_2 broadened by N_2, the perturber mass and the mass of the active molecule are different than each other, so the effects of speed-dependence cannot be discounted.

2.2.7 Theory of The Temperature Dependence of Broadening Coefficients

Remote sensing applications always take into account some approximations or assumptions. The interpretation of remote measurements need these approximations because the natural atmospheric conditions are subject to be in consideration while predicting and calculating the line shapes of an absorption spectra. One of the main approximations is the temperature scaling law for pressure broadening coefficients because line parameters varies with the temperature. An approximate scaling law which is a function of the absolute temperature for the broadening coefficients was first developed by Birnbaum [42] and enlarged by Bonamy *et al.* [43]. The temperature scaling law for broadening coefficients for a mixture of two gases is given as:

$$\gamma(p,T) = p\left[\gamma^{o}_{foreign}(p_o,T_o)(1-\chi)\left[\frac{T_o}{T}\right]^{n_1} + \gamma^{o}_{Self}(p_o,T_o)\chi\left[\frac{T_o}{T}\right]^{n_2}\right] \tag{2.6}$$

where the power n_1 and n_2 are the temperature dependence exponent foreign $\gamma^{o}_{foreign}$ and self-broadening γ^{o}_{self} (at half-width). p_o = 1 atm and T_o =296 K are the reference pressure and temperature where $p = p_{foreign}+p_{self}$ is the total sample pressure and χ is the ratio of p_{self} to p. γ is the measured broadened half-width coefficients of the spectral line at the total gas pressure of p and at temperature T.

Two types of theories are followed while deriving the temperature scaling law. The first one is a simple kinetics argument and the second one is a complicated theory. The simplest one follows the kinetic theory - the collision frequency increases linearly as the density and mean molecular velocity increase. The changes in density are given as T^{-1} and molecular velocity as $T^{1/2}$, thus the law obtains the temperature dependency with n = 0.5. In this study, the temperature dependence coefficient will be calculated and discussed in chapter 4.

The second one is a different but more complicated method to derive the temperature scaling law which takes the quadrupole-quadrupole forces produce the dominant interaction [44] into account, which was used by Birnbaum [42] for the pressure broadening in the microwave region. Later on, Bonamy *et al.* have found [43] out that the theory used by Birnbaum is based on the assumptions of straight-line trajectories. This means that the Birnbaum theory is more valid for the gas molecules which are at low temperature (distant collisions), but less valid for close collisions at higher temperatures. With such experimentally determined *n* values and less spectral resolution, the scaling law has been shown to be very steady for some degree of temperature ranges that matches the temperature of to the lower atmosphere [45, 46]. The value of *n* depends on the temperature range of the experiments and the increasing or deceasing value of rotational quantum *J*

number [44]. The temperature dependency for acetylene transitions has been studied before by Dhyene *et al*. [12] for C_2H_2, Predoi-Cross *et al.* for CO [47] and for CO_2 [48] and Chad Povey [49].

2.3 Schrödinger equation

Spectroscopic study of gas phase molecules such as this one involves analysis of absorption/emission spectra using the quantum mechanical knowledge of molecular structure. In this chapter we will discuss pure rotational and vibrational-rotational spectra of linear diatomic and polyatomic molecules. Spectra arise when absorptions or emissions occur, and they appear in the different region of the electromagnetic spectrum depending on the electric dipole moment change of the molecules. If any vibrational mode of a molecule gives a permanent dipole moment (i.e: $\mu=0$) at a frequency, then it means that the molecule is active in that frequency range. For example, C_2H_2 absorption spectra appears in the infrared region, which implies that for some of its normal modes this molecule is active in the infrared region because of the presence of the permanent dipole moment.

We have already discussed about the transition between two energy levels, E_n (upper state) and E_m (lower state), where absorption is the transition from lower state to upper state and emission is from upper state to lower state. In quantum mechanics, these energy states that are a set of eigenvlaues $\{E_i\}$ can be determined by solving the time-independent Schrödinger equation

$$\hat{H}\Psi = E\Psi \tag{2.7}$$

of nuclei and electrons. Here, $\hat{H}$ is the Hamiltonian of the molecule that represents the sum of kinetic and potential energy. The solution of this Schrödinger equation is a set of wavefunctios $\{\Psi_i\}$ and a set of eigenvlaues $\{E_i\}$ associated with these wavefunctions. In the procedure of solving this equation, one has to make prediction/approximation of the relation between stationary nuclei and fast-orbiting electrons. In the theory of molecular physics and quantum chemistry this approximation is known as Born-Oppenheimer approximation, named after Max Born and Robert Oppenheimer. In early 1900, Born related the particle form and wave form of a particle, and the probability of finding the particle in a space point and time. This Born-Oppenheimer approximation separates the wavefuntion in two parts (nuclei and electrons) by assuming that the motion of nuclei and electron can be separated (makes the solution much easier) [33].

2.4 Rotational Spectroscopy and Pure Rotational Transition

Considering the Schrödinger equation for rigid linear diatomic molecule [13],

$$\frac{\hat{J}^2\Psi}{2I} = E\Psi \tag{2.8}$$

Solutions of this equation give a set of wavefunctions $\{\Psi_i\}$ and corresponding eigenvalues $\{E_i\}$. Here $\hat{J}$ is the operator corresponding to the total angular momentum, $\hat{J} \neq 0$ = R+L+S+I = rotational + orbital +electronic spin + nuclear spin. In the case of pure rotational transitions where the molecule is rotating rather than vibrating, we include only the rotational angular momentum and exclude orbital, electronic and nuclear momentums. In the above equation I is the moment of inertia $I = \mu r^2$, where $\mu = m_1m_2/(m_1+m_2)$ is the reduced mass of the molecule and r is the internuclear distance between two atoms. The

rotational energy states (eigenenergy values – rotational energy levels) of a rigid diatomic molecule can be found by solving the above equation (2.5) as:

$$E(J) = \frac{h^2}{8\pi^2 I} J(J+1) \tag{2.9}$$

where J is the rotational quantum number; $J \geq 0$ and h is Planck's constant. It can be expressed in terms of wavenumber dividing by hc,

$$F(J) = \frac{E(J)}{hc} = \frac{h}{8\pi^2 cI} J(J+1) = BJ(J+1) \tag{2.10}$$

Here B is known as the rotational constant. The rotational constant value B can be found from the moment of inertia of the molecule; $B = h/8\pi^2 cI$ (in wavenumber form) is in inverse relation with moment of inertia I, as is internuclear distance r [33].

In the energy level system there is a whole series of rotational energy states appearing for each vibrational energy state. The transition between two rotational energy state in the same vibrational energy state is called the pure rotational transition and gives pure rotational spectra. The pure rotational transition follows the electric dipole moment selection rule, given as $\Delta J = \pm 1$ and $\mu \neq 0$ (i.e. must have permanent dipole moment). $\Delta J = \pm 1$ means transition between consecutive upper J' and lower J'' rotational energy state where $J' \leftarrow J''$ represents absorption and $J'' \leftarrow J'$ represents emission. Therefore, the absorption transition position or the rotational line position in wavenumber can be written as:

$$\tilde{\nu}_{J+1 \leftarrow J} = F(J+1) - F(J) \; = \; F(J') - F(J'')$$

$$= \; B(J+1)(J+2) \; - \; BJ(J+1) \; = \; 2B(J+1) \tag{2.11}$$

where B is a constant value so the spacing between the energy levels increases with the increasing rotational quantum number and becomes a multiple of $2B$ (twice the rotational constant), thus the spectra shows a pattern of equally distant rotational absorption lines.

The possibility of a transition taking place between two energy states depends on the population of those two states. Generally, we assume that at room temperature only the ground state is populated. The Boltzmann distribution function shows the relation between the ground N_0 and the upper N_J populated states as:

$$N_J = N_0(2J+1)\exp(-\frac{E_r}{kT}) \tag{2.12}$$

$$\frac{N_J}{N_0} = (2J+1)\exp(-BJ(J+1)/kT) \tag{2.13}$$

where k is the Boltzmann constant, $(2J + 1)$ represents the rotational partition function and T is the temperature of the gas sample. The higher the temperature, the higher J levels can be populated. In order to consider the symmetry of the molecules we include the term "rotational partition function" in the equation (2.13), which becomes:

$$N_J = N(2J+1)\frac{e^{-BJ(J+1)/kT}}{Q_{rot}} \tag{2.14}$$

where $$Q_{rot} = \sum_J (2J+1)\, e^{-BJ(J+1)/kT} \approx \frac{kT}{\sigma B} \tag{2.15}$$

represents the rotational partition function and σ is the symmetric number indicating 1 for asymmetric properties and 2 for symmetric properties. To determine the most populated rotational energy level we take the first order derivative with respect to J on both side of the equation (2.13) and equating to zero (0) gives:

$$\frac{d(N_J/N_0)}{dJ} = \frac{d}{dJ}[(2J+1)\exp(-BJ(J+1)/kT)] = 0 \quad (2.16)$$

$$J_{max} = (\frac{kT}{2B})^{1/2} - \frac{1}{2} \quad (2.17)$$

Now we should consider the non-rigid linear molecules because equations (2.10) and (2.11) are valid only for diatomic rigid rotors, and in reality, molecules are neither rigid nor their internuclear bonds [13, 33]. For real non-rigid molecules, the rotational energy increases as the rotational speed and the rotational quantum number *J* increase, which subsequently increases the interatomic distance due to an outward force, known as centrifugal force. All the atoms in real molecules experience a centrifugal force of increasing strength as the rotational quantum number increases. As a result, the spacing between the energy levels decreases (thus, the rotational constant *B*) with increasing distance between atoms *r* and equation (2.10) and (2.11) become, respectively:

$$F(J) = BJ(J+1) - D[J(J+1)]^2 \quad (2.18)$$

$$\tilde{\nu}_{J+1\leftarrow J} = F(J+1) - F(J) = F(J') - F(J'')$$

$$= 2B(J+1) - 4D(J+1)^3 \quad (2.19)$$

where $D = 4B^3/\omega^2$, is the centrifugal distortion constant and ω is the vibration wavenumber. This formula gets more and more complex for symmetric tops and asymmetric rotors, which will not be discussed in this thesis.

2.5 *Normal modes of the Polyatomic Linear Molecules*

A diatomic or polyatomic molecule shows different type of vibrational motions (for example: stretching, bending, rocking, wagging, etc). These motions depend on the degrees of freedom. A molecule of N atoms has 3N-5 or 3N-6 degrees of freedom. N atomic molecule has total 3N degrees of freedom of motion, from which it leaves 3N-5 or 3N-6 degrees of freedom after subtracting the translational and rotational degrees of freedom. Linear molecules have 3N-5 and non-linear molecules have 3N-6 degrees of freedom and they correspond to the number of independent normal modes of vibration [50].

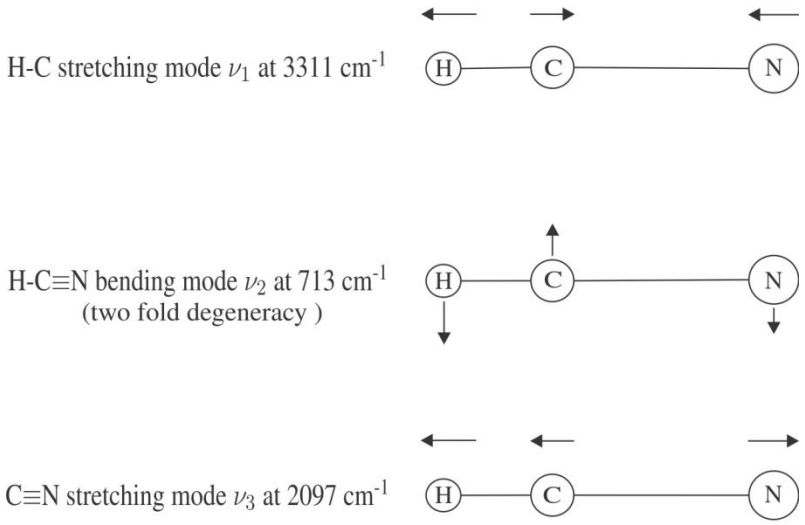

Figure 2.4: Fundamental modes of HCN.

N atomic linear molecules normally belongs to the $C_{\infty v}$ point group. Using the symmetry method (Group theory), the acetylene (H-C≡C-H) molecule is grouped under the $D_{\infty h}$ point group. The acetylene (H-C≡C-H) molecule has 3N-5 = 3*4-5 = 7 normal modes of vibrations: three of them are stretching modes and two of them are bending modes with double degeneracy, thus a total of seven fundamental vibrational modes. Seven vibrational modes of acetylene are labeled as $\mathbf{v_1 v_2 v_3 v^l_4 v^l_5}$. The symmetric C-H vibrational

stretching frequency $\nu_1(\sigma_g)$ at 3373 cm^{-1} is IR inactive, the asymmetric C-H vibrational stretching frequency $\nu_3(\sigma_u)$ at 3295 cm^{-1} is IR active, the C-C vibrational stretching frequency $\nu_2(\sigma_g)$ at 1974 cm^{-1} is IR inactive, the H-C≡C-H doubly degenerate trans-bending frequency $\nu_4(\pi_g)$ at 612 cm^{-1} is IR inactive and the C≡C-H doubly degenerate cis-bending (wagging) frequency $\nu_5(\pi_u)$ at 729 cm^{-1} is IR active. The subscripts g and u represents the symmetric and asymmetric property of the vibrational mode, respectively. Superscript *l* represents the vibrational angular momentum (which will be discussed later in this chapter) for which the positive and negative signs are associated with the clockwise and anticlockwise motion of the nuclei [13, 33].

Figure 2.4 is an example of the vibrational normal mode of hydrogen cyanide. Hydrogen cyanide (the H-C≡N) is a linear triatomic molecule belongs to the $C_{\infty v}$ point group and has 3N-5 = 3*3 – 5 = 4 normal modes of vibration. Vibrational modes of HCN is labeled as $v_1\ v_2^l\ v_3$. The H-C stretching mode v_1 appears at 3311 cm^{-1}, the C-N stretching mode v_3 appears 2097 cm^{-1} and the H-C-N bending mode v_2 appears at 712 cm^{-1} region of the electromagnetic spectrum. The v_2 bending mode is doubly degenerated [13, 33].

2.6 Vibrational Spectroscopy of Diatomic Molecules and Vibrational-Rotational Transition

The quantum mechanical approach to find the vibrational energy states is possible by solving the time-independent Schrödinger equation which relates the Hamiltonian, *H*, the wavefunctions, Ψ, and the corresponding energy eigenvalues as:

$$\hat{H}\Psi = E\Psi \tag{2.20}$$

The solution of the time independent Schrödinger equation is a set of eigenvalues (energy states). The energy states for a diatomic harmonic oscillator that obeys Hooke's law of spring is:

$$E(v) = h\nu(v + \frac{1}{2}) \tag{2.21}$$

in terms of wavenumber diving by *hc*,

$$G(v) = \frac{E(v)}{hc} = \tilde{\nu}_e \left(v + \frac{1}{2}\right) \tag{2.22}$$

where *h* is Planck's constant, ν is the vibrational frequency of the oscillator, $\tilde{\nu}_e$ vibrational frequency in wavenumber and $v \geq 0$ is the vibrational quantum number. Here $\nu = \frac{1}{2\pi}(\frac{k}{\mu})^{1/2}$, where k is the force constant and μ is the reduced mass. The distance between the vibrational energy levels are equally spaced for a harmonic oscillator. For a harmonic oscillator the emission or absorption processes take place at the same frequency but are different for an anharmonic oscillator. For an anharmonic oscillator the expression of vibrational energy state can be written as:

$$E(v) = h\nu_e \left(v + \frac{1}{2}\right) - h\nu_e x_e \left(v + \frac{1}{2}\right)^2 + \cdots \tag{2.23}$$

where the subscript *e* indicates the equilibrium position and the anharmonicity constant is represented by x_e, and ν_e is much more large than $\nu_e x_e$. Above expression can be written in the wavenumber form as:

$$G(v) = \frac{E(v)}{hc} = \tilde{\nu}_e \left(v + \frac{1}{2}\right) - \tilde{\nu}_e x_e \left(v + \frac{1}{2}\right)^2 + \cdots \tag{2.24}$$

Similarly, like the rotational transitions, the vibrational transitions also follow the selection rules. The electric dipole moment selection rule for the vibrational transition is $\Delta v = \pm 1$. The intensity of transition (absorption/emission) lines decrease as the vibrational quantum number v increases.

In the vibrational-rotational transition system the value of rotational constants depends on the nature of the vibrational state because the vibrational-rotational transition is a simultaneous system which incorporates both the vibrational and rotational motion of the molecules. Vibrational-rotational spectra are the result of these simultaneous motion of vibration and rotation of the molecules. Therefore, in the presence of both vibrational and rotational motion, the formulation of the vibrational-rotational energy levels must consider both rotational $F_v(J)$ and vibrational $G(v)$ terms. The transition term for the vibration-rotation spectra is shown below (in wavenumbers) [13, 33]

$$T = G(v) + F_v(J)$$

$$= \tilde{\nu_e}\left(v + \frac{1}{2}\right) - \tilde{\nu_e}x_e\left(v + \frac{1}{2}\right)^2 + B_v J(J+1) - D_v[J(J+1)]^2 \qquad (2.25)$$

Here, the rotational energy term $F_v(J) = B_v J(J+1) - D_v[J(J+1)]^2 + \cdots$ represents the vibrational dependency on rotation. The corrected rotational constant and the centrifugal distortion constants for the rotational motion that undergoes the vibrational motion are:

$$B_v = B_e - \alpha_e\left(v + \frac{1}{2}\right) + \gamma_e\left(v + \frac{1}{2}\right)^2 + \cdots \qquad (2.26)$$

$$D_v = D_e + \beta_e\left(v + \frac{1}{2}\right) + \cdots \qquad (2.27)$$

where the value of α_e and β_e are much smaller than B_e and D_e. In this case the vibrational transitions obey the selection rules $\Delta v = \pm 1$ together with the rotational selection rules $\Delta J = \pm 1$.

2.7 Degeneracy, Vibrational Angular Momentum and the l-type Doubling: e/f Parity

Degeneracy is a factor that may be found in some of the vibrational modes. For linear polyatomic molecule one can see the degeneracy for the normal bending modes. In the classical mechanical concept of the circular motion of nuclei for a linear polyatomic molecule, the circular path is formed around the horizontal axis of the molecule with a small amplitude. Double degeneracy refers to the clockwise and counterclockwise circular motion of the nuclei. Due to this circular motion, the nuclei experience an angular momentum which is called vibrational angular momentum. Vibrational angular momentum creates molecular energies which correspond to the rotational motion of the hydrogen atom around the axis of the molecule. The clockwise and anticlockwise rotational motion of the hydrogen can be explained by the superposition with a $\pi/2$ phase difference of two degenerate bending vibrations. For this motion of the nuclei, $\pm |l|\hbar$ units of angular momentum are possible and the possible positive values of the quantum number $|l|$ that are associated with the vibrational angular momentum are given below

$$l = v_i, v_i - 2, v_i - 4 \ldots, 0 \text{ or } 1 \tag{2.28}$$

where v_i represents the vibrational quantum number for the bending mode ν_i. Based on the

values of the quantum number $|l|$. the symmetry about the internuclear axis can be denoted by: Σ for $l = 0$, Π for $l = 1$, Δ for $l = 2$, etc. Different types of band will be discussed later in this chapter that are defined using the above mentioned Greek symbols.

There are four types of angular momentum that a molecule can have, but commonly most of the molecules show only vibrational and rotational angular momentum. Therefore, the total angular momentum would be the sum of the rotational R and vibrational l angular momentum: $J = R + l$. The double degeneracy in a molecule refers to having two rotational states of the same energy values. This degeneracy is removed due to the coupling of these two angular momentum R and l. When the degeneracy is removed, we see a split in these two identical doubly ($\pm|l|$) degenerated rotational energy levels with a difference of few wavenumbers which is called the l-type doubling effect having a magnitude of [13]

$$\Delta v = qJ(J+1) \tag{2.29}$$

where J is the rotational quantum number and q is the l-type doubling constant with $J = |l|$, $|l|+1$, $|l|+2$…etc.

This l-type doubling gives rise to doublets in the spectra. Therefore, the rotational energy term considering the both vibrational dependency and the l-type doubling is

$$F(J,l) = B_v[J(J+1) - l^2] - D_v[J(J+1) - l^2]^2 \tag{2.30}$$

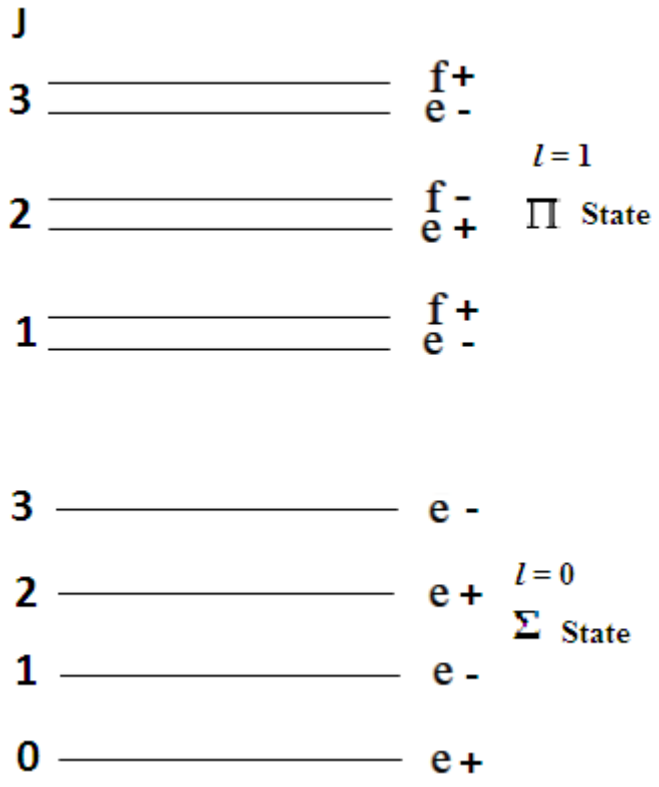

Figure 2.5: Parity labels for the rotational levels of a Π state (fundamental state $^1\Pi$) and Σ state (Example: for HCN molecule) [13].

To label the *l*-type doubling of the rotational energy levels, it is common to use the letters *e* and *f* known as *e/f* parity, shown in figure 2.5. For identifying parity that is associated with each transition, one needs to consider the inversion operation of the coordinate system of the molecule (electron and nuclei). The inversion operation of the wavefunction $\Psi = \Psi_{el}\Psi_{vib}\Psi_{rot}$ does not change the magnitude but only the sign. Thus, the parity *e* and *f* can have both positive and negative signs since the parity is a result of inversion property of the co-ordinate of electron and nuclei. The parity *e* is defined by $+(-1)^J$ and *f* is by $-(-1)^J$. For odd rotational quantum number *J*, the *e* and *f* parity will be negative and positive, respectively, and for even *J* values it is vice-versa. For vibrational

angular momentum l = 0, the rotational quantum numbers J has no f parity, it has only e parity (Σ – state) [13].

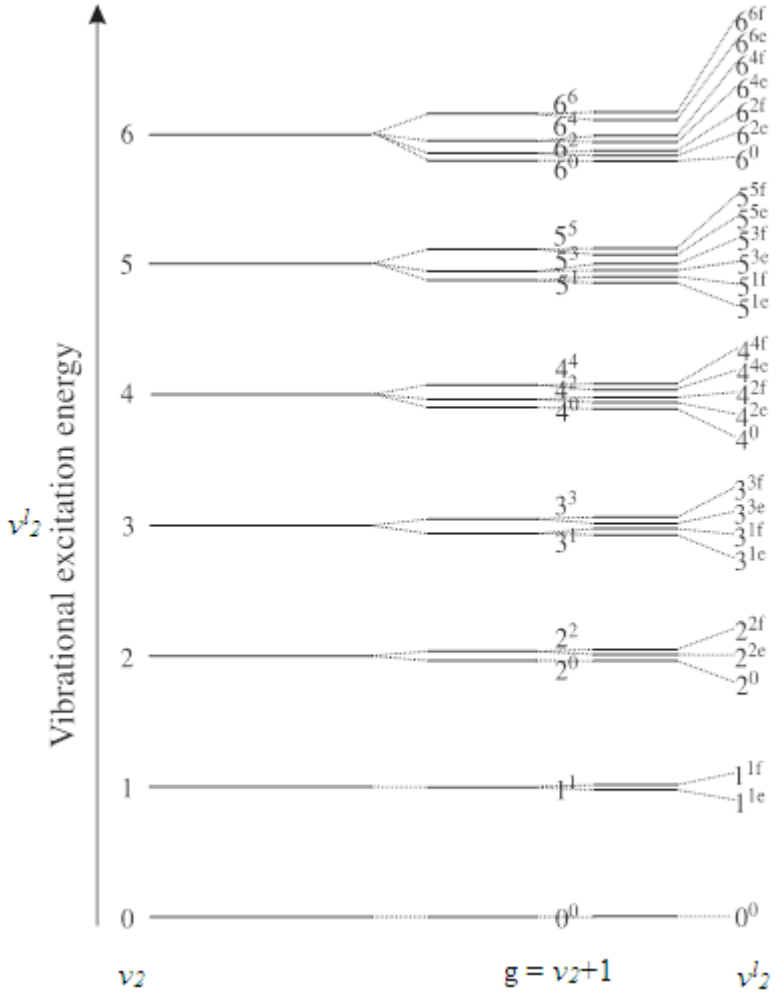

Figure 2.6: Bending energy structure of a triatomic linear molecule - two-dimension harmonic oscillator (Example: for HCN molecule) [13].

The degenerated bending energy levels of a two dimensional harmonic oscillator can be structured as in the figure below 2.6. The structure shows eigenenergies of the bending degenerate vibrational states v^l_2 of the two dimensional harmonic oscillator are split into g = v_2+1 sublevels. The levels of the two dimensional anharmonic oscillator are shown in the middle where the degeneration of the two-dimension harmonic oscillator is

removed. Each of the sublevels corresponds to different vibrational angular momentum with *e*/*f* parity state [28]. On the right of the structure in figure 2.6 shows the eigenenergy structure of the HCN bending vibration. The vibrational-rotational eigenstates of HCN can be labelled by *v*, *l*, *J*, (*e/f*) using the quantum numbers of the Wang symmetrized basis functions.

2.8 Vibrational Spectroscopy of Polyatomic Molecules and The Vibrational-Rotational Bands in Small Molecules

A vibrational band is a result of the transition between two vibrational states. In virbrational-rotaional bands, each vibrational level contains an entire set of rotational levels. The spacing between rotational levels is different for different vibrational states. The transitions from one rotational energy state to the other rotational state between two different vibrational energy state are called the vibrational-rotational transitions and then give vibrational-rotational spectra. We will consider a polyatomic molecule of N atoms in order to formulate the vibrational-rotational band. First, we can extend the expression of vibrational transition in the equation (2.24) for the harmonic N atomic molecule, as: [13]

$$G(v_1, v_2, \dots\ v_{3N-5}) = \tilde{\nu}_1\left(v_1 + \frac{1}{2}\right) + \tilde{\nu}_2\left(v_2 + \frac{1}{2}\right) + \cdots \tilde{\nu}_{3N-5}\left(v_{3N-5} + \frac{1}{2}\right) \tag{2.31}$$

Now we can consider the degeneracy factor in the vibrational term, then the equation (2.31) can be rewritten as:

$$G(v_1, v_2, \dots v_{3N-5}) = \sum_{1}^{3N-5} \tilde{\nu}_i(v_i + \frac{d_i}{2}) \tag{2.32}$$

where d_i is the the degeneracy of the i[th] mode of vibration for an N atomic molecule. The above terms are valid for the harmonic oscillator. In the case of the anharmonic ocsilator we need to introduce rotation together with vibration. Taking both rotation and vibration into account, the anharmonic terms in the potential of a polyatomic molecule causes the appearance of overtones as well as combination bands. Considering two or more of the vibrational quantum numbers, the vibrational energy term in the above equation will become:

$$G(v_1, v_2, \ldots v_{3N-5}) = \sum_1^{3N-5} \tilde{\nu}_i (v_i + \tfrac{d_i}{2}) + \sum_i \sum_{k \geq i} x_{ik} \left(v_i + \tfrac{d_i}{2}\right)\left(v_k + \tfrac{d_k}{2}\right) + \cdots \quad (2.33)$$

where x_{ik} are the anharmonicity constants. This equation indicates that for a combined state, one photon can excite two or more different vibrations simultaneously. Considering both the angular momentum and the degeneracy (denoted by the subscript *t*), this equation becomes:

$$G(v_1, v_2, \ldots v_{3N-5}) = \sum_1^{3N-5} \tilde{\nu}_i (v_i + \tfrac{d_i}{2}) + \sum_i \sum_{k \geq i} x_{ik} \left(v_i + \tfrac{d_i}{2}\right)\left(v_k + \tfrac{d_k}{2}\right) + \cdots + \sum_t g_{tt} l_t^2 \quad (2.34)$$

The transition wavenumbers for this complex vibrational-rotational transition is given in equation (2.25). Using equation (2.25) together with (2.34) we get the transition term for vibrational-rotational bands as:

$$T = G(v_1, v_2, \ldots) + F_v(J, l)$$

$$= \sum_{1}^{3N-5} \tilde{v}_i \left(v_i + \frac{d_i}{2}\right) + \sum_{i} \sum_{k \geq i} x_{ik} \left(v_i + \frac{d_i}{2}\right)\left(v_k + \frac{d_k}{2}\right) \qquad (2.35)$$

$$+ \sum_{t} g_{tt} l_t^2 + B_v J(J+1) - D_v [J(J+1)]^2$$

Different kinds of bands appear in the vibrational-rotational infrared spectra based on the transition types; such bands are fundamental bands, overtone bands, hot bands and combination bands. At room temperature the fundamental bands are most possible transitions which may be seen in the spectra more than the other type of bands. Fundamental band transitions take place between the ground state *v"* = 0 and the first vibrational excited state *v'* = 1. Onertone bands appears because of the transition between ground state *v"* = 0 and the second, third,…vibrational excited state *v'* = 2, 3, 4, …so on. These types of transitions are usually weaker than the others. Fundamental and overtone bands appear in the spectra of both diatomic and polyatomic anharmonic oscilator. For hot bands, the first requirement which is most important is high temperature and the transition type is *v"* ≠ 0 and *v'* = 2, 3, 4, …so on. Bands that are resulting from transitions between states obtained by mixing of the various normal modes of vibration are called the combination bands, normally appearing in the spectra of polyatomic anharmonic oscillator, for example $\nu_1 + \nu_3$, $\nu_2 - \nu_5$,…etc.

The vibrational transitions v_1, v_2, and v_3 of HCN molecule is structured down in figure 2.7. We know that the transitions from the ground state can be sorted in to three types of bands: fundamental, overtone and combination bands. Transitions such as ground state to the fundamental energy state: 0-1v_1, 0-1v_2 and 0-1v_3 are the fundamental bands of

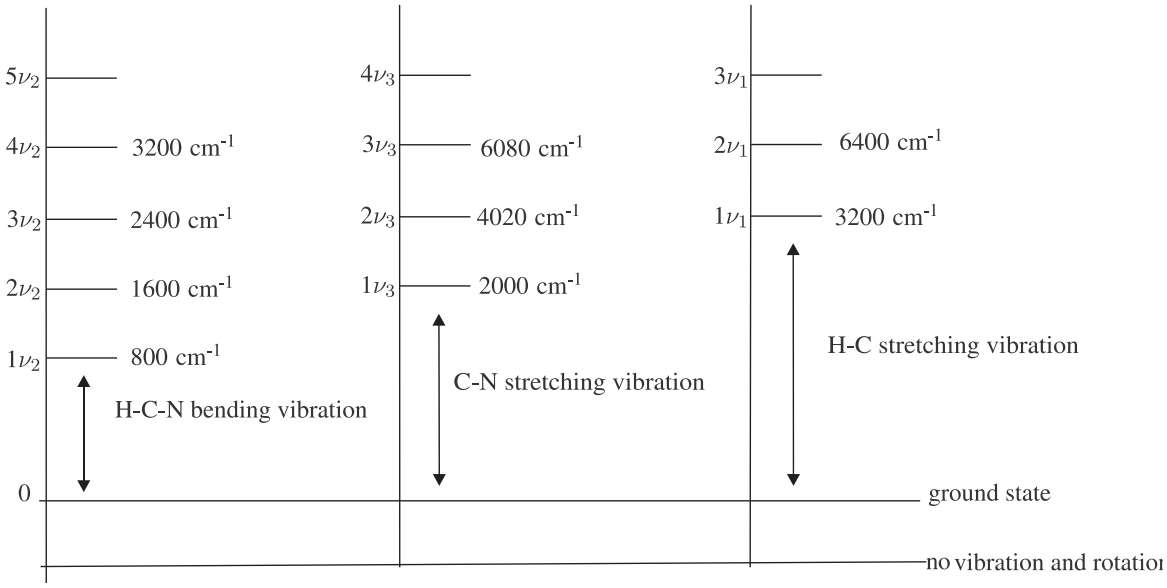

Figure 2.7: The pure fundamental and overtone vibrational transition of HCN.

HCN molecules. The 0-2ν_1, 0-3ν_1, 0-3ν_2, 0-3ν_3 and so on…are the overtone transitions; and ν_1+ν_3, 2ν_2+3ν_3, 4ν_1+5ν_3 etc. are the examples for combination bands formed by the combination of CN stretching, HC stretching and HCN bending vibrations.

2.9 The Parallel and Perpendicular bands (P-, Q- and R- branch system)

The above mentioned bands are the results of transitions from a rotational state of a vibrational state to another rotational state of another vibrational state. Depending upon the direction of change of the transition dipole moment, the vibrational-rotational bands of a linear polyatomic molecules can appear into two forms: parallel band and perpendicular band [33]. The classical configuration of parallel and perpendicular bands are shown in figure (2.8). The type of band that one will observe is depending on the direction of the dipole moment changes and the vibrational mode of the molecule. In the case of stretching vibration, a parallel band arises if the dipole moment changes in the parallel direction of

the molecular axis [50]. The change is the dipole moment component is the result of the combined stretching and rotating motion of the molecule. A parallel band consists of two

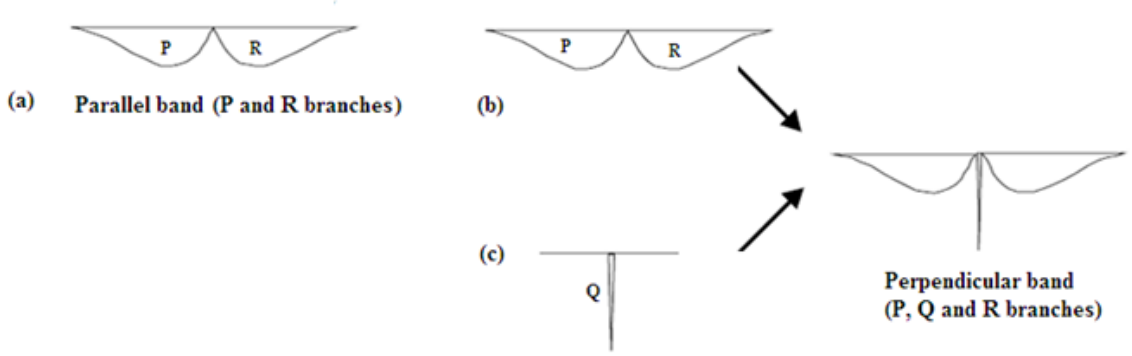

Figure 2.8: Classical picture of the origins of (a) parallel band and (b) & (c) perpendicular band.

branches called *P*- and *R*- branch as shown in figure (2.8 a). In the case of bending vibration, a perpendicular band arises if the dipole moment changes in the perpendicular direction to the axis of the molecule [50]. A perpendicular band consists of three branches called *P*-, *Q*- and *R*- branch shown in figure (2.8 b-c). In this case, the *P*- and *R*- branches arise when the rotational axis of the molecule is perpendicular to the bending plane (figure 2.8 b) and the *Q*- branch arises when the rotational axis of the molecule is parallel to the bending plane and the direction of dipole moment change of the molecule (figure 2.8 c).

As shown in the structure, *P*- branch start at left end (lower frequency), *Q*- branch is in the middle and *R*- branch end at the right end (higher frequency) of the electromagnetic spectrum. According to the quantum mechanical theory, the selection rules for *P*-, *Q*- and *R*- branches are defined as: $\Delta J = -1$ (*P*- branch), $\Delta J = 0$ (*Q*- branch) and $\Delta J = +1$ (*R*- branch), along with $\Delta l = 0, \pm 1$ gives the allowed transition.

1. $\Sigma \leftarrow \Sigma$ type parallel band arises with *P*- ($\Delta J = -1$) and *R*- ($\Delta J = +1$) branches if $\Delta l = 0$ where $l = 0$.

2. $\Pi \leftarrow \Sigma$, $\Delta \leftarrow \Pi$ type perpendicular band arises with *P*- ($\Delta J = -1$), *Q*- ($\Delta J = 0$) and *R*- ($\Delta J = +1$) branches if $\Delta l = \pm 1$. This is a perpendicular has a strong *Q*- branch.

3. $\Pi \leftarrow \Pi$, $\Delta \leftarrow \Delta$ type parallel band arises with weak *Q*- ($\Delta J = 0$) branch if $\Delta l = 0$ where $l \neq 0$. This type of bands never appears in the fundamentals band types and since $l \neq 0$. In this type of band transitions, the molecule is always in an excited bending vibrational mode [13].

2.9.1 The m Index

In the parallel band system, the P and R branches of a vibrational band can be represented with the upper and lower rotational quantum number *J''* and *J'* respectively, and replace by a single index *m* defined through:

$$m = (J' - J'')\frac{(J'+J''+1)}{2} \tag{2.36}$$

For the P-branch, *m* index values are the negative of the rotational quantum number *J''*; and $J' = J'' - 1$ gives $m < 0$. For the R-branch, *m* index values are the positive of the rotational quantum number *J'*; and $J' = J'' + 1$ gives $m > 0$.

Table 2.1: The *m* Index for The *P*- and *R*- branch.

Branch	*m* Index	
P branch:	$J'' = -m$	(2.37)
R branch:	$J'' = m - 1 \Rightarrow m = J'' + 1$	(2.38)

In the above expressions rotational quantum numbers *J''* and *J'* indicate the lower and upper energy levels of any transition, respectively. Starting from P and going up to R the numbers of "*m* index" variy from negative to positive values with the increasing transition frequency/wavenumber.

2.10 Line Intensity in an Emission Experiment

Derivation of the expression for the intensity analysis of the emission spectra will be discussed in details in this section. In a two level energy system, the Einstein coefficients for spontaneous emission and induced emission (discussed in section 2.1) are denoted by A_{nm} and B_{nm} respectively [33], and defined by

$$A_{nm} = \frac{64\pi^4}{3hg_n(4\pi\varepsilon_0)}\ \tilde{\nu}^3{}_{nm}|R^{nm}|^2 \tag{2.39}$$

$$B_{nm} = \frac{g_m}{g_n}B_{mn} = \frac{8\pi^3}{3h^2cg_n(4\pi\varepsilon_0)}\ \tilde{\nu}^3{}_{nm}|R^{nm}|^2 \tag{2.40}$$

the squared term $|R^{nm}|^2$ in both equations is known as the transition moment squared and $g_n$is the degeneracy. For a two level energy system of N_m lower and N_n upper, the rate of change of population is given in equation (2.41). Multiplying equation (2.41) by the energy of the transition $E = hc\tilde{\nu}_{nm}$ (energy difference between two levels), gives equation (2.42) and inserting A_{nm} from equation (2.39) into (2.42) gives equation (2.43):

$$(\frac{dN_n}{dt})_{SpE} = -N_nA_{nm} \tag{2.41}$$

$$I_{SpE} = N_nA_{nm}hc\tilde{\nu}_{nm} \tag{2.42}$$

$$I_{SpE} = N_n \frac{64\pi^4 c}{3g_n(4\pi\varepsilon_0)} \tilde{\nu}^4{}_{nm} |R^{nm}|^2 \tag{2.43}$$

The number of molecules present in the eigenstate $|n\rangle$ is given by the Boltzmann distribution, re-arranging equation (2.11) as:

$$\frac{N_n}{N} = \frac{g_n}{Q_{tot}} e^{(-\frac{E_n}{kT})} \tag{2.44}$$

where N_n is the number of molecules in upper eigenstate $|n\rangle$ and N is the total number of molecules present in the sample. Using the Boltzmann distribution from equation (2.44) in equation (2.43) produces intensity expression as:

$$I_{SpE} = \frac{64\pi^4 c}{3(4\pi\varepsilon_0)} \frac{N}{Q_{tot}} \tilde{\nu}^4{}_{nm} e^{(-\frac{E_n}{kT})} |R^{nm}|^2 \tag{2.45}$$

which is still not complete. We know that the intensity of emission line is proportional to number of photons detected by the detector. The energy of photons $E = (E_n - E_m) = h\nu = hc\tilde{\nu}$, can be derived from the energy difference between the lower and the upper eigenstates. Dividing equation (2.45) by the energy of a photon, gives

$$I_{SpE} = \frac{64\pi^4}{3h(4\pi\varepsilon_0)} \frac{N}{Q_{tot}} \tilde{\nu}^3{}_{nm} e^{(-\frac{E_n}{kT})} |R^{nm}|^2 \tag{2.46}$$

The number of molecules per unit volume, n = N/V can be determined by considering the ideal gas law: $PV = nRT$, which is related to the absorption or emission cell pressure P and temperature T:

$$\frac{N}{V} = n = \frac{p}{k_B T} = \frac{p}{k_B T_S} \frac{T_S}{T} \tag{2.47}$$

where N is the total munber of molecules in gas, V is the volume of the sample cell, k_B is the Boltzmann constant of value $1.38065 * 10^{-23}$ JK^{-1} and considering the standard temperature, T_s = 273.15 K, then equation (2.47), becomes:

$$\frac{1}{k_B T_s} = \frac{n(T_s)}{p_0} = \boldsymbol{\mathcal{L}} \tag{2.48}$$

Here $\boldsymbol{\mathcal{L}}$ is the Loschmidt number, the numerical value of this constant is $\big(L(Ts)\big) = 2.68676 * 10^{25}$molecules×m^{-3}atm^{-1}), the standard pressure p_0 is given in 1 atm unit and $n(T_s)$ is the number of molecules per unit volume at standard temperature. Therefore, for an ideal gas the Loschmidt number $\boldsymbol{\mathcal{L}}$, represents the number of molecules per unit volume at standard pressure and standard temperature. Let us consider C is the isotopic abundance of a given species. Now using C together with the equations (2.47) and (2.48), we obtain

$$n = pC\boldsymbol{\mathcal{L}}\frac{T_s}{T} \tag{2.49}$$

inserting n from equation (2.49) and using the the value of standard temperature in equation (2.46) leads to intensity expression for the molecular emission from the unit volume of the emission cell,

$$I_{SpE} = \frac{64\pi^4}{3h(4\pi\varepsilon_0)} \frac{pC\boldsymbol{\mathcal{L}}}{Q_{tot}} \frac{273.15K}{T} \tilde{\nu}^3{}_{nm} e^{(-\frac{E_n}{kT})} |R^{nm}|^2 \tag{2.50}$$

Here, Q_{tot} is the total partition function of the molecule, which is the sum of the product of the total degeneracy g_j and the eigenenergy E_j term of the energy state $|j\rangle$.

$$Q_{tot} = \sum_j g_j e^{(-\frac{E_j}{kT})} \tag{2.51}$$

also this partition function Q_{tot} is a product of the spin degeneracy and the vibrational and rotational partition functions, given as:

$$Q_{tot} = g_{ns} Q_{vib} Q_{rot} \tag{2.52}$$

The rotational partition function Q_{rot} is defined in equation (2.12). Euation (2.50) represents the emission intensity of a rovibrational transition. If all values in equation (2.50) are determined in SI units except pressure which is in atm then the units of intensity is derived in photons$\times s^{-1}m^{-3}$.

The transition moment squared or line strength $|R^{nm}|^2$in the equation (2.50), can be deduced using a perturbation calculation, the Born-Oppenheimer approximation and considering nuclear spin degeneracy g_{ns}, we get [51]:

$$|R^{nm}|^2 = g_{ns}\mu_v^2 * S_{v_n v_m} * S_{J_n J_m} * F_{v_n v_m} = g_{ns}\mu_v^2 * S_v * S_R * F \tag{2.53}$$

The transition dipole moment square, μ_v^2 is also known as vibrational transition dipole moment squared or dipole moment squared. It is used as a constant for a vibrational band of HCN and HNC in a first approximation. Here $S_{J_n J_m} = S_R$ is the Honl-London factor which includes the rotational dependancy of $|R^{nm}|^2$; $S_{v_n v_m} = S_R$ is the vibrationan intensity factor and $F_{v_n v_m} = F$ is the Herman-Wallis correction factor which inclued the vibrational dependency of $|R^{nm}|^2$. Inclusion of the vibrational transition dipole moment square and the Hermann-Wallis factor leads to a significant data reduction, so that only three parameters are needed for a complete band intensity.

The term $\mathcal{R}^{nm}$is used as the weighted transition moment squared, $\mathcal{R}^{nm} = \frac{|R^{nm}|^2}{g_m}$ [52-54] in the HITRAN database. At resonances the formulae derived above for intensity do not reproduce the band intensity because the intensity pattern is altered due to the resonance. In this cases, the line intensities have to be considered individual lines instead of bandwise. The relation between the weighted transition moment squared and the transition dipole moment squared is given by [53]:

$$\mathcal{R}^{nm} = \frac{|R^{nm}|^2}{g_m} = \frac{g_{ns}}{g_m}\mu_v^2 * S_v * S_R * F \tag{2.54}$$

Combining the previous expressions, we obtain:

$$S^p_{\tilde{\nu}_{nm}} = \frac{8\pi^3}{3hc(4\pi\varepsilon_0)}\frac{\mathcal{L}C\tilde{\nu}_{nm}}{Q_{tot}}\frac{273.15K}{T}e^{(-\frac{E_m}{kT})}[1 - e^{(-\frac{hc\tilde{\nu}_{nm}}{kT})}]g_{ns}\mu_v^2 * S_v * S_R * F \tag{2.55}$$

Using $Q_{tot} = Q_{vib}Q_{rot}g_{ns}$ for the line intensity in absorption

$$S^p_{\tilde{\nu}_{nm}} = \frac{8\pi^3}{3hc(4\pi\varepsilon_0)}\frac{\mathcal{L}C\tilde{\nu}_{nm}}{Q_{vib}Q_{rot}}\frac{273.15K}{T}e^{(-\frac{E_m}{kT})}[1 - e^{(-\frac{hc\tilde{\nu}_{nm}}{kT})}]\mu_v^2 * S_v * S_R * F \tag{2.56}$$

and

$$I_{SpE} = \frac{64\pi^4}{3h(4\pi\varepsilon_0)}\frac{pC\mathcal{L}}{Q_{tot}}\frac{273.15K}{T}\tilde{\nu}^3{}_{nm}e^{(-\frac{E_n}{kT})}g_{ns}\mu_v^2 * S_v * S_R * F \tag{2.57}$$

Using $Q_{tot} = Q_{vib}Q_{rot}g_{ns}$ for the intensity in an emission experiment, we have:

$$I_{SpE} = \frac{64\pi^4}{3h(4\pi\varepsilon_0)}\frac{pC\mathcal{L}}{Q_{vib}Q_{rot}}\frac{273.15K}{T}\tilde{\nu}^3{}_{nm}e^{(-\frac{E_n}{kT})}\mu_v^2 * S_v * S_R * F \tag{2.58}$$

The SI unit of I_{SpE} is $m^{-3}s^{-1}$, only the pressure unit is taken in atm. In CGS system the same intensity has an unit of $cm^{-3}s^{-1}$, which is obtained by multiplying the wavenumber

with a factor of 100 and omitting the $1/(4\pi\varepsilon_0)$ factor [55]. It is required to multiply the equation (2.58) by a factor of exactly 10^{-36} in order to use the transition moment squared in the unit of Debye^2. Here 1 Debye = 10^{-18} cm$^{5/2}$g$^{1/2}$s^{-1}.

2.10.1 Hermann-Wallis Factor

The theoretical formula of Herman-Wallis factor was first proposed by Herman and Wallis. The *P*- and *R*-branch Herman-Wallis factor of a diatomic molecules is given by the following formula [56]

$$F(m) = 1 + A_1(v)m + A_v(v)m^2 + \cdots \tag{2.59}$$

In equation (2.59) $A_1(v)$and $A_v(v)$are expressions that depend on the molecular cubic potential and quadratic dipole derivatives. Later on, [57] this expression was modified by Watson using the perturbation calculation, deduced to the following form:

$$F(m) = (1 + {A_1}^{RP}m + {A_2}^{RP}m^2)^2 \tag{2.60}$$

2.10.2 The Holn-London-Factor

Table 2.2: Holn-London-Factors for the linear triatomic molecule HCN

$\Delta l = 0$	$\Delta l = \pm 1$
P branch: $S_R = \frac{(m^2 - l^2)}{\lvert m\rvert}$	P branch: $S_R = \frac{\frac{1}{2}(\lvert m\rvert - l\Delta l - 1)(\lvert m\rvert - l\Delta l)}{\lvert m\rvert}$
R branch: $S_R = \frac{(m^2 - l^2)}{\lvert m\rvert}$	R branch: $S_R = \frac{\frac{1}{2}(\lvert m\rvert + l\Delta l + 1)(\lvert m\rvert + l\Delta l)}{\lvert m\rvert}$
Q branch: $S_R = \frac{(2J+1)l^2}{J(J+1)}$	Q branch: $S_R = \frac{\frac{1}{2}(J + l\Delta l + 1)(J - l\Delta l)(2J+1)}{J(J+1)}$

For the linear triatomic molecule HCN, the Holn-London factor S_R is derived for all three *P*-, *Q*- and *R*-branches with the condition of $\Delta l = 0$ and ± 1, $l = l''$ and $\Delta l = l' - l''$. The expressions are given in the Table 2.2 [55].

2.10.3 Vibrational Intensity Factor

The vibrational intensity factor is the product of the term value of transitions between the degenerate states and transitions between non-degenerate stats, denoted by S_v and defined by [58]

$$S_v = L_{13} * L_2 \tag{2.61}$$

in the case of HCN molecule, this term value is determined as 1.

2.11 Line Intensities in an Absorption Experiment

Basic theory of absorbtion mechanism for a monochromatic light radiation through a homogeneous gas layer is given by the Beer-Lambert law [13]. The law explains that the change in the intensity, $dI(\tilde{\nu})$, at a given wavenumber $\tilde{\nu}$ is proportional to the incremental depth *dl* of the gas layer and the intensity $I(\tilde{\nu})$of this radiance [53], i.e. :

$$dI(\tilde{\nu}) = -k(\tilde{\nu})I(\tilde{\nu})dl \tag{2.62}$$

Using $k(\tilde{\nu})$ as the absorption coefficient of the monochromatic radiation in per unit length (1/*m*). The monochromatic absorption coefficient $k(\tilde{\nu})$ is equal to the product of the value of integrated absorption coefficient *S* (in m^{-2}) of a rovibrational line and the normalized line shape function $f(\tilde{\nu} - \tilde{\nu}_0)$:

$$k(\tilde{\nu}) = Sf(\tilde{\nu} - \tilde{\nu}_0) \tag{2.63}$$

Here ($\tilde{\nu}_0$) is the transition frequency, at the center of an absorption line (position of the peak). Combining the normalized line shape function $\int_{-\infty}^{\infty} f(\tilde{\nu} - \tilde{\nu}_0) = 1$ with equation (2.63) we obtain the line intensity in terms of integrated absorption coefficient:

$$S = \int_{-\infty}^{\infty} k(\tilde{\nu}) d\tilde{\nu} \tag{2.64}$$

The calculated value of the integrated absorption coefficient is proportional to the gas pressure of to the number *n* of absorption molecules per unit volume, therefore

$$S = S_{\tilde{\nu}}^{p} p = S_{\tilde{\nu}}^{n} n \tag{2.65}$$

Here the unit of line intensity $S_{\tilde{\nu}}^{p} p$ is $atm^{-1}m^{-2}$ with pressure unit in atm, whereas considering the number *n* of absorption molecules per unit volume in molecules × m^{-3} gives the unit of line intensity $S_{\tilde{\nu}}^{n} n$ as m × $molecule^{-1}$. Thus, the relation between these two line intensities is:

$$S_{\tilde{\nu}}^{n}(T) = \frac{p}{n} S_{\tilde{\nu}}^{p}(T) \tag{2.66}$$

$$\frac{n}{p} = \frac{1}{k_B T} = \frac{1}{k_B T_s} \frac{T_s}{T} \tag{2.67}$$

The ratio (*n*/*p*) comes from the ideal gas law, where $k_B = 1.38065 * 10^{-23} JK^{-1}$ is the Boltzmann constant of the gas at temperature *T*. If T_s = 273.15 K is the standard temperature and $\boldsymbol{\mathcal{L}} = \big(L(Ts)\big) = 2.68676 * 10^{25}$ (molecules ×m^{-3}) is the Loschmidt number [58] at the standard pressure unit p_0= 1 atm, then the above relation becomes:

$$\frac{1}{k_B T_s} = \frac{L(T_s)}{p_0} \tag{2.68}$$

Combining the equations (2.67) and (2.68) we obtain:

$$S_{\tilde{\nu}}^{n}(T) = \frac{p_0}{L(T_s)} \frac{T}{T_s} S_{\tilde{\nu}}^{p}(T) \tag{2.69}$$

Using Loschmidt number $\boldsymbol{\mathcal{L}} = \frac{\boldsymbol{LT_s}}{\boldsymbol{p_0}}$, where the unit is in molecules $\times m^{-3}atm^{-1}$, then equation (2.69) becomes:

$$S_{\tilde{\nu}}^{n}(T) = \frac{1}{\mathcal{L}} \frac{T}{T_s} S_{\tilde{\nu}}^{p}(T) \tag{2.70}$$

For absorption and stimulated emission, the change in concentration *dn* is determind within an infinitesimal time *dt*, is given by adding the following two equations (2.71) and (2.72) and applying $dl = c \times dt$ (the absorbed radiation along the optical path length *dl*)

$$\left(\frac{dN_n}{dt}\right)_{Abs} = N_m B_{mn} \rho(\tilde{\nu}_{mn}) \tag{2.71}$$

and

$$\left(\frac{dN_n}{dt}\right)_{StE} = -N_n B_{mn} \rho(\tilde{\nu}_{mn}) \tag{2.72}$$

In the above two expression, N_m and N_n represent the populations of a two level eigenenergies E_m and $E_n$system, respectively, B_{mn} is the so-called Einstein coefficient constant for induced absorption and $\rho(\tilde{\nu}_{mn})$ is the energy density. The change in concentration, *dn* can be given as

$$d_n = \left(n_m B_{mn} I(\tilde{\nu}_{nm}) - n_n B_{nm} I(\tilde{\nu}_{nm})\right) dt = \left(n_m B_{mn} - n_n B_{nm} I(\tilde{\nu}_{nm})\right) \frac{dl}{c} \tag{2.73}$$

The change is the intensity $dI = (\tilde{\nu} - \tilde{\nu}_0)$ equals to $-dn * hc\tilde{\nu}_{nm}$ and thus

$$dI = -(n_m B_{mn} - n_n B_{nm} I(\tilde{\nu}_{nm}))dl \tag{2.74}$$

Combining equation (2.62) and (2.74) we obtain:

$$S = k(\tilde{\nu}_{nm}) = -\frac{1}{I(\tilde{\nu}_{nm})}\frac{dI}{dl} = (n_m B_{mn} - n_n B_{nm})h\tilde{\nu}_{nm} \tag{2.75}$$

Together with the following equation

$$B_{nm} = \frac{g_m}{g_n}B_{mn} = \frac{8\pi^3}{3h^2 c g_n (4\pi\varepsilon_0)}|R^{nm}|^2 \tag{2.76}$$

we obtain

$$S = (n_m \frac{8\pi^3}{3hcg_m(4\pi\varepsilon_0)}|R^{nm}|^2 - n_n \frac{8\pi^3}{3hcg_n(4\pi\varepsilon_0)}|R^{nm}|^2)\tilde{\nu}_{nm}$$

$$= [\frac{n_m}{g_m} - \frac{n_n}{g_n}]\ \frac{8\pi^3}{3hcg_n(4\pi\varepsilon_0)}\tilde{\nu}_{nm}|R^{nm}|^2 \tag{2.77}$$

Dividing (2.77) by the total number of absorbing molecules per unit volume *n* to obtain $S_{\tilde{\nu}}^n \frac{S}{n}$ as:

$$S_{\tilde{\nu}}^n = \frac{S}{n} = \frac{1}{n}[\frac{n_m}{g_m} - \frac{n_n}{g_n}]\ \frac{8\pi^3}{3hcg_n(4\pi\varepsilon_0)}\tilde{\nu}_{nm}|R^{nm}|^2 \tag{2.78}$$

Using the Boltzmann distribution $n_n = \frac{ng_n}{Q_{tot}}e^{(-\frac{E_n}{kT})}andn_m = \frac{ng_m}{Q_{tot}}e^{(-\frac{E_m}{kT})}$, we obtain:

$$S_{\tilde{\nu}}^n = \frac{8\pi^3}{3hc(4\pi\varepsilon_0)}\frac{1}{Q_{tot}}\tilde{\nu}_{nm}[e^{(-\frac{E_m}{kT})} - e^{(-\frac{E_n}{kT})}]\ |R^{nm}|^2$$

$$= \frac{8\pi^3}{3hc(4\pi\varepsilon_0)}\frac{1}{Q_{tot}}\tilde{\nu}_{nm}e^{(-\frac{E_m}{kT})}[1 - e^{(-\frac{hc\tilde{\nu}_{nm}}{kT})}]\ |R^{nm}|^2 \tag{2.79}$$

Taking the isotopic abundance into account

$$S_{\tilde{\nu}}^n = \frac{8\pi^3}{3hc(4\pi\varepsilon_0)}\frac{C}{Q_{tot}}\tilde{\nu}_{nm}e^{(-\frac{E_m}{kT})}[1 - e^{(-\frac{hc\tilde{\nu}_{nm}}{kT})}]|R^{nm}|^2 \tag{2.80}$$

According to the equation (2.80), the SI unit of the individual line strength $S_{\tilde{\nu}}^{n}$ is m×molecule^{-1} and in CGS is cm×molecule^{-1}. This expression is used in the HITRAN database [53] to calculate intensities.

Converting the unit of the intensity into SI unit m^{-2}×atm^{-1} by replacing with $S_{\tilde{\nu}}^{n}(T)$ in the expression for $S_{\tilde{\nu}}^{p}(T)$:

$$S_{\tilde{\nu}}^{p}(T) = S_{\tilde{\nu}}^{n}(T)\boldsymbol{\mathcal{L}}\frac{273.15K}{T}$$

$$= \frac{8\pi^3}{3hc(4\pi\varepsilon_0)}\frac{\boldsymbol{\mathcal{L}}C}{Q_{tot}}\frac{273.15K}{T}\tilde{\nu}_{nm}e^{(-\frac{E_m}{kT})}[1 - e^{(-\frac{hc\tilde{\nu}_{nm}}{kT})}]|R^{nm}|^2 \quad (2.81)$$

thus, all the physical quantities in equation (2.81) are converted into SI units, but only the pressure has a unit of atm, defined in the Loschmidt number of $\boldsymbol{\mathcal{L}}$ [59]. However, calculating in CGS units of cm^{-2}×atm^{-1}, needs a multiplication factor of 100 for the wavenumber and the factor $\frac{1}{4\pi\varepsilon_0}$ needs to be omitted [55]. To use the transition moment squared is in the unit of Debye^2, it is required to multiply the equation (2.86) by a factor of exactly 10^{-36} where 1 Debye = 10^{-18} cm$^{5/2}$g$^{1/2}$s^{-1}.

The well-known Beer-Lambert law [60] relates the intensity of a monochromatic radiation before $I_0(\tilde{\nu})$ and after $I(\tilde{\nu})$ traveling through a homogeneous gaseous sample of pathlength *l* is:

$$I(\tilde{\nu}) = I_0(\tilde{\nu})e^{-k(\tilde{\nu})l} \quad (2.82)$$

$$k(\tilde{\nu}) = -\frac{(\frac{I(\tilde{\nu})}{I_0(\tilde{\nu})})}{l} \quad (2.83)$$

Combing in equation (2.64), (2.82) and (2.83) to find the absorbance

$$S = \frac{1}{l}\int_{-\infty}^{\infty} \ln\left(\frac{I_0(\tilde{\nu})}{I(\tilde{\nu})}\right) d\tilde{\nu} = \frac{1}{l}\int_{-\infty}^{\infty} \mathrm{B}(\tilde{\nu}) d\tilde{\nu} \tag{2.84}$$

In the above expression, $\mathrm{B}(\tilde{\nu}) = \ln\left(\frac{I_0(\tilde{\nu})}{I(\tilde{\nu})}\right)$is the absorbance. Theoretically, the integrated absorption coefficient S can be obtained by integrating each line in the absorption spectrum within the limit of $-\infty$ to ∞ where the integration procedure and the absorption coefficient S corresponds to the determination of the area under the curve (the lineshape in the absorbance spectrum) [55].

For low pressure spectra a Gaussian type of line shape function and for high pressure a Lorentzian line shape is used. For Gaussian, the theory considers only a small region around the peak position which is three to five times of the line width, whereas for Lorentzian a wider area around the peak position is considered for integration because the tail of the Lorentzian peaks is very broad.

The calculation of absorption has a decadal logarithmic term($log\left(\frac{I_0(\tilde{\nu})}{I(\tilde{\nu})}\right)$) , so in order to convert the absorption coefficient into the natural logarithm [61] it is needed to be multiplied by a factor of ln(10) = 2.3036. The relation between S and $S^p_{\tilde{\nu}_{nm}}$ is:

$$S^p_{\tilde{\nu}_{nm}} = \frac{S}{p} = \frac{1}{pl}\int_{-\infty}^{\infty} \ln\left(\frac{I_0(\tilde{\nu})}{I(\tilde{\nu})}\right) d\tilde{\nu} = \frac{1}{pl}\int_{-\infty}^{\infty} \mathrm{B}(\tilde{\nu}) d\tilde{\nu} \tag{2.85}$$

which is the relation between the integrated absorption coefficients S given in m^{-2} [62] and the line intensity $S^p_{\tilde{\nu}_{nm}}$.

3 Experimental details

3.1 Description of the Laser Spectroscopy Facility

A laboratory-based spectroscopic study like this one needs a laser system, gas cells, detectors, vacuum pump system, heating and cooling system and a reliable software to control the entire setup. Our studies focus on wide spectral range. For the absorption experiment we have incorporated a tunable diode laser system including two gas cells of fixed pathlength, three optical detectors, pressure and temperature sensors. In the emission experiment we have a Fourier Transform Spectrometer with a heatable gas cell.

3.1.1 Temperature and Pressure Controlled Cells

There are different types of gas absorption cells available for laboratory experiments that include room temperature, room pressure, variable temperature and variable pressure gas cells. With the improvement of technology, a new type of gas absorption cell has been developed over the past twenty years which is commonly known as multi-pass gas absorption cell [63]. Multi-pass gas cells are designed with such multi-pass optical configurations so that one can obtain long absorption pathlength while recording experimental spectra. This long pathlength leads to an approach to improve any spectroscopic measurement.

The White design and the Herriot design are two types of multi-pass cell that can be used to achieve several meters of pathlength. An atmospheric study on ozone absorption cross-sections was performed using high-resolution Fourier Transform spectrometer coupled with a white type cell of 131.3 cm base length [64]. Helou *et al*. have used this

multi-pass cell to obtain variable temperature between 144K and room temperature, as well as a pathlength of 4*131.3 = 525.2 cm. An absorption gas cell, coolable from 120 K to room temperature with a temperature stability of ± 2 K and short path length between 0 and 3 cm was developed and reported by Lambot *et al.* [65]. This study was focussed on self-collisional broadening of acetylene absorption spectra recorded at 173 K and four different pressure ranging from 15 to 100 mbar using a tunable diode laser spectrometer (TDL).

Current available technology has improved the ability of the temperature controlled White type cells to obtain path lengths of 1 km. A gas cell with variable path length of minimum 0.3119 up to maximum 24.166 m, pressures between 0.210 and 49.9 Torr (1 Torr = 1.333 hPa) and temperatures from 294.45 to 295.75 K is presented in a study by Jacquemart *et al.* [66]. McKellar and co-authors have reported a temperature-controlled White type 5 m long multi-pass cell which can obtain a path length of 100 m after a total 20 times back and forth reflection [67, 68]. A multi-pass design was used to achieve 512 m path length that can endure a gas pressure of maximum 5 bar [69, 70]. Additionally, the study reported Ballard *et al*. [69] used corrosive and flammable gases at temperature between 190 and 300 K.

Two temperature controlled cells of base length 147.5 cm and 25 cm were accommodated in an experiment to record carbon monoxide spectra in the $3 \leftarrow 0$ band [47] region using a Bomem DA8.3 FTIR spectrometer. Both of the cells were designed for working conditions between 205 and 350 K but different pressure condition. Valentin *et al*. have constructed a stabilized low-temperature controlled cell for recording carbon monoxide absorption lines in the infrared region [71]. The temperature range from 80 to

250 K were controlled with liquid nitrogen and from a few K to 80 K with liquid helium, operated by an open cycle refrigerator. In another study, Sprakel *et al*. [72] have employed an experimental setup with an optical cell UV-visible and a liquid x-ray absorption spectroscopy cell that have temperature variability between 195 K and room temperature.

Using temperature variable cells needs the guaranty of achieving the set temperature and the stability. In order to examine the temperature variability and stability of the temperature-controlled cell, temperature sensors are usually mounted along the base length of the cells to monitor the temperature variability and the thermal gradients inside the inner chamber. Different studies have incorporated thermocouples in their experimental setup for testing temperature: [73] three thermocouples with an accuracy of ±1K have been used in a high temperature multi-pass gas cell; [74] six thermocouples with an accuracy of ±2K were directly measuring the temperature of the coolant; and [75] eight thermocouples have been employed to test the temperature stability of the entire cell body. A temperature gradient of ±0.31 K were reported in [47] by Predoi-Cross *et al.*. The smallest thermal gradient [76] was found for a temperature variable long path cell during an absorption study. A better temperature stability of 0.005 K was reported [63] for a copper-made, long path, Herriott optical designed cell. The cell was developed to obtain data in variable temperature between 20 and 296 K.

3.1.2 Our Laser Spectroscopy Facility

To probe remote sensing data, it is essential to perform laboratory experiments that can validate the database with better accuracy. High accuracy can be achieved by integrating heating/cooling and vacuum systems, compatible optical configurations, electronic designs and informatics. A tunable diode laser spectrometer system was used in

this research work to scan over the 1.5 to 1.63 microns spectral range. This instrument offers both the very high sensitivity and resolution needed in high accuracy line shape studies. Spectra were evenly re-sampled at the resolution of 0.0001 cm^{-1} when creating the transmission files. The pure acetylene gas used as reference was stated to be 99.96 % pure. The sample gas was a mixture of acetylene with a quoted concentration of 9.94% and nitrogen gas supplied by Praxair.

Simulations have been performed for transitions in the v_1+v_3 band of acetylene using line parameters available in the HITRAN08 database [77]. After completing the simulations, it was possible to determine both the pressure range for the projected measurements as well as what spectral lines could be correctly measured at levels well below saturation. The simulations procedure allowed us to select a total of 47 acetylene transitions in the v_1+v_3 band. Among them, 22 transitions in the P branch with corresponding rotational quantum number up to J = 31 and 25 transitions in the R branch with corresponding rotational quantum number up to J = 33 have been selected. For each spectral line we have recorded spectra at four different pressures of 100, 250, 400 and 500 torr. For each line and each pressure, we have recorded spectra at 7 different temperatures within -60° to 60° C in steps of 20° C.

The overall experimental setup contains three channels as shown in Figure 3.1. The tunable laser spectrometer system accommodates a temperature controlled cell, which was custom designed and built in our spectroscopy lab at the University of Lethbridge for spectroscopic studies of gases. This cell was filled with sample gas and implemented in the first channel of the spectrometer. A reference room-temperature cell filled with pure acetylene is implemented in the second channel. The third channel is used to record the

background signal needed to create transmission files. The temperature of the sample gas inside the first channel is controlled by liquid coolant, either ethanol or methanol, which is kept in a Neslab ULT-80 thermal bath.

The Neslab Chiller ULT-80 is an essential component to maintain the temperature control system of the sample gas inside the temperature controlled cell. Temperature of this cell can very between 193 and 353 K. The ULT-80 contains a powerful cascaded refrigeration system needed for fast cooling, obtaining extreme low temperatures and maintaining the stability of the chosen/set temperature. The Chiller controls the temperature of the fluid filled inside the reservoir of the refrigerator. The circulating pump of the Chiller can circulate the heating/cooling liquid externally through the cooling jacket of the inner cell with consistent flow.

During our measurements, both the sample and reference cell were initially evacuated by draining all the existing gas using a turbo pump to create a high vacuum and to eliminate chances for contamination to occur. Once the gas was introduced, we allowed time for the entire main cell to come to the same temperature. After vacuuming for several hours, the main cell was filled with the gas mixture of C_2H_2-N_2 and the reference cell with pure C_2H_2. The gas pressures were measured using highly accurate Baratron MKS gauges. The wavenumber was determined by using a WA-1500 EXFO Wavemeter.

The entire system is controlled and monitored using the LabVIEW software. LabVIEW offers a graphical user interface and is currently used by us to interface and control all instruments in our lab. A laser system of the New Focus Velocity model, which is combined with a Littman-Metcalf design, has been used to carry out this spectroscopic study. This laser system provides a wide spectral range over 1500-1570 nm by allowing a

(a)

(b)

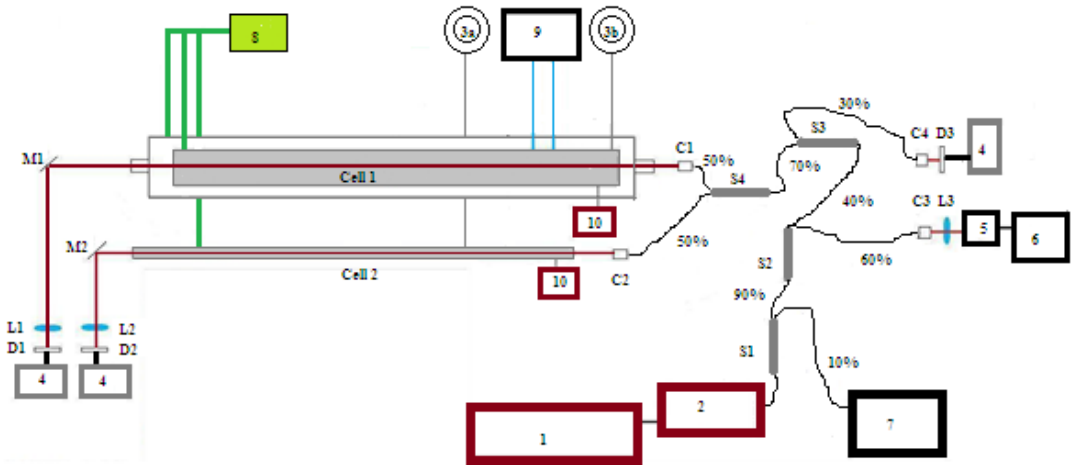

Figure 3.1: (a) photo , (b) schematic diagram of a 3-channel tunable diode laser spectrometer. Cell 1- temperature and pressure control cell. Cell 2- room temperature reference cell. 1&2. Velocity diode laser head and controller, 3. Sample gases (a. C_2H_2-N_2 & b. C_2H_2), 4. Detector pre-amps and power supplies for three InGas detectors D_1, D_2 and D_3, 5&6. Fabry Perot interferometer and controller 7. WA-1500 EXFO Wavemeter, 8. Vacuum system, 9. Cooling system (Neslab chiller) and 10. MKS Baratron pressure gauge. L_1, L_2 and L_3 refers to the lenses used to focus beam onto detector., M_1 and M_2 refers to the directing mirrors. C_1, C_2, C_3 and C_4 refers to the collimators used to couple the fiber Laser to free optics. S_1, S_2, S_3 and S_4 refers to the fiber splitters used to send signal to the various channels. The thick green lines represent the vacuum lines. The blue lines represent the coolant flow path. Thin curved lines represent the fiber optic cables. The red lines represent Laser path [18].

tunability of 30 GHz and very high signal-to-noise ratio, better than 2000 which is suitable for recording acetylene spectra. A laser central position was set at the starting frequency/wavelength before performing a scan. A Fabry Perot (FP) interferometer of 1.5 GHz (or 0.05 cm^{-1}) free spectral range has been introduced in this spectrometer setup in order to correct the non-linearity present in the piezo element. The piezo voltage covers between -3V and 2.7V (corresponds to a value little higher than 30 GHz) with a set interval close to 0.001V. The pressure and temperature was recorded at the starting and end of each piezo scan. The combination of FP and Wavemeter allows us to record accurate wavelength scales [18].

3.1.3 Mechanical and Optical Design of the Temperature-Controlled Cell

The schematic diagram of experimental setup used in the present study is presented in Figure 3.1. The first one of the three channels has two concentric chambers- referred to "cell 1" and the "outer chamber". The inner chamber is a temperature and pressure controlled gas cell of pathlength 1.54 m. Each end of the cell is fitted with a custom welded flange. The flanges are also made of stainless steel and have the same diameter as the inner pipe. Each flange has insert ports for temperature and pressure sensors, as well as ports for a gas inlet and a gas outlet. This is a single-pass gas cell which has anti-reflection CaF_2 windows on both ends, shown in Figure 3.2. These windows are mounted on the inner sides of the cell and are sealed by fluoro-silicon O-rings to make the inner chamber completely sealed.

There are five platinum resistor thermometers (PRT) mounted inside the gas cell with rods of different lengths as shown in Figure 3.3. These rods are attached to the cell flange by 1/8" diameters fittings. Having lengths of 6, 18 and 30 inches make it possible

to monitor the temperature at different points inside the gas cell. A combination of MKS Baratron pressure gauge (0 - 1000Torr) and a signal conditioner model 670 are used for measuring the gas pressures inside the gas cells. The stability of temperature and pressure has been monitored using the LABVIEW software.

The inner cell filled with sample gases is placed in the center of a vacuum jacket surrounded by the outer chamber that is maintained as vacuum. The inner cell is positioned in this way so that it does not touch the wall of outer cell. Through the evacuation process, the vacuum jacket reduces thermal conductivity by using a vacuum pump. The control in temperature (heating/cooling**)** is achieved using ethanol or methanol circulated in a Neslab ULT-80 thermal bath that is designed to adjust the required temperature range from 213 to 333 K inside the cell. The coolant fluid is allowed to flow through a pipe in direct contact with the entire length of the cell body so that the sample gas obtains the same temperature as the coolant has (shown in Figure 3.3).

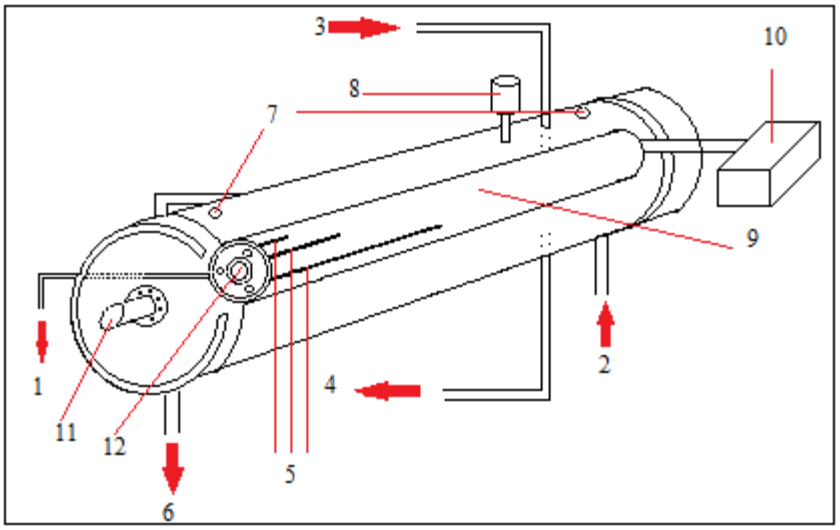

Figure 3.2: A 3-dimensional outline of the temperature controlled cell: 1. Gas inlet, 2. Gas outlet, 3. Coolant in, 4. Coolant out, 5. Three platinum resistor thermometers, 6. vacuum line , 7. vacuum feed through, 8. Pirani pressure gauge, 9. inner cell body, 10. MKS Baratron pressure gauge, 11. CaF_2 window at Brewster angle for the outer cell and 12. CaF_2 windows for the inner cell [18].

The outer chamber is made up of stainless steel pipe with a diameter of 6” and can be opened from both sides. This chamber is also provided with anti-reflection coated CaF2 windows, wedged at Brewster angles and placed in the center of both ends with the support of flanges. The vacuum prevents water condensation on the outer surface of the windows. The flanges on both ends of the outer chamber are not sealed like the inner chamber and can be removed to operate inner chamber insert/outlet valves. A compression ring, also made of stainless steel is mounted in-between each window and the corresponding flange. The sample cell is set on adjustable support stand, mainly needed for adjusting the alignment. This setup provides the required temperature and pressure of the sample gas [18].

3.1.4 The Reference and Background Channels of Our Laser Spectrometer

The second channel of the laser spectrometer contains a reference cell kept at room temperature. Both the temperature and pressure controlled cell and the reference cell have the path length of 1.54 m. Spectra recorded using this room temperature cell at 296 K are used as reference lines, which are needed to perform the line shift measurements. The shifts in the line positions can be measured by examining the reference position and comparing it to the position of the spectral line recorded with the temperature variable cell at elevated pressure. Pure acetylene gas was used to record the reference spectra in the room temperature cell. The gas pressures selected for the reference cell were in the 100 - 500 mTorr range. Both the sample cell and the reference cell are placed on support stands attached to the air table.

The third channel records the signal coming directly from the laser system used as the background spectra. The background signal is corrected with a Chebyshev polynomial

because it is needed to create the transmission files [18]. This method is also used to correct the baseline of signals from channels 1 and 2. The difference between channel 1 baseline and channel 3 background signal is calculated to find the best order of a Chebyshev polynomial. The background signal is then corrected with the determined order Chebyshev polynomial. After that the transmission spectra is created. Data were recorded simultaneously using all these three channels in order to complete an accurate line shape analysis of the spectral lines of interest.

3.1.5 Testing The Temperature Stability of the Variable Temperature Cell

The sensors for measuring temperature inside the temperature and pressure controlled cell are called platinum resistor thermometers (PRT), located inside the cell as shown in Figure 3.3. The PRTs were calibrated in the factory using a two-point method.

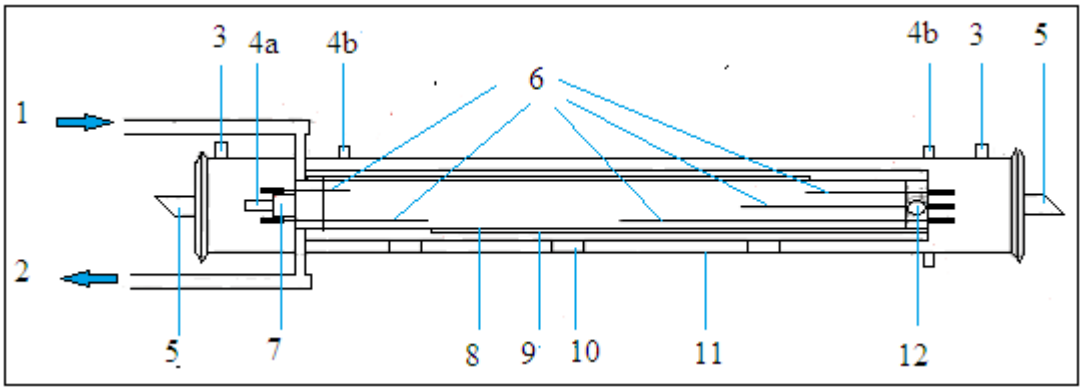

Figure 3.3: The temperature controlled cell (side view). Legend: 1. Coolant in 2. Coolant return. 3. vacuum port, 4a. gas inlet, 4b. vacuum feed-through for platinum resistors, 5. CaF_2 windows mounted at Brewster angle, 6. temperature sensors using platinum resistors, 7. vacuum valve, 8. fins for directing the coolant through the coolant jacket, 9. coolant jacket, 10. cell support, 11. outer cell body and 12. valve for de-pressuring of the outer jacket [49].

Additionally, they were calibrated in our experimental lab using a temperature monitoring unit model Lakeshore 330 as mentioned in [18]. The temperature calibration

curves (polynomial curves) for every sensor were fitted and were stored in the LabVIEW software, so that they were accessible to be applied each time while temperature measurements were made.

Testing of this temperature controlled cell was performed during a previous study [18]. The tests were carried out at different temperatures between 213 and 333 K for observing the stability in readings of each sensor over a time range, and for checking the temperature gradients along the cell. The performance of the temperature controlled cell is best at about 300 K in terms of temperature consistency over the five PRT (thermometers). In fact, the readings in all sensors shows a maximum difference of 0.3 K for all temperature tests above 273 K; however, it was a little higher for temperatures below 273 K (with a maximum of 0.4 K). These differences were calculated from the maximum difference between each two thermometers. The calculation of the standard deviation of recorded data in the five sensors was determined using 1000 data points. For most temperatures besides the extreme ones, it takes about 20 minutes to reach the set temperature and achieve stability. For extreme temperatures the cell needs at least 30 minutes to achieve thermal stability.

3.1.6 Controlling and Monitoring System of the Experimental Setup

A block diagram of the LabVIEW software is presented in Figure 3.3 [18] which is used for monitoring, data collection and controlling of the entire experimental setup. LabVIEW controls and monitors a New Focus Velocity laser system tunable between 1500 and 1570 nm and a Fabry Perot interferometer that enables the recording of spectra in accurate wavelength scales. Before scanning, the user can set a specific transitions wavenumber/wavelength or the entire wavelength range of interest to be scanned.

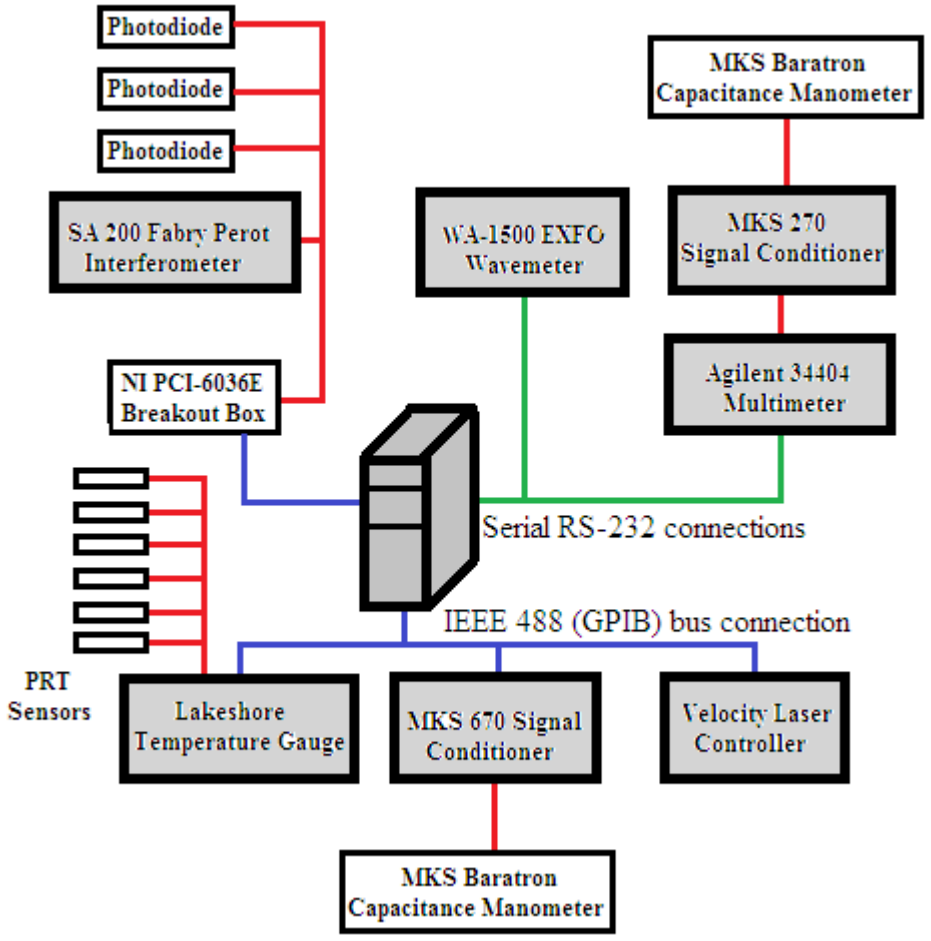

Figure 3.4: The block diagram of LabVIEW software used to record spectra with the laser spectrometer [18].

A series of programs was developed using the LabVIEW software which enables the recording and monitoring the temperature and pressure information [18]. Figure 3.4 shows connection between setup programs with the lines in different colors, where the red lines indicate analog signals that are digitized by a National Instruments 6036E Multifunction 16 channel 16-bit DIO card. The green lines represent serial RS-232 connections and the blue line represents the IEEE 488 (GPIB) bus connection. LabVIEW 8.0 is a Windows XP-based software. The shaded rectangular boxes represent test equipment that are operated by LabVIEW software. The Lakeshore model 218 temperature

gauge at the left-bottom of the diagram is used for monitoring the temperatures detected by six temperature sensors (platinum resistor thermometers) with an accuracy of +/- 135 mK at 300 K. Analog signals are produced by three photodiode sensors and read via 6036E card, and are connected by the red lines. A MKS Baratron Capacitance Manometer and a MKS 270 Signal Conditioner combined with an Agilent 34401A multimeter of accuracy 1 mV (or 6 digits of accuracy) can be used to digitize the pressure signal coming from channel 2. This pressure recording and monitoring system is interfaced to the LabVIEW software via a RS-232 serial link. Channel 1 pressure is digitized by a Baratron pressure gauge that is connected to a 670 signal conditioner and is interfaced using an IEEE 488 (GPIB) bus connection.

Before starting scanning of any absorption line, the center wavelength of the laser needs to be set to the desired starting point. The user can choose the Min (minimum) and Max (maximum) wavelength in order to scan over a wavelength range of interest. After each scan the laser center wavelength is shifted by 0.25 nm to start the next scan. The pressure and temperature of both cells are also measured simultaneously during each scan.

The line positions of the transitions are compared with those stored in the HITRAN 2008 data [77]. For this project, spectra were recorded at seven different pressures in the $\nu_1+\nu_3$ band. Spectral line data for the $\nu_1+\nu_3$ band is available [77] which was used to test accurate line positions and their intensities before recording spectra. The $\nu_1+\nu_3$ band is an ideal combination band to be analysed because of its intensity. Each spectrum was recorded at four different pressures between 100 and 500 Torr in channel 1, and at few hundred mTorr in channel 2. One of previous studies [18] performed using this same experimental setup proves that the line positions were on had an average difference of 0.002288 cm^{-1}

when compared to the HITRAN 2008 data base and of 0.002275 cm^{-1} compared to other reported data in [78] literature. The same previous study [18] also examined and found the difference between line positions recoded in channel 1 and 2 is 0.0000165 cm^{-1}. This difference agrees with the error value associate with the fitting routine reported in literature [79].

3.1.7 Data Processing and Crating Transmission Spectra

The transmission files can be processed after we correct the wavelength scale of the recorded signal/spectrum of all three channels using the information from the wavemeter and Fabry-Perot interferometer. Spectra recorded from the temperature and pressure controlled cell is called channel 1 spectra; from the reference cell is called channel 2 spectra; and the signal recorded from the laser is called background or channel 3 spectra.

The transmission files are created by following the procedure outlined below. First, we cut the spectral feature out of the raw file (spectra recorded on channel 1/channel 2) which gives the baseline of the spectra and then compare it with the spectrum of the third channel. Then the difference (residual) between the background spectra and the measured spectra can be calculated by subtracting *Channel 3* background from *channel 1* baseline. Next, we fit the difference/residual using the Chebyshev Polynomial (to find the best order) because it represents the best observed pattern of the background. After identifying the best order of Chebyshev polynomial, the background signal is then added to this Chebyshev polynomial to calculate the corrected baseline. Finally, the raw spectra recorded by channels 1 or 2 were divided by the corrected baseline in order to create the transmitted file. The spectra were fitted with selected line shapes models. The software [79] used to fit

with different line shapes was developed by Hurtmans *et al.*. The above mentioned steps can be formulated by the following expressions [18]:

$$resdiual = Channel1\ baseline - Channel3\ background \tag{3.1}$$

$$Cheb\ Poly + Channel3\ background = Corrected\ baseline \tag{3.2}$$

$$\frac{Cannel\ 1\ or\ 2\ raw\ spectra}{Corrected\ baseline} = Transmission\ Spectra \tag{3.3}$$

3.2 Experimental Setup for Emission Experiments

The emission measurements were performed using a Bruker IFS 120 High Resolution Fourier Transform Infrared spectrometer at the Justus-Liebig-University, Giessen, Germany. A custom made quartz cell was filled with the sample gas for recording

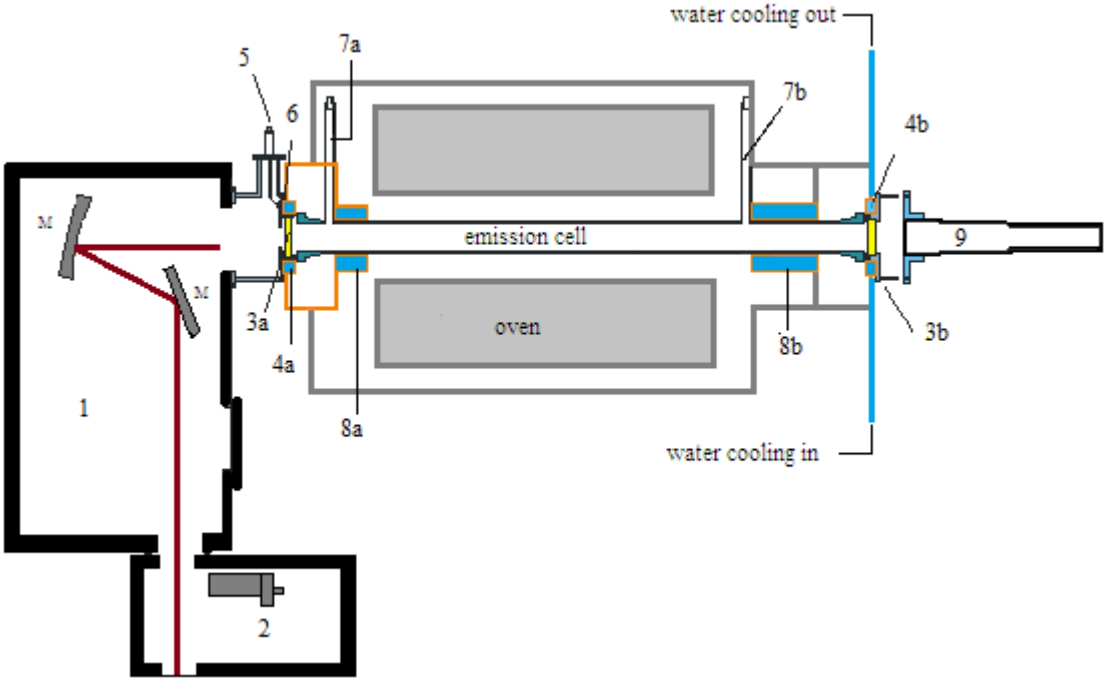

Figure 3.5: A schematic diagram of the laboratory experimental setup for emission experiment: 1. Transfer optics, 2. Bruker IFSI 120 HR source box, 3a & 3b.Cell window, 4a & 4b. Window cooling, 5. Aperture adjustment, 6. Emission cell iris, 7a & 7b. Sample in/out, 8. Cell cooling and 9. Laser alignment [80].

the data. The experimental setup is presented in Figure 3.5 and will be discussed below. No experiments were performed during this study. The spectra recorded before by Mellau [81], and also studied by Jan Schostag [55] have been used for the intensity analysis (discussed in Chapter 5). The spectra were recorded at 1450 ± 30 K at a pressure of 9 mbar in the ν_1 band of HCN. The spectra between the 3000 and 3500 cm^{-1} wavenumber range is presented in chapter 5. The experiment was performed at low pressure to avoid the effects of pressure-induced line shifts and Lorentzian line shapes [82].

The high resolution Fourier Transform infrared (FTIR) spectrometer system accommodates a heatable quartz cell and an adjustable iris that can regulate the radiative field of view. The transfer optics components are aligned to direct the input/output beam along the optical axis and mounted in an evacuated chamber to avoid any type of contamination like absorption by H_2O and CO_2. Any type of vibration can cause noise in the spectra while running an experiment. For that reason, a feather/spring insulator system was employed in order to protect the optics in the vacuum chamber [80]. The alignment was achieved by using a He-Ne laser source attached at the rear end of the cell tube. A mirror was chosen as the focusing optical aperture to ensure that the emission jets on the spectrometer screen have as small an aberration as possible and also to ensure minimum intensity losses. The 1 m long and 5 cm in diameter quartz cell was used as the emission cell. Both ends of this cell have CaF_2 windows fitted by O-rings. The quartz tube was heated using an electrical furnace (model RoK/A 6/60, Heraeus, Hanau). A water cooling system kept the CaF_2 windows at room temperature even though the middle section of the tube was set at 1450K inside the furnace. An InSb[6] detector was used to detect the emitted

[6] Indium antimonide

radiation that enters the FTIR spectrometer through an external input port [83]. This is an adjustable (tunable) iris used in order to adjust the field of view and intensity of the infrared beam inside the interferometer.

The furnace and the preconditioned cell were prepared before inserting the gas sample (HCN) by vacuuming the cell, heating of the furnace and the cell at 1450 K temperature. Then the cell was filled with the sample gas (HCN) after achieving the required temperature. Hydrogen Cyanide has a fairly quick decomposition characteristic, so the quartz cell was evacuated and refilled every 2 hours.

Two infrared spectra were recorded at low pressure of 9 mbars and then merged together [81]. For radiation detection an InSb quantum detector was used for recording both spectra. For each spectrum over 800 scans were averaged to improve the signal-to-noise ratio to a 2000:1 level.

To optimize the signal to noise ratio a correction needed to be carried out since the emission lines and the black body radiation emitted from the cell wall are superimposed on each other. This can be done by subtracting the background radiation from the emission spectrum recorded at the same temperature. Background spectra are measured with the empty cell and the emission spectrum comes from the sample gas. The signal-to-noise ratio is calculated from the total number of photons that falls on the detector which is the summation of the Planck background radiation and the molecular radiation. It is possible to increase the signal to noise ratio of 3000:1 to 10000:1 for highly intense emission spectra by using filters of different bandpass [55].

4 Analysis

4.1 Spectroscopic Line Shape Study of Acetylene Broadened by Nitrogen

This chapter covers the analysis of acetylene spectra broadened by nitrogen. This experimental study, data and results were published in Molecular Physics Journal [84]: Hoimonti Rozario, Jolene Garber, Chad Povey, Daniel Hurtmans, Jeanna Buldyreva and Adriana Predoi-Cross, "*Experimental and theoretical study of N_2-broadened acetylene line parameters in the $\nu_1+\nu_3$ band over a range of temperatures*, Molecular Physics: 110, Special Issue: SI 21/22 (2012) 2645-2663. The theoretical calculations were performed by Jeanna Buldyreva who is a co-author of the paper. I have included the theoretical results in my thesis for the consistency and comparisons between theory and experimental results.

Acetylene spectra were recorded in our laser spectroscopy lab at the University of Lethbridge, using a Tunable Diode laser spectrometer [84]. The spectral lines were modeled using a multispectrum fit software [79]. Multispectrum fit is a least square iterative fitting procedure which convolves the instrumental line shape [38] with the choice of different line shape (Voigt [13], Rautian, Galatry) models. Marquardt algorithm is a built in algorithm in program to adjusts the individual line parameters by minimizing the difference between the experimental and theoretically modeled spectra.

The absorption line positions in each recorded spectrum were initially calibrated by using the data listed within the HITRAN 2008 database [77]. For the initial guess of fit parameters, we have used the values reported in a previous [77] study. For modeling our experimental spectra, two lineshape profiles have been chosen to accomplish the

spectroscopic analysis are: Voigt and Rautian (Hard Collision) profiles. The narrowing parameter was set at the value quoted in [25].

The N_2-broadening ($\gamma^0_{N_2}$) coefficients (unit in $cm^{-1}atm^{-1}$), pressure-shift ($\delta^0_{N_2}$, δ'_{N_2}, δ'_{1N_2}, δ'_{2N_2}) coefficients (unit in $cm^{-1}atm^{-1}$) and their temperature dependence coefficients were determined using the following formulas:

$$\gamma(p,T) = p \times \left[\gamma^0_{N_2}(p_0,T_0) \times (1-\chi) \times \left[\frac{T_0}{T}\right]^n + \gamma^0_{self}(p_0,T_0) \times \chi \times \left[\frac{T_0}{T}\right]^n \right], \quad (4.1)$$

$$\nu(T) = \nu_0 + p \times [\delta^0_{N_2}(T) \times (1-\chi) + \delta^0_{self}(T) \times \chi], \quad (4.2)$$

$$\delta^0_{N_2}(T) = \delta^0_{N_2}(T_0) + \delta'_{N_2} \times (T - T_0), \quad (4.3)$$

$$\delta^0_{N_2}(T) = \delta^0_{N_2}(T_0) + \delta''_{1N_2} \times (T - T_0) + \delta'_{2N_2} \times (T - T_0)^2 / 2. \quad (4.4)$$

The term $\gamma(p,T)$ in equation (4.1) represents the half-width (in cm^{-1}) of the absorption line at total sample pressure of $p = p_{N_2} + p_{self}$ and temperature T. The pressure and the temperature T are given in atm and Kelvin, respectively, χ represents the mixing ratio of the sample (ratio of the partial pressure P_{self} to the total sample pressure) and n is the temperature dependence exponent of the sample gas. Here, $\gamma^0(N_2)(p_0, T_0)$ is the half width of the absorption line at the reference pressure p_0. The reference pressure p_0 corresponds to 1 atm, and the reference temperature T_0 is set at 296 K.

The measured absorption line position ν at the total pressure p where ν_0 is the position at zero pressure can be determined by the equation (4.2). The temperature dependence of shift coefficients was modeled and determined by either of the two equations (4.3) and (4.4). The initial guesses for self-broadening and self-shift coefficients

are taken from a previous study [25]. A summary of previous spectroscopic line shape studies in acetylene is given in Table 4.1.

Table 4.1: Summary of previous studies of acetylene broadened by N_2 [84]

Vib. Band	Temp.	Broadener	Assignment range	Line shape model	Ref.
ν_5	297K	N_2, O_2	P(29)-R(25)	Voigt	[2]
ν_5	297K	N_2, O_2	P(35)-R(34)	Theoretical(RB)	[19]
ν_5	147-295K	H_2, N_2, He, Ar	P(8)-R(21)	Voigt	[7]
ν_5	296K	H_2, N_2, He, Ar	R(3)-R(34)	Theoretical(RB)	[20]
ν_5	173.4K	N_2	P(29)-R(28)	Rautian,theoretical (RB)	[5]
$\nu_4+\nu_5-\nu_4$	296K	N_2, He	Q(1)-Q(35)	Theoretical(ECS)	[21]
$2\nu_5-\nu_5$	296K	N_2, He	Q(1)-Q(35)	Theoretical(ECS)	[21]
$\nu_4+\nu_5-\nu_4$	183.2,198.2K	N_2, He	Q(1)-Q(35)	Theoretical(ECS)	[11]
$2\nu_5-\nu_5$	183.2,198.2K	N_2, He	Q(1)-Q(35)	Theoretical(ECS)	[11]
$\nu_4+\nu_5$	296K	N_2, air	P(31)-R(20)	Voigt	[22]
$\nu_4+\nu_5$	173.2-273.2K	N_2	P(1)-R(23)	Voigt,Rautian	[12]
$\nu_4+\nu_5$	298K	N_2	P(17)-R(22)	Voigt,Rautian	[85]
$\nu_4+\nu_5$	173.2-298.2K	N_2	R(11)-P(23)	Voigt,Rautian,Galatry	[23]
$\nu_1+\nu_3$	295K	H_2, N_2, D_2, air	P(31)-R(27)	Voigt	[24]
$\nu_1+\nu_3$	296K	C_2H_2, N_2	P(11)	Voigt,Rautian,Galatry	[25]
$\nu_1+\nu_3$	195,373,473 K	N_2	P(25)-R(25)	Voigt	[10]
$\nu_1+\nu_5$	296K	C_2H_2,N_2,Ar	R(0)-R(7), Q(7)-Q(29)	Rautian	[16]
$\nu_1+3\nu_3$	298K	N_2, O_2, He, Ar, Ne, Kr, Xe	P(17)-R(22)	Galatry,Rautian	[26]
$\nu_1+\nu_2+\nu_4+\nu_5$	213-350K	C_2H_2	R(0)-R(19)	Voigt,SpeedDependent Voigt	[18]

In a previous study performed in the same manner as this one reported that a weak line mixing effect occurs in individual transitions due to collisional transfer between two energy levels *j* and *k* [18]. At high pressure, absorption lines that are very closely spaced, as a result they become over broaden and overlap each other. In that case, those lines are no longer be considered as isolated lines. To account for this line- mixing effect, the weak line mixing coefficients Y_{0i} have been calculated using the Exponential Power Gap method. A linear equation $Y_i = pY_{0i}$ express the relation between the total calculated line mixing component, Y_i, and the total pressure *p* of the sample gas. Voigt or Speed-dependent Voigt profile was incorporated in the software to model this effect by the equation (13) reported in [18]. The β parameter is used for expressing the off-diagonal matrix elements, W_{jk} as a function of the collisional transfer rate, with the of value β = 0.56, where $W_{jk} = -\beta_{kjk}$. This collisional transfer rate is calculated using the Exponential Power gap (EPG) law for a pairs of rotational levels, from lower *k* to a higher *j* level by the equation (13) given in Ref. [18]. In that equation, B_0 is the rotational constant for the corresponding energy level, ΔE_{jk} is the energy difference between a pair of energy levels. In this equation, the parameters *a*, *b*, and *c* were optimized to improve the calculated broadening coefficients so that they are matched with the experimental ones. For values retrieved for P-branch transitions were *a* = 0.06184, *b* = 0.31698, *c* = 1.28210, and for R-branch transitions were *a* = 0.06883, *b* = 0.37615, *c* = 1.17421. For each column of the relaxation matrix, the sum of off-diagonal elements of the relaxation matrix matches the measured pressure broadening coefficients through the sum rule within 1.54×10^{-23} for P-branch transitions and 1.70×10^{-22} for R-branch transitions. Parameters a, b and c were calculated for seven different temperature using the Voigt and the Speed Dependent Voigt models. The value of the temperature dependency

of weak ling mixing were found to be very small. The calculated asymmetry that were found due to line mixing effects has been taken into account in our non-linear fitting procedure assuming that the temperature dependence of the weak line mixing coefficients is negligible. The retrieved broadening coefficients are not affected by the inclusion of line mixing effects. However, the pattern of the shifts as a function of m is smoother when line mixing effect is accounted for.

We have performed semi-classical theoretical calculation to compute N_2-broadening, shifts parameters and their temperature dependence coefficients for the R-branch. We have compared our results with other results collected from different experimental studies published previously on acetylene broaden by nitrogen, as well as with the theoretical results obtained during this present study.

4.2 Semi-Classical Formalism for Line Broadening and Shift Calculations

Table 4.2: Atom-atom interaction parameters for the C_2H_2-N_2 system [84]

r_{1i}, r_{2j} (Å) [8]		d_{ij} 10^{-7} erg Å^{12}	e_{ij} 10^{-10} erg Å^6	Reference	V_{iso} model
r_{1C} = 0.6035	CN	0.3234	0.2922	[86]	"V_{iso} LJ"
	HN	0.0571	0.0803		"numerical V_{iso}"
					"V_{iso} LJ trial"
r_{1H} = 1.6614	CN	0.0018	0.0146	calculated from [87] ("final" values)	"numerical V_{iso}-2"
	HN	0.0002	0.0004		
r_{2N} = 0.550	CN	0.4773	0.2983	calculated from [87] ("initial" CN values)	"numerical V_{iso}-3"
	HN	0.0571	0.0803		

A details of the semi-classical calculations of line widths γ and line shifts δ will be discussed in this section. Semi-classical theoretical calculations like this one, have been

performed using the standard expression of the perturbative approach of Robert and Bonamy [88] but supplied by exact trajectories determined by the isotropic part of the intermolecular interaction potential [89]. Considering the vibrational transition $i \rightarrow f$ these line widths γ and line shifts δ in the unit of wavenumber (cm^{-1}) can be written as

$$\gamma_{fi} - i\delta_{fi} = \frac{n\bar{v}}{2\pi c}\int_0^{\infty} 2\pi b db \left\langle 1 - e^{-\mathrm{Re}\,S_2} e^{-i(\mathrm{Im}\,S_2 + S_1)} \right\rangle_{J_2}, \tag{4.5}$$

where n is known to be the number density of perturbing particles, $\bar{v}$ is the average of thermal velocity, c is the speed of light, b is the impact parameter further replaced by the distance of the closest approach r_c. Here, S_1 is the first-order and S_2 is second-order contributions to the scattering matrix, and the $\langle ... \rangle_{J_2}$ term indicates the average over the rotational states of the perturber. Approximation of the mean thermal velocity for C_2H_2-N_2 gas mixture has been found to be accurate at temperatures higher than 143 K while considering the system in the frame of quantum-mechanical close coupling calculations [90]. Therefore, for the molecular system considered in the present work it is expected to be valid too because the selected temperature conditions are above 200 K.

The explicit form of Re S_2 term for two linear molecules following exact trajectories can be calculated from the general formulae of two asymmetric colliders 1 and 2 [91]. This can also be deduced directly from the rotationally invariant representation of the intermolecular interaction potential as given below:

$$V(1,2,\vec{r}) = \sum_{l_1 l_2 l} V_{l_1 l_2 l}(r) \sum_{m_1 m_2 m} C^{lm}_{l_1 m_1 l_2 m_2} Y_{l_1 m_1}(\theta_1, \varphi_1) Y_{l_2 m_2}(\theta_2, \varphi_2) C^{*}_{lm}(\theta, \varphi) \tag{4.6}$$

the corresponding imaginary part $\mathrm{Im}S_2$ is further obtained with equation (10) of Ref. [88]. In the above equation (4.6), the first term inside the first summation $V_{l_1 l_2 l}(r)$ are the radial

potential components including contributions from various kinds of intermolecular interactions and the first term inside the second summation $C^{lm}_{l_1 m_1 l_2 m_2}$, are the Clebsch-Gordan coefficients. The multiplication of spherical harmonic terms $Y_{l_1 m_1}(\theta_1, \varphi_1) \times Y_{l_2 m_2}(\theta_2, \varphi_2) C^{*}_{lm}(\theta, \varphi)$ (products of the spherical harmonics) represents the rotationally invariant basis in the laboratory-fixed frame where the component $C^*_{lm}(\Theta, \varphi)$ with asterisk denotes the complex conjugation. In order to compose the intermolecular interaction potential, we have chosen $l_1 \leq 2$ and $l_2 \leq 2$ where the potential is considered as a sum of electrostatic (*e*) quadrupole-quadrupole and pairwise atom-atom (*a*) interactions. The quadrupole moment values of the electrostatic term $V^{e}_{224}(r) = 4\pi\sqrt{70}\, Q_1 Q_2 / (5r^5)$ are taken as $Q_{C2H2} = 4.0 \cdot 10^{-26}$ esu cm^2 [5] and $Q_{N2} = -1.52 \cdot 10^{-26}$ esu cm^2 [92] (for final calculations) to used in this theoretical method. Here the radial potential components are defined by the functions of the interatomic parameters d_{ij} and e_{ij} which is defined via the Lennard-Jones parameters ε_{ij}, σ_{ij} of the atoms *i* and *j* as $d_{ij} = 4\varepsilon_{ij}\sigma_{ij}^{12}$, $e_{ij} = 4\varepsilon_{ij}\sigma_{ij}^{6}$:

$$V^{a}_{l_1 l_2 l}(r) = \sum_{i,j} [d_{ij} f^{12}_{l_1 l_2 l}(r_{1i}, r_{2j}, r) - e_{ij} f^{6}_{l_1 l_2 l}(r_{1i}, r_{2j}, r)] \xi_{1i} \xi_{2j} \qquad (4.7)$$

where, in the molecular frame of atom *i* we have considered $\xi_{1i} = 1$ and $\xi_{1i} = (-1)^{l_1}$ for a positive *z*-value and a negative *z*-value, respectively (taking the origin of this coordinate system at the center of mass of the molecule and the molecular *z*-axis as the axis of the molecular symmetry). Similar condititions are applied in the molecular frame of the *j*-atoms of the perturbing molecule where $\xi_{2j} = 1$ and $\xi_{2j} = (-1)^{l_2}$ for a positive *z*-axis value and a negative *z*-axis value, respectively. The functions $f^{n}_{l_1 l_2 l}(r_{1i}, r_{2j}, r)$ come from the two-

center expansion [93] of the interatomic distances $r_{1i,2j}^{-n}$ and for the chosen representation of the intermolecular potential have the form as given below:

$$f_{l_1 l_2 l}^{n}(r_{1i}, r_{2j}, r) = \frac{(-1)^{l_2}}{r^n} 4\pi \sqrt{(2l_1+1)(2l_2+1)}\, C^{l0}_{l_1 0 l_2 0} \sum_{p,q} \left(\frac{r_{1i}}{r}\right)^p \left(\frac{r_{2j}}{r}\right)^q$$
$$\times \frac{(n+p+q-l-3)!!(n+p+q+l-2)!!}{(n-2)!(p-l_1)!!(p+l_1+1)!!(p-l_1)!!(p+l_1+1)!!} \times \left\{1+\delta_{n1}(\delta_{pl_1}\delta_{ql_2}\delta_{p+q,l_1}-1)\right\} \tag{4.8}$$

with $p = l_1, l_1+2, l_1+4, \ldots$; $q = l_2, l_2+2, l_2+4, \ldots$. The sets of atom-atom parameters tested in the present work are assembled in Table 4.2.

With the potential of equation (4.6) the real part of the second-order contribution composed of three terms $S_{2,i2}$, $S_{2,f2}$, $S_{2,f2i2}$ is given by:

$$S_{2,i2} = \frac{2r_c^2}{\hbar^2 \bar{v}^2} \sum_{l_1 l_2 l} \sum_{J_i' J_2'} \left(C^{J_i' 0}_{J_i 0 l_1 0}\right)^2 \left(C^{J_2' 0}_{J_2 0 l_2 0}\right)^2 f_{l_1 l_2 l}\,, \tag{4.9}$$

$$S_{2,f2i2} = -\frac{2r_c^2}{\hbar^2 \bar{v}^2} \sum_{l_1 l_2 l} (-1)^{\rho+l_2+l} D(J_i J_f; \rho\, l_1) \sum_{J_2'} \left(C^{J_2' 0_2}_{J_2 0 l_2 0}\right)^2 f_{l_1 l_2 l}\,; \tag{4.10}$$

where, the coefficients of the second-order contribution is given by $D(J_iJ_f;\rho l_1) = (-1)^{J_i+J_f} 2[(2J_i+1)\times(2J_f+1)]^{1/2} \left(C^{J_i 0}_{J_i 0 l_1 0}\right)\left(C^{J_f 0}_{J_f 0 l_1 0}\right) W(J_i J_f J_i J_f; \rho\, l_1)$ and are defined in particular by the Racah coefficients $W(J_iJ_fJ_iJ_f;\rho l_1)$; $\rho = 1$ is for the infrared absorption. The resonance functions $f_{l_1 l_2 l}$ of equation (4.9 and 4.10) shows two arguments for any given temperature. They are i) the distance of the closest approach r_c and ii) the resonance parameter $k_c = \omega r_c / \bar{v}$, so that $f_{l_1 l_2 l}$ can be expressed as:

$$f_{l_1 l_2 l} = \sum_m \frac{(l-m)!\,(l+m)!}{2^{2l}((l-m)/2)!^2\,((l+m)/2)!^2} \left| \int_1^\infty \frac{dy V_{l_1 l_2 l}(r_c y)\, y \cos[k_c A_0(y) + m\sqrt{1-V_{iso}^{\circ}(r_c)}\, A_2(y)]}{\sqrt{y^2 - 1 + V_{iso}^{\circ}(r_c) - y^2 V_{iso}^{\circ}(y r_c)}} \right|^2 \tag{4.11}$$

The integration of these functions are carried out over exact classical trajectories with the dimensionless integration variable $y = r/r_c$ and depend on the reduced isotropic potential $V_{iso}^{\circ} = 2V_{iso}/(m^{\circ}\overline{v}^2)$ where m° is the reduced mass of a pair of molecules), and on the integrals

$$A_n(y) = \int_1^y dz\ z^{-n+1}[z^2 - 1 + V_{iso}^{\circ}(r_c) - z^2 V_{iso}^{\circ}(zr_c)]^{-1/2}\ . \qquad (4.12)$$

For the line-width calculations in the present work, we have neglected the contributions coming from the imaginary part of from S_1 (vibrational dependence of the isotropic potential) and S_2 (non-commutative character of interaction at two different times) due to their very small value. The term S_1 yields, however, the dominant vibrational contribution to the pressure-induced shift of spectral lines, will be discussed below.

To govern the trajectories, analytical or numerical methods can be applied to chose the isotropic potential. The analytical form (for example Lennard-Jones 12-6) or an accurate numerical form computed from the sum of atom-atom interactions. For the analytical form, the Jacobian for the change of $bdb \rightarrow r_c dr_c$ variables in the equation (4.5) has an analytical form and can only be defined by the Lennard-Jones ε and σ parameters (given in [43]). For the numerical form, the values of the first derivative of the isotropic potential are additionally required: $bdb = r_c dr_c[1 - V_{iso}^{\circ}(r_c) - (r_c/2)dV_{iso}^{\circ}(r_c)/dr_c)]$ and are obtained by numerical derivation for the purposes of the present work. We have tried several models to test the line-shape parameters due to the fact that the calculated line-shape parameters are very sensitive to the characteristics of V_{iso}. First, the standard Lennard-Jones 12-6 form [86] (ε = 131.1 K, σ = 4.0135 Å) named "V_{iso} LJ" were tested. After that, the numerical

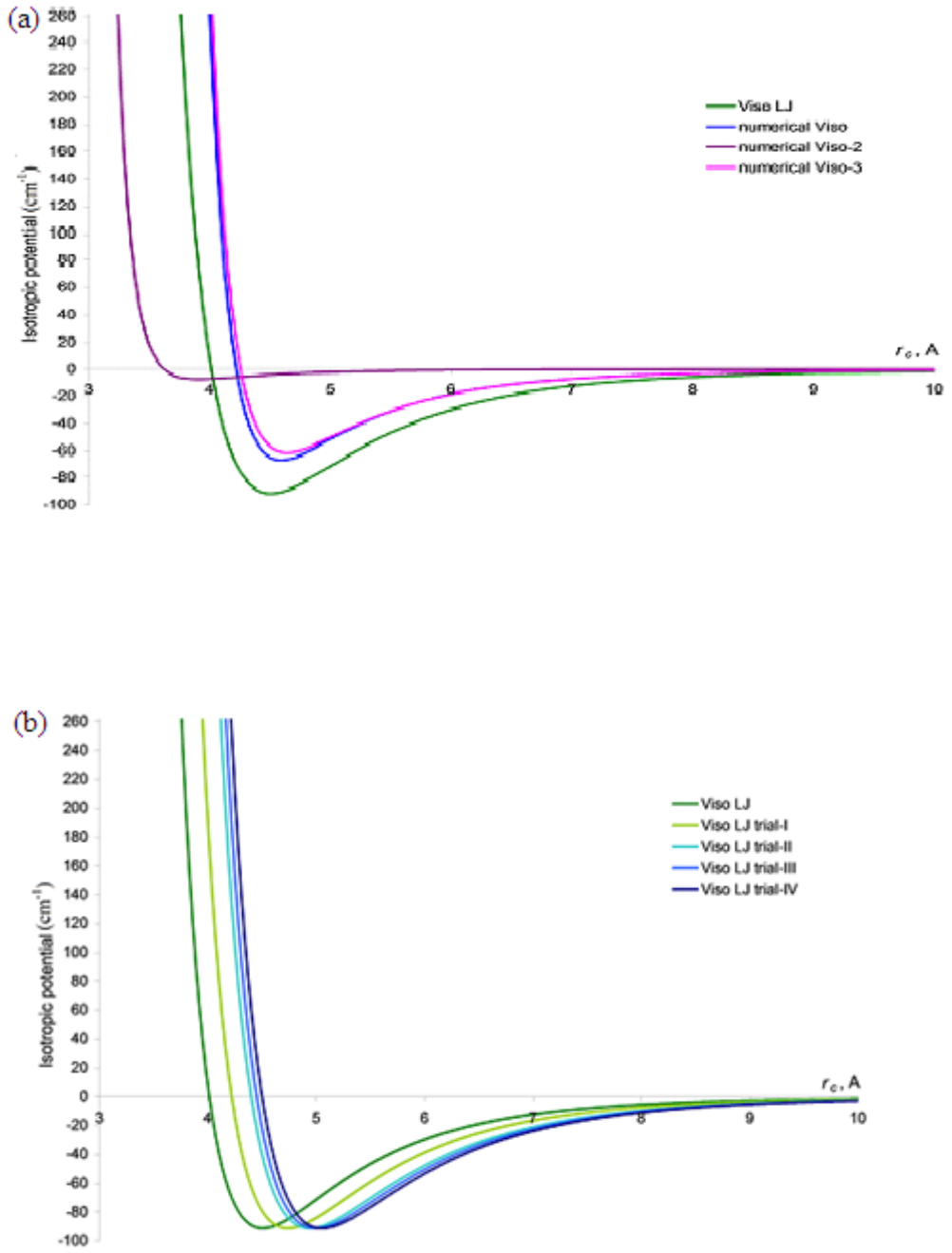

Figure 4.1: (a) Models of isotropic potential tested in preliminary computations of line broadening coefficients with parameterizations available in the literature and (b) with trial of the present work. [84]

It is difficult to find an "effective" isotropic potential that can predict a realistic value of line widths because none of the isotropic potentials have led to an accurate prediction of room-temperature line broadening coefficients for all values of the rotational quantum number (Figure 4.2 (a)). The line widths arise are mainly due to the atom-atom interactions, so for high *J*-values this interaction becomes short-range atom-atom interaction. For this reason, we have tried to decrease the contributions from these terms by keeping the same potential depth[7] $\varepsilon = 131.1$ K and increasing progressively the Lennard-Jones parameter σ (shown in Figure 4.1(b)). The increasing values of the parameters are $\sigma = 4.2$ Å ("Viso LJ trial-I" curve), $\sigma = 4.4$ Å ("Viso LJ trial-II" curve),

(a)

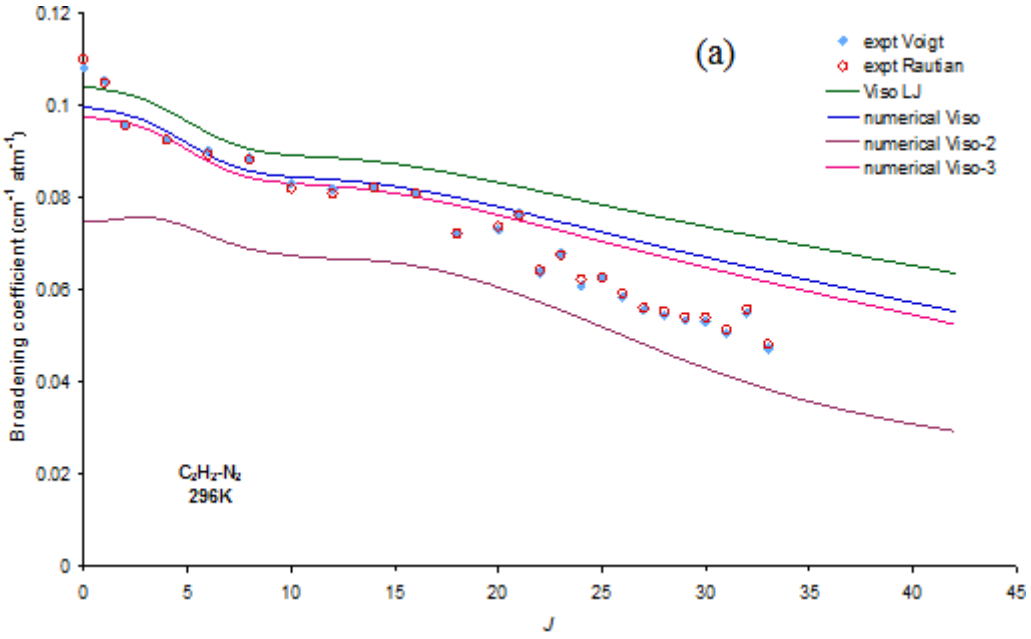

[7] For a fixed σ-value, decreasing of the potential depth ε results in an overall downward translation of the theoretical curve, so that we have not modified the initial ε-value.

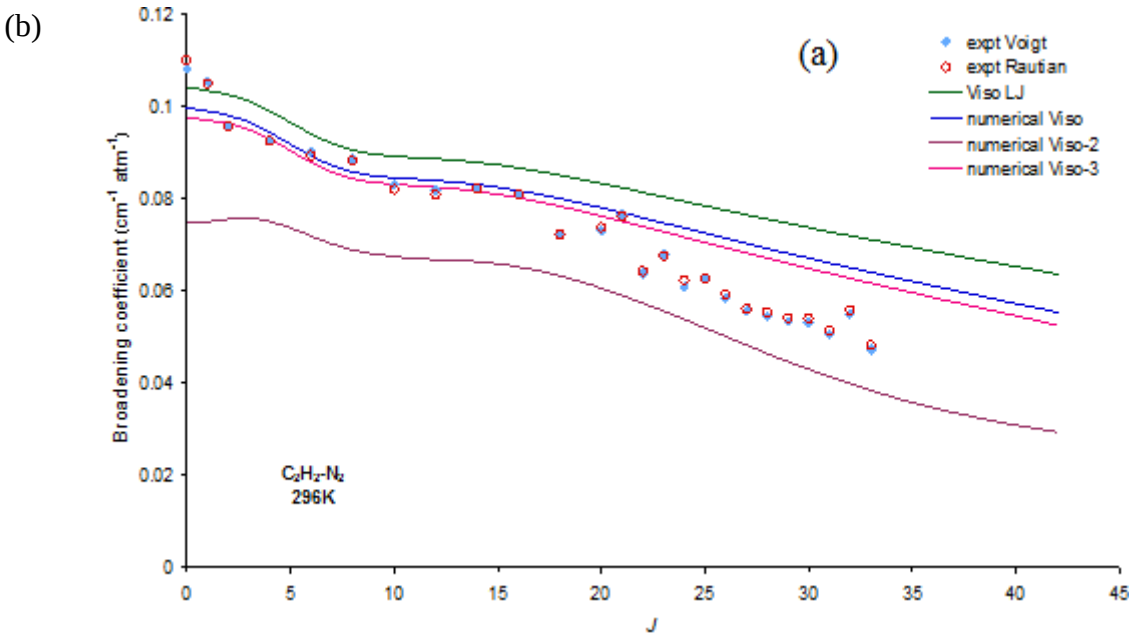

Figure 4.2: C_2H_2-N_2 line broadening coefficients calculated with the isotropic potential of Figure 4.1(a) and 4.1(b) at 296K in comparison with the experimental results of the present work. The curves without asterisk correspond to the quadrupole moment of N_2 equal to -1.3×10-26 esu cm^2 [5], the curve marked with an asterisk is obtained with Q_{N2} = -1.4×10-26 esu cm^2 [87] and the curves with double asterisk are assimilated with Q_{N2} = -1.5×10-26 esu cm^2 [91]. [84]

σ = 4.5 Å (Viso LJ trial-IV" curve) with the corresponding room-temperature line widths can be seen in Figure 4.2 (b). In this figure we can see that the agreement between experimental and numerically calculated values improves for using higher σ-values and higher J-values. In that case we have to keep in mind that these σ-values should not be too high to reduce the contributions from the electrostatic interactions for low J-values. The role of the N_2 quadrupole moment is shown for the "trial-IV" curves: Q_{N2} =1.3·10^{-26} esu cm^2 [5] (curve "Viso LJ trial-IV"), Q_{N2} = -1.4·10^{-26} esu cm^2 [94] (curve "Viso LJ trial-IV*") and Q_{N2} = -1.52·10^{-26} esu cm^2 [92] (curve "Viso LJ trial-IV**"). The best agreement between the experimental and calculated broadening coefficients is obtained for the isotropic Lennard-Jones potential with the parameters ε = 131.1 K, σ = 4.45 Å and for the nitrogen quadrupole moment with the curve "Viso LJ trial-III**" in Figure 4.2(b) given in

Ref. [92]. In order to complete the final theoretical calculations of line widths and shifts at different temperatures, we have retained the same parameterisation of the C_2H_2-N_2 interaction potential.

However, calculations of line shifts have been carried out following the procedure described in by Flygare *et al.* [94] because the vibrational dependence of isotropic or anisotropic interaction potential of C_2H_2 with N_2 is not available for any vibrational motion of the active molecule. First, the contribution coming from the vibrational dephasing S_1 term have been computed by neglecting the ImS_2 term in the second exponent of equation (4.5), and can be modelled:

$$S_1 = \frac{3}{2}\frac{\pi c\sigma}{\hbar v_c'}\frac{\Delta C_6}{C_6}\left[\frac{21}{32}\left(\frac{\sigma}{r_c}\right)^{11} y - \left(\frac{\sigma}{r_c}\right)^{5}\right] \tag{4.13}$$

with $v_c' = \bar{v}\left\{1 + 8\varepsilon/(m^{\circ}\bar{v}^{-2})[5(\sigma/r_c)^{12} - 2(\sigma/r_c)^6]\right\}^{1/2}$, and adjusted the fitting parameters $\Delta C_6/C_6$ and y on the high-J values of the experimental line-shifting coefficients at 296 K (Figure 4.3); the best overall agreement has been obtained for $\Delta C_6/C_6 = 0.005$ and $y = 0.7$. Then, the "rotational" contribution, due to ImS_2 and responsible for the asymmetry of the shift in the *R* and *P* branches, has been added, leading to slight modifications of the line shifts for low values of the rotational quantum number.

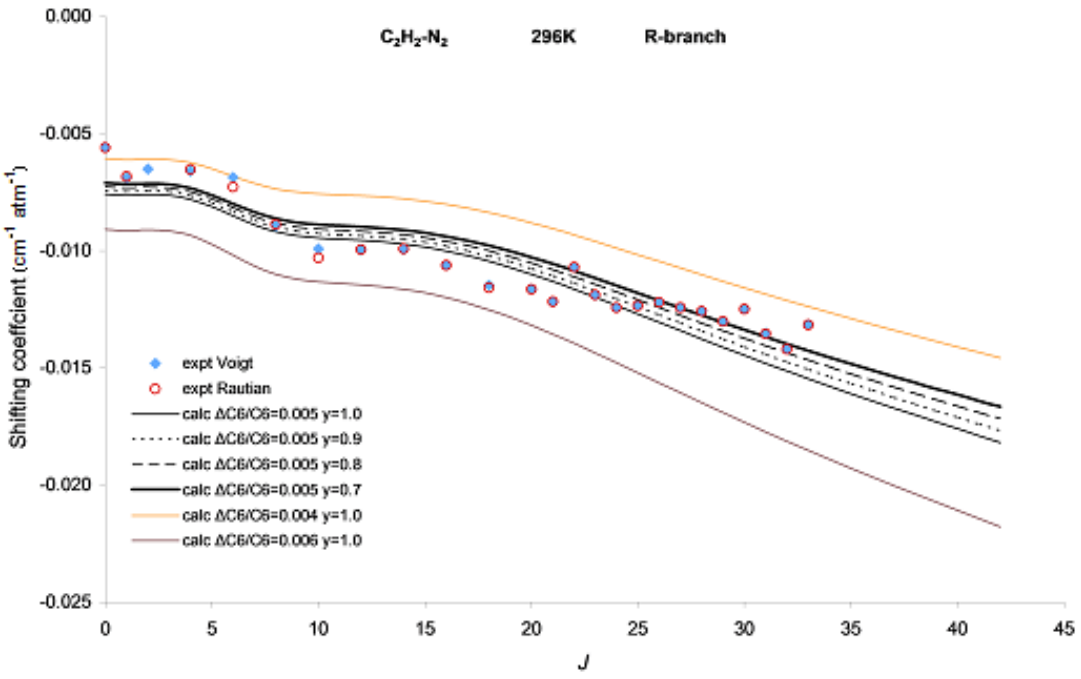

Figure 4.3: Room-temperature line-shifting coefficient calculated with the vibrational dephasing contribution for various values of fitting parameters accounting for the vibrational dependence of the isotropic potential. [84]

4.3 Spectroscopic Line Parameters

In this study, the retrieved line parameters: N_2-broadening, N_2-shift coefficients for seven different temperatures between 213 and 333 K with an increment of 20 K and their temperature dependence coefficients. The experimental N_2-broadening coefficients retrieved in the present work are presented in Table 4.3 and 4.4, with the calculated error value in bracket. Table 4.3 shows the results obtained using the Voigt model. Voigt is a convolution of Doppler and Lorentzian model that combines the effects of both thermal motion and molecular collisions. Table 4.4 shows the results retrieved using the hard-collision model which takes the narrowing effect into account. We have overlaid our experimental results with others' results. The comparison of room temperature broadening coefficients between ours (obtained with the two models) and those available in the

Table 4.3: N_2-broadening coefficients (cm^{-1} atm^{-1}) retrieved with the Voigt profile [84]

lines	m	213 K	233 K	253 K	273 K	296 K	313 K	333 K
P31	-31	0.0602(6)	0.0551(2)	0.0499(4)	0.0487(4)	0.0448(3)	0.0451(3)	0.0435(3)
P30	-30	0.0647(14)	0.0611(7)	0.0589(7)	0.0566(6)	0.0507(5)	0.0524(5)	0.0527(5)
P29	-29	0.0725(2)	0.0655(3)	0.0633(4)	0.0611(1)	0.0549(2)	0.0479(2)	0.0586(2)
P28	-28	0.0702(7)	0.0650(4)	0.0639(4)	0.0550(5)	0.0521(3)	0.0516(4)	0.0467(4)
P27	-27	0.0705(3)	0.0656(4)	0.0639(5)	0.0585(5)	0.0606(3)	0.0537(6)	0.0497(6)
P26	-26	0.0747(7)	0.0688(6)	0.0667(6)	0.0625(2)	0.0546(21)	0.0550(6)	0.0544(6)
P25	-25	0.0751(1)		0.0662(2)	0.0635(5)	0.0586(3)	0.0570(4)	0.0538(4)
P24	-24	0.0808(3)	0.0765(3)	0.0724(4)	0.0678(5)	0.0523(0)	0.0631(1)	0.0610(1)
P23	-23	0.0829(3)	0.0784(2)	0.0795(3)	0.0736(1)	0.0584(5)	0.0610(8)	0.0620(8)
P22	-22	0.0831(3)	0.0804(3)	0.0786(4)	0.0724(7)	0.0526(2)	0.0730(5)	0.0640(5)
P21	-21	0.0871(3)	0.0815(2)	0.0787(4)	0.0747(4)	0.0538(2)	0.0652(4)	0.0595(4)
P20	-20	0.0864(3)	0.0822(2)	0.0818(3)	0.0722(1)	0.0547(8)	0.0677(2)	0.0671(2)
P18	-18	0.1006(4)	0.0957(3)	0.0885(1)	0.0831(2)	0.0571(7)	0.0662(4)	0.0613(4)
P16	-16	0.0905(2)	0.0876(15)	0.0795(5)	0.0754(4)	0.0595(4)	0.0665(4)	0.0600(4)
P14	-14	0.0956(5)	0.0962(4)	0.0813(2)	0.0811(2)	0.0652(7)	0.0725(7)	0.0682(7)
P12	-12	0.0997(2)	0.0963(4)	0.0855(5)	0.0838(23)	0.0689(2)	0.0747(4)	0.0700(4)
P10	-10	0.1074(13)	0.0979(7)	0.0907(7)	0.0851(5)	0.0730(0)	0.0721(5)	0.0708(5)
P8	-8	0.1090(6)	0.1011(0)	0.0925(7)	0.0861(2)	0.0802(0)	0.0726(2)	0.0735(2)
P6	-6	0.1130(3)	0.1061(7)	0.0986(8)	0.0913(4)	0.0921(0)	0.0828(7)	0.0815(7)
P4	-4	0.1332(19)	0.1115(6)	0.1009(5)	0.0995(6)	0.0960(21)	0.0951(6)	0.0889(6)
P2	-2	0.1348(5)	0.1269(4)	0.1104(4)	0.1125(2)	0.1022(4)	0.1000(8)	0.0922(8)
P1	-1	0.1455(7)	0.1303(1)	0.1208(6)	0.1147(3)	0.1057(19)	0.1044(8)	0.0970(8)
R0	1	0.1428(10)	0.1355(10)	0.1210(19)	0.1129(23)	0.1081(7)	0.1065(6)	0.1005(15)
R1	2	0.1350(35)	0.1304(17)	0.1147(19)	0.1123(17)	0.1053(13)	0.1071(7)	0.0997(8)
R2	3	0.1282(10)	0.1191(4)	0.1103(10)	0.1052(7)	0.0957(9)	0.0925(6)	0.0878(5)
R4	5	0.1227(14)	0.1176(12)	0.1058(12)	0.1044(6)	0.0928(6)	0.0914(5)	0.0857(5)
R6	7	0.1126(22)	0.1075(11)	0.0972(26)	0.0998(14)	0.0902(7)	0.0829(13)	0.0778(10)
R8	9	0.1062(14)	0.1056(12)	0.0905(24)	0.0996(6)	0.0885(3)	0.0835(7)	0.0786(6)
R10	11	0.1011(19)	0.0972(24)	0.0898(21)	0.0907(7)	0.0830(2)	0.0797(5)	0.0738(9)
R12	13	0.1032(6)	0.1015(7)	0.0893(8)	0.0870(11)	0.0817(8)	0.0823(5)	0.0736(6)
R14	15	0.1002(7)	0.0973(6)	0.0868(11)	0.0860(5)	0.0822(4)	0.0820(9)	0.0738(7)
R16	17	0.1013(2)	0.0967(3)	0.0896(2)	0.0818(5)	0.0810(3)	0.0778(2)	0.0713(4)
R18	19	0.0932(3)	0.0892(3)	0.0872(1)	0.0824(3)	0.0723(5)	0.0724(3)	0.0692(3)
R20	21	0.0877(5)	0.0814(3)	0.0805(1)	0.0708(3)	0.0730(3)	0.0708(4)	0.0643(3)
R21	22	0.0883(4)	0.0871(3)	0.0839(4)	0.0793(4)	0.0766(4)	0.0707(5)	0.0701(4)
R22	23	0.0804(5)	0.0740(3)	0.0707(3)	0.0672(2)	0.0638(3)	0.0626(2)	0.0592(2)
R23	24	0.0793(3)	0.0774(3)	0.0742(3)	0.0693(4)	0.0678(3)	0.0648(3)	0.0628(4)
R24	25	0.0760(4)	0.0706(5)	0.0691(5)	0.0653(3)	0.0608(3)	0.0600(2)	0.0566(2)
R25	26	0.0748(2)	0.0712(1)	0.0674(2)	0.0643(2)	0.0626(1)	0.0606(1)	0.0579(2)
R26	27	0.0752(6)	0.0670(5)	0.0633(3)	0.0569(4)	0.0586(2)	0.0556(2)	0.0554(2)
R27	28	0.0659(4)	0.0624(3)	0.0598(3)	0.0576(2)	0.0556(4)	0.0549(2)	0.0535(2)
R28	29	0.0648(5)	0.0625(3)	0.0601(3)	0.0566(1)	0.0545(2)	0.0529(2)	0.0500(2)
R29	30	0.0627(7)	0.0599(5)	0.0571(2)	0.0554(1)	0.0534(1)	0.0513(1)	0.0489(1)
R30	31	0.0560(17)	0.0616(11)	0.0570(8)	0.0537(3)	0.0531(5)	0.0483(4)	0.0479(3)
R31	32	0.0614(3)	0.0581(3)	0.0522(3)	0.0518(2)	0.0505(2)	0.0472(2)	0.0460(2)
R32	33	0.0880(13)	0.0661(13)	0.0595(11)	0.0546(8)	0.0550(7)	0.0513(6)	0.0400(4)
R33	34	0.0577(16)	0.0550(8)	0.0494(7)	0.0478(3)	0.0472(3)	0.0442(2)	0.0413(4)

Table 4.4: N_2-broadening coefficients (cm^{-1} atm^{-1}) retrieved with the Hard collision profile [84]

lines	m	213 K	233 K	253 K	273 K	296 K	313 K	333 K
P31	-31	0.0610(8)	0.0554(3)	0.0507(6)	0.0494(5)	0.0416(5)	0.0460(5)	0.0443(4)
P30	-30	0.0652(16)	0.0616(10)	0.0595(9)	0.0573(9)	0.0441(6)	0.0532(7)	0.0535(10)
P29	-29	0.0728(3)	0.0660(5)	0.0639(5)	0.0614(2)	0.0513(1)	0.0485(2)	0.0586(4)
P28	-28	0.0707(11)	0.0657(5)	0.0646(6)	0.0558(8)	0.0541(0)	0.0527(6)	0.0476(9)
P27	-27	0.0712(5)	0.0664(5)	0.0645(7)	0.0588(7)	0.0608(1)	0.0542(9)	0.0500(2)
P26	-26	0.0751(10)	0.0693(9)	0.0672(9)	0.0633(3)	0.0580(7)	0.0558(9)	0.0551(10)
P25	-25	0.0739(3)		0.0666(3)	0.0638(7)	0.0613(1)	0.0571(7)	0.0538(6)
P24	-24	0.0812(4)	0.0768(4)	0.0728(6)	0.0683(6)	0.0611(8)	0.0629(1)	0.0616(4)
P23	-23	0.0830(5)	0.0785(3)	0.0795(5)	0.0735(1)	0.0627(4)	0.0606(17)	0.0633(10)
P22	-22	0.0834(4)	0.0808(4)	0.0790(6)	0.0726(10)	0.0632(3)	0.0734(7)	0.0644(6)
P21	-21	0.0871(3)	0.0813(7)	0.0782(8)	0.0741(7)	0.0640(6)	0.0653(5)	0.0583(11)
P20	-20	0.0866(4)	0.0824(3)	0.0820(4)	0.0725(1)	0.0687(6)	0.0683(3)	0.0674(9)
P18	-18	0.1007(4)	0.0958(4)	0.0885(1)	0.0831(3)	0.0715(0)	0.0663(6)	0.0614(7)
P16	-16	0.0902(4)	0.0872(28)	0.0791(9)	0.0750(5)	0.0730(5)	0.0660(8)	0.0595(4)
P14	-14	0.0951(14)	0.0958(9)	0.0813(2)	0.0806(3)	0.0749(10)	0.0720(15)	0.0679(4)
P12	-12	0.0995(8)	0.0940(13)	0.0855(5)	0.0836(48)	0.0783(14)	0.0742(11)	0.0694(13)
P10	-10	0.1074(13)	0.0979(8)	0.0907(8)	0.0851(4)	0.0836(5)	0.0704(10)	0.0694(8)
P8	-8	0.1090(6)	0.1008(16)	0.0925(8)	0.0858(4)	0.0893(8)	0.0719(5)	0.0728(9)
P6	-6	0.1128(11)	0.1061(9)	0.0985(23)	0.0908(7)	0.0964(7)	0.0824(12)	0.0812(7)
P4	-4	0.1324(24)	0.1116(9)	0.1006(11)	0.0994(9)	0.0990(8)	0.0951(10)	0.0890(5)
P2	-2	0.1349(8)	0.1270(6)	0.1105(7)	0.1127(2)	0.1071(8)	0.1003(12)	0.0927(6)
P1	-1	0.1498(15)	0.1302(12)	0.1207(9)	0.1147(4)	0.1080(14)	0.1044(6)	0.0972(6)
R0	1	0.1430(10)	0.1360(10)	0.1214(19)	0.1133(22)	0.1100(7)	0.1068(6)	0.1015(15)
R1	2	0.1347(35)	0.1298(17)	0.1141(19)	0.1118(17)	0.1050(13)	0.1069(7)	0.0993(8)
R2	3	0.1280(11)	0.1191(4)	0.1103(10)	0.1053(6)	0.0958(9)	0.0929(6)	0.0881(5)
R4	5	0.1224(14)	0.1174(12)	0.1054(12)	0.1041(6)	0.0925(7)	0.0914(5)	0.0858(5)
R6	7	0.1120(22)	0.1064(11)	0.0967(26)	0.0992(15)	0.0893(15)	0.0829(13)	0.0774(10)
R8	9	0.1053(14)	0.1051(12)	0.0898(24)	0.0990(6)	0.0882(3)	0.0828(7)	0.0780(7)
R10	11	0.1000(19)	0.0970(24)	0.0890(21)	0.0903(7)	0.0820(5)	0.0797(5)	0.0730(9)
R12	13	0.1030(6)	0.1012(7)	0.0889(8)	0.0863(11)	0.0809(8)	0.0819(5)	0.0729(6)
R14	15	0.0999(7)	0.0971(6)	0.0863(11)	0.0858(5)	0.0821(4)	0.0817(9)	0.0737(7)
R16	17	0.1012(2)	0.0934(3)	0.0895(2)	0.0816(5)	0.0809(3)	0.0778(2)	0.0711(4)
R18	19	0.0933(3)	0.0892(3)	0.0873(1)	0.0828(2)	0.0723(5)	0.0725(3)	0.0692(3)
R20	21	0.0879(5)	0.0817(3)	0.0807(1)	0.0709(3)	0.0737(3)	0.0687(4)	0.0645(3)
R21	22	0.0881(4)	0.0869(3)	0.0836(4)	0.0788(4)	0.0762(4)	0.0692(6)	0.0694(4)
R22	23	0.0808(5)	0.0744(3)	0.0711(3)	0.0672(2)	0.0642(3)	0.0628(2)	0.0596(2)
R23	24	0.0795(3)	0.0775(3)	0.0741(1)	0.0691(4)	0.0676(3)	0.0644(4)	0.0623(4)
R24	25	0.0765(4)	0.0712(5)	0.0696(4)	0.0659(3)	0.0623(1)	0.0606(2)	0.0571(2)
R25	26	0.0752(2)	0.0716(1)	0.0678(2)	0.0643(2)	0.0628(1)	0.0608(1)	0.0580(2)
R26	27	0.0758(6)	0.0677(5)	0.0641(3)	0.0550(3)	0.0592(2)	0.0565(2)	0.0560(2)
R27	28	0.0667(3)	0.0630(3)	0.0604(3)	0.0582(2)	0.0561(4)	0.0554(1)	0.0540(2)
R28	29	0.0654(5)	0.0631(3)	0.0609(3)	0.0572(1)	0.0553(2)	0.0537(2)	0.0512(2)
R29	30	0.0635(7)	0.0607(5)	0.0580(2)	0.0559(1)	0.0540(1)	0.0521(1)	0.0497(1)
R30	31	0.0568(17)	0.0623(11)	0.0579(7)	0.0544(3)	0.0540(5)	0.0494(4)	0.0490(3)
R31	32	0.0620(3)	0.0588(3)	0.0529(3)	0.0522(1)	0.0514(2)	0.0480(2)	0.0469(1)
R32	33	0.0879(55)	0.0666(13)	0.0604(11)	0.0552(8)	0.0557(7)	0.0520(6)	0.0412(3)
R33	34	0.0584(16)	0.0558(8)	0.0504(7)	0.0488(3)	0.0482(3)	0.0452(2)	0.0425(3)

Table 4.5: N_2-broadening coefficients ($cm^{-1}atm^{-1}$) calculated with the semi-classical approach. [84]

lines	*J*	213 K	233 K	253 K	273 K	296 K	313 K	333 K
R0	0	0.1296	0.1198	0.1114	0.1042	0.0973	0.0929	0.0879
R1	1	0.1285	0.1189	0.1107	0.1035	0.0967	0.0923	0.0873
R2	2	0.1277	0.1184	0.1103	0.1033	0.0965	0.0922	0.0873
R3	3	0.1254	0.1166	0.1090	0.1022	0.0957	0.0916	0.0868
R4	4	0.1218	0.1135	0.1063	0.1000	0.0939	0.0900	0.0855
R5	5	0.1173	0.1095	0.1028	0.0968	0.0911	0.0875	0.0833
R6	6	0.1131	0.1055	0.0991	0.0934	0.0880	0.0846	0.0806
R7	7	0.1101	0.1025	0.0960	0.0905	0.0852	0.0819	0.0781
R8	8	0.1085	0.1007	0.0941	0.0885	0.0832	0.0799	0.0761
R9	9	0.1079	0.1000	0.0932	0.0875	0.0821	0.0787	0.0748
R10	10	0.1076	0.0996	0.0928	0.0870	0.0815	0.0781	0.0741
R11	11	0.1072	0.0993	0.0926	0.0867	0.0812	0.0778	0.0738
R12	12	0.1064	0.0988	0.0922	0.0864	0.0810	0.0775	0.0736
R13	13	0.1052	0.0979	0.0915	0.0859	0.0806	0.0772	0.0733
R14	14	0.1036	0.0967	0.0906	0.0852	0.0800	0.0767	0.0729
R15	15	0.1015	0.0951	0.0893	0.0842	0.0793	0.0761	0.0724
R16	16	0.0990	0.0932	0.0878	0.0829	0.0782	0.0752	0.0717
R17	17	0.0962	0.0909	0.0859	0.0814	0.0770	0.0742	0.0708
R18	18	0.0932	0.0884	0.0839	0.0797	0.0756	0.0729	0.0697
R19	19	0.0899	0.0857	0.0816	0.0778	0.0739	0.0715	0.0685
R20	20	0.0865	0.0829	0.0792	0.0757	0.0722	0.0699	0.0671
R21	21	0.0831	0.0799	0.0766	0.0735	0.0703	0.0683	0.0657
R22	22	0.0796	0.0769	0.0740	0.0712	0.0683	0.0665	0.0641
R23	23	0.0760	0.0738	0.0714	0.0689	0.0663	0.0647	0.0625
R24	24	0.0726	0.0708	0.0687	0.0665	0.0642	0.0628	0.0608
R25	25	0.0692	0.0678	0.0660	0.0641	0.0621	0.0609	0.0591
R26	26	0.0659	0.0649	0.0634	0.0618	0.0600	0.0589	0.0573
R27	27	0.0628	0.0620	0.0608	0.0595	0.0580	0.0570	0.0556
R28	28	0.0597	0.0593	0.0583	0.0572	0.0559	0.0551	0.0539
R29	29	0.0567	0.0566	0.0559	0.0550	0.0539	0.0533	0.0522
R30	30	0.0539	0.0540	0.0535	0.0528	0.0519	0.0514	0.0505
R31	31	0.0512	0.0515	0.0512	0.0507	0.0500	0.0497	0.0488
R32	32	0.0485	0.0491	0.0490	0.0486	0.0482	0.0479	0.0472
R33	33	0.0460	0.0467	0.0469	0.0467	0.0464	0.0462	0.0456

literature are plotted in Figure 4.4. For the room temperature coefficients, we have also plotted the comparison with the theoretical results (calculation details given in Sec. 4.2). We have display the results as a function of the quantum number *m* index where $m = -J''$ is for the P branch and $m = J'' + 1$ is for the R branch. Our theoretical results presented in Table 4.5 are in the numerical values, compare very favourably with all sets of experimental data. Broadening coefficients values show a good agreement with the values reported in other works (literature) and with our calculated values. The N_2-broadening parameters increases with the increasing m index for the P branch and decreases with the increasing m index the R branch.

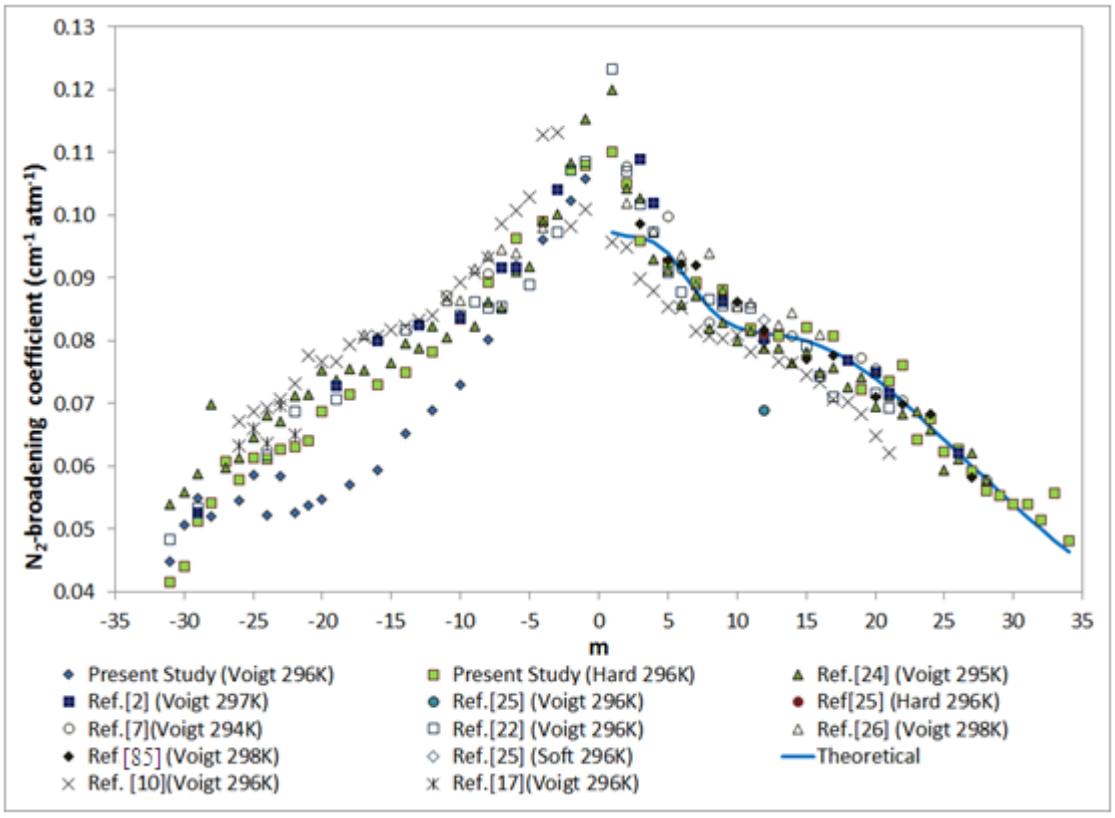

Figure 4.4: Room temperature N_2-broadening coefficient of C_2H_2 transitions (present study and published results) as a function of m, where $m = -J''$ for the P-branch and $m = J''+1$ for the R-branch lines. [84]

In the similar manner as the N_2-broadening coefficients, the N_2-pressure induced shift coefficients are also retrieved for seven different temperatures between 213 and 333 K with an increment of 20 K. Shift coefficients retrieved using Voigt profile are listed in Table 4.6 and the hard-collision profile in Table 4.7. The calculated semi-classical values are given in Table 4.8. A comparison of our results with the calculated one and those available in the literature for the room-temperature are shown in Figure 4.5.

The temperature-dependence exponents (coefficient), *n*, of N_2-broadening coefficients were calculated using equation (4.1) for both Voigt and hard-collision models. The results are presented in Table 4.9 and plotted in Figure 4.6 along with values issued from our calculated N_2-broadening coefficients. Both, the table and the plot shows P- and R- branches in the case of experimental and only R-branch in the case of theoretical. Theoretical temperature dependence coefficient for m > 22 are not shown because of insufficient quality of linear regression analysis. Within the considered range of *m*-values, we notice a good agreement between theoretical and experimental values of *n* exponents.

Two different equation were implemented in order to calculate the temperature dependencies in N_2-shifts: a linear and a quadratic equation. The linear expression is given in equation (4.3) and the quadratic expression is given in (4.4). The results are listed for linear and quadratic case in Tables 4.10 and 4.11, respectively, together with theoretical values deduced from the semi-classically calculated line shifts. The results from Table 4.10 are plotted in Figure 4.7(a) and from Table 4.11 in Figures 4.7(b) and 4.7(c). According to the three panels in Figure 4.7, the quadratic expression gives a better agreement between experimental and theoretical temperature dependencies of N_2-shift coefficients than the linear one.

Table 4.6: N_2-shift coefficients (cm^{-1} atm^{-1}) retrieved with the Voigt profile [84].

lines	m	213K	233K	253K	273K	296K	313K	333K
P(31)	-31	-0.0135(6)	-0.0126(2)	-0.0131(4)	-0.0124(4)	-0.0116(3)	-0.0122(3)	-0.0119(3)
P(30)	-30	-0.0132(14)	-0.0121(7)	-0.0119(7)	-0.0117(6)	-0.0091(5)	-0.0121(5)	-0.0102(7)
P(29)	-29	-0.0134(2)	-0.0134(3)	-0.0137(4)	-0.0126(1)	-0.0108(2)	-0.0096(2)	-0.0124(3)
P(28)	-28	-0.0120(7)	-0.0121(4)	-0.0120(4)	-0.0113(5)	-0.0110(3)	-0.0122(4)	-0.0113(6)
P(27)	-27	-0.0129(3)	-0.0124(4)	-0.0125(5)	-0.0116(5)	-0.0113(3)	-0.0117(6)	-0.0107(2)
P(26)	-26	-0.0126(7)	-0.0124(6)	-0.0119(6)	-0.0118(2)	-0.0102(21)	-0.0116(6)	-0.0109(7)
P(25)	-25	-0.0127(1)	-0.0103(34)	-0.0118(2)	-0.0116(5)	-0.0119(3)	-0.0113(4)	-0.0108(3)
P(24)	-24	-0.0120(3)	-0.0122(3)	-0.0115(4)	-0.0119(5)	-0.0092(0)	-0.0113(1)	-0.0107(3)
P(23)	-23	-0.0125(3)	-0.0123(2)	-0.0117(3)	-0.0114(1)	-0.0116(5)	-0.0109(8)	-0.0102(5)
P(22)	-22	-0.0121(3)	-0.0118(3)	-0.0117(4)	-0.0112(7)	-0.0111(2)	-0.0111(5)	-0.0102(4)
P(21)	-21	-0.0125(3)	-0.0123(2)	-0.0113(4)	-0.0106(4)	-0.0130(2)	-0.0108(4)	-0.0100(4)
P(20)	-20	-0.0114(3)	-0.0113(2)	-0.0107(3)	-0.0109(1)	-0.0108(8)	-0.0114(2)	-0.0100(6)
P(18)	-18	-0.0116(4)	-0.0117(3)	-0.0116(1)	-0.0119(2)	-0.0128(7)	-0.0123(4)	-0.0123(5)
P(16)	-16	-0.0108(2)	-0.0114(15)	-0.0108(5)	-0.0121(4)	-0.0096(4)	-0.0102(4)	-0.0095(2)
P(14)	-14	-0.0118(5)	-0.0102(4)	-0.0100(2)	-0.0119(2)	-0.0095(7)	-0.0091(7)	-0.0083(2)
P(12)	-12	-0.0114(2)	-0.0110(4)	-0.0102(5)	-0.0114(23)	-0.0091(2)	-0.0090(4)	-0.0084(6)
P(10)	-10	-0.0112(13)	-0.0105(7)	-0.0093(7)	-0.0110(5)	-0.0090(0)	-0.0088(5)	-0.0081(4)
P(8)	-8	-0.0110(6)		-0.0089(7)	-0.0105(2)	-0.0096(0)	-0.0077(2)	-0.0072(5)
P(6)	-6	-0.0083(3)	-0.0082(7)	-0.0080(8)	-0.0162(4)	-0.0075(0)	-0.0073(7)	-0.0067(4)
P(4)	-4	-0.0082(19)	-0.0081(6)	-0.0078(5)	-0.0079(6)	-0.0067(21)	-0.0065(6)	-0.0070(3)
P(2)	-2	-0.0076(5)	-0.0076(4)	-0.0072(4)	-0.0073(2)	-0.0060(4)	-0.0055(8)	-0.0063(4)
P(1)	-1	-0.0074(7)	-0.0076(1)	-0.0073(6)	-0.0072(3)	-0.0024(19)	-0.0066(8)	-0.0063(5)
R(0)	1	-0.0051(7)	-0.0045(7)	-0.0039(13)	-0.0012(15)	-0.0056(7)	-0.0037(4)	-0.0041(10)
R(1)	2	-0.0067(9)	-0.0064(5)	-0.0036(6)	-0.0060(6)	-0.0069(7)	-0.0064(3)	-0.0053(4)
R(2)	3	-0.0069(5)	-0.0067(2)	-0.0057(5)	-0.0067(3)	-0.0065(6)	-0.0059(4)	-0.0060(4)
R(4)	5	-0.0049(5)	-0.0068(5)	-0.0057(5)	-0.0079(3)	-0.0066(4)	-0.0061(3)	-0.0055(3)
R(6)	7	-0.0066(4)	-0.0072(4)	-0.0060(8)	-0.0064(6)	-0.0069(6)	-0.0063(6)	-0.0059(5)
R(8)	9	-0.0079(4)	-0.0077(4)	-0.0072(8)	-0.0088(3)	-0.0089(2)	-0.0070(3)	-0.0064(3)
R(10)	11	-0.0090(5)	-0.0079(6)	-0.0073(6)	-0.0100(2)	-0.0099(1)	-0.0077(2)	-0.0073(3)
R(12)	13	-0.0111(2)	-0.0098(2)	-0.0095(2)	-0.0103(4)	-0.0100(4)	-0.0086(2)	-0.0081(3)
R(14)	15	-0.0120(3)	-0.0122(3)	-0.0099(4)	-0.0109(2)	-0.0100(2)	-0.0092(4)	-0.0089(3)
R(16)	17	-0.0137(1)	-0.0131(2)	-0.0121(1)	-0.0116(2)	-0.0106(2)	-0.0098(1)	-0.0094(2)
R(18)	19	-0.0149(2)	-0.0137(2)	-0.0123(0)	-0.0117(2)	-0.0115(4)	-0.0105(2)	-0.0096(2)
R(20)	21	-0.0151(3)	-0.0139(2)	-0.0126(1)	-0.0120(3)	-0.0116(2)	-0.0098(3)	-0.0098(2)
R(21)	22	-0.0152(2)	-0.0143(2)	-0.0136(3)	-0.0123(3)	-0.0122(4)	-0.0112(4)	-0.0103(3)
R(22)	23	-0.0163(4)	-0.0147(2)	-0.0140(2)	-0.0129(2)	-0.0107(3)	-0.0120(2)	-0.0109(2)
R(23)	24	-0.0163(2)	-0.0152(2)	-0.0140(2)	-0.0129(2)	-0.0119(3)	-0.0121(2)	-0.0111(2)
R(24)	25	-0.0162(3)	-0.0147(3)	-0.0146(3)	-0.0133(2)	-0.0124(1)	-0.0116(2)	-0.0105(2)
R(25)	26	-0.0168(1)	-0.0154(1)	-0.0151(1)	-0.0135(1)	-0.0124(1)	-0.0112(1)	-0.0105(1)
R(26)	27	-0.0176(4)	-0.0161(2)	-0.0157(2)	-0.0139(3)	-0.0122(2)	-0.0121(1)	-0.0115(1)
R(27)	28	-0.0174(2)	-0.0160(2)	-0.0156(2)	-0.0140(2)	-0.0124(3)	-0.0125(1)	-0.0118(1)
R(28)	29	-0.0176(3)	-0.0162(2)	-0.0162(2)	-0.0144(1)	-0.0126(2)	-0.0122(2)	-0.0114(1)
R(29)	30	-0.0176(4)	-0.0163(3)	-0.0164(1)	-0.0142(1)	-0.0130(1)	-0.0134(1)	-0.0128(1)
R(30)	31	-0.0174(10)	-0.0164(7)	-0.0159(5)	-0.0141(2)	-0.0125(3)	-0.0123(2)	-0.0122(2)
R(31)	32	-0.0176(2)	-0.0162(2)	-0.0163(2)	-0.0146(1)	-0.0135(2)	-0.0131(1)	-0.0123(1)
R(32)	33	-0.0139(9)	-0.0141(9)	-0.0156(8)	-0.0137(4)	-0.0142(7)	-0.0118(3)	-0.0118(2)
R(33)	34	-0.0175(10)	-0.0166(6)	-0.0167(4)	-0.0150(2)	-0.0132(2)	-0.0135(2)	-0.0124(2)

Table 4.7: N_2-shift coefficients (cm^{-1} atm^{-1}) retrieved with the hard-collision profile [84].

lines	m	213K	233K	253K	273K	296K	313K	333K
P(31)	-31	-0.0135(6)	-0.0126(2)	-0.0130(4)	-0.0124(4)	-0.0112(7)	-0.0122(3)	-0.0119(3)
P(30)	-30	-0.0131(10)	-0.0121(7)	-0.0119(7)	-0.0117(6)	-0.0097(18)	-0.0121(5)	-0.0102(7)
P(29)	-29	-0.0134(2)	-0.0134(3)	-0.0136(4)	-0.0126(1)	-0.0120(1)	-0.0096(2)	-0.0124(3)
P(28)	-28	-0.0121(7)	-0.0121(4)	-0.0120(4)	-0.0113(5)	-0.0119(2)	-0.0122(4)	-0.0113(6)
P(27)	-27	-0.0128(3)	-0.0124(4)	-0.0124(5)	-0.0116(5)	-0.0107(2)	-0.0117(6)	-0.0107(2)
P(26)	-26	-0.0126(7)	-0.0124(6)	-0.0119(6)	-0.0118(3)	-0.0102(7)	-0.0116(6)	-0.0109(7)
P(25)	-25	-0.0128(2)		-0.0118(2)	-0.0116(5)	-0.0113(1)	-0.0113(4)	-0.0108(4)
P(24)	-24	-0.0120(3)	-0.0122(3)	-0.0115(4)	-0.0120(5)	-0.0096(36)	-0.0100(0)	-0.0107(3)
P(23)	-23	-0.0125(3)	-0.0123(2)	-0.0117(3)	-0.0114(1)	-0.0100(4)	-0.0109(8)	-0.0103(5)
P(22)	-22	-0.0121(3)	-0.0118(3)	-0.0117(4)	-0.0112(7)	-0.0096(0)	-0.0111(5)	-0.0102(4)
P(21)	-21	-0.0125(2)	-0.0123(3)	-0.0113(4)	-0.0106(4)	-0.0122(2)	-0.0108(4)	-0.0100(4)
P(20)	-20	-0.0114(3)	-0.0113(2)	-0.0107(3)	-0.0109(1)	-0.0104(4)	-0.0114(2)	-0.0100(6)
P(18)	-18	-0.0116(4)	-0.0117(3)	-0.0117(1)	-0.0119(2)	-0.0120(0)	-0.0124(4)	-0.0124(5)
P(16)	-16	-0.0136(2)	-0.0114(15)	-0.0108(5)	-0.0121(4)	-0.0098(2)	-0.0102(4)	-0.0095(2)
P(14)	-14	-0.0118(5)	-0.0102(4)	-0.0100(2)	-0.0119(2)	-0.0094(4)	-0.0092(7)	-0.0083(2)
P(12)	-12	-0.0114(2)	-0.0110(4)	-0.0102(5)	-0.0114(23)	-0.0107(0)	-0.0090(4)	-0.0084(6)
P(10)	-10	-0.0112(13)	-0.0105(7)	-0.0093(8)	-0.0110(5)	-0.0091(0)	-0.0088(5)	-0.0081(4)
P(8)	-8	-0.0110(6)		-0.0089(7)	-0.0105(2)	-0.0099(0)	-0.0076(2)	-0.0071(5)
P(6)	-6	-0.0083(3)	-0.0072(8)	-0.0080(8)	-0.0161(4)	-0.0068(6)	-0.0073(7)	-0.0066(4)
P(4)	-4	-0.0082(19)	-0.0081(6)	-0.0081(5)	-0.0079(6)	-0.0065(7)	-0.0065(6)	-0.0070(3)
P(2)	-2	-0.0076(5)	-0.0076(4)	-0.0072(4)	-0.0074(2)	-0.0050(4)	-0.0055(8)	-0.0063(4)
P(1)	-1	-0.0074(7)	-0.0076(7)	-0.0074(6)	-0.0073(3)	-0.0019(17)	-0.0066(8)	-0.0064(5)
R(0)	1	-0.0051(7)	-0.0045(7)	-0.0039(13)	-0.0012(15)	-0.0056(7)	-0.0037(4)	-0.0041(0)
R(1)	2	-0.0067(5)	-0.0063(5)	-0.0035(6)	-0.0059(6)	-0.0068(7)	-0.0063(3)	-0.0053(4)
R(2)	3	-0.0069(2)	-0.0067(2)	-0.0057(5)	-0.0067(3)		-0.0059(4)	-0.0060(4)
R(4)	5	-0.0049(5)	-0.0068(5)	-0.0057(5)	-0.0079(3)	-0.0065(4)	-0.0060(3)	-0.0055(3)
R(6)	7	-0.0055(4)	-0.0073(4)	-0.0061(8)	-0.0064(6)	-0.0073(9)	-0.0063(6)	-0.0060(5)
R(8)	9	-0.0079(4)	-0.0075(4)	-0.0073(8)	-0.0088(3)	-0.0089(2)	-0.0070(3)	-0.0064(3)
R(10)	11	-0.0090(6)	-0.0080(6)	-0.0074(6)	-0.0100(2)	-0.0103(2)	-0.0077(2)	-0.0075(3)
R(12)	13	-0.0111(2)	-0.0098(3)	-0.0095(2)	-0.0103(4)	-0.0100(4)	-0.0086(2)	-0.0081(3)
R(14)	15	-0.0111(3)	-0.0123(3)	-0.0099(4)	-0.0108(2)	-0.0099(2)	-0.0092(4)	-0.0089(3)
R(16)	17	-0.0137(2)	-0.0131(2)	-0.0120(1)	-0.0115(2)	-0.0106(2)	-0.0098(1)	-0.0094(2)
R(18)	19	-0.0149(2)	-0.0137(2)	-0.0123(0)	-0.0116(1)	-0.0116(4)	-0.0105(2)	-0.0097(2)
R(20)	21	-0.0151(2)	-0.0139(2)	-0.0126(1)	-0.0118(2)	-0.0117(2)	-0.0098(3)	-0.0098(2)
R(21)	22	-0.0152(2)	-0.0143(2)	-0.0135(3)	-0.0123(3)	-0.0122(3)	-0.0112(3)	-0.0103(3)
R(22)	23	-0.0163(2)	-0.0147(2)	-0.0140(2)	-0.0128(1)	-0.0107(3)	-0.0119(1)	-0.0109(2)
R(23)	24	-0.0163(2)	-0.0152(2)	-0.0140(2)	-0.0129(2)	-0.0119(2)	-0.0121(2)	-0.0111(2)
R(24)	25	-0.0162(3)	-0.0147(3)	-0.0146(3)	-0.0133(2)	-0.0124(1)	-0.0117(2)	-0.0105(2)
R(25)	26	-0.0168(1)	-0.0154(1)	-0.0151(1)	-0.0134(1)	-0.0124(1)	-0.0112(1)	-0.0105(1)
R(26)	27	-0.0176(2)	-0.0160(3)	-0.0157(2)	-0.0138(3)	-0.0122(2)	-0.0121(1)	-0.0115(1)
R(27)	28	-0.0174(2)	-0.0160(2)	-0.0156(2)	-0.0140(2)	-0.0124(3)	-0.0124(1)	-0.0118(1)
R(28)	29	-0.0176(2)	-0.0162(2)	-0.0162(2)	-0.0144(1)	-0.0126(2)	-0.0122(1)	-0.0114(1)
R(29)	30	-0.0177(3)	-0.0164(3)	-0.0164(1)	-0.0142(1)	-0.0130(1)	-0.0134(1)	-0.0128(1)
R(30)	31	-0.0174(7)	-0.0164(7)	-0.0159(5)	-0.0141(2)	-0.0125(3)	-0.0123(2)	-0.0122(2)
R(31)	32	-0.0176(2)	-0.0162(2)	-0.0163(2)	-0.0144(1)	-0.0136(2)	-0.0131(1)	-0.0123(1)
R(32)	33	-0.0140(9)	-0.0141(9)	-0.0156(8)	-0.0136(4)	-0.0142(6)	-0.0118(3)	-0.0118(2)
R(33)	34	-0.0175(6)	-0.0167(6)	-0.0167(4)	-0.0151(2)	-0.0132(2)	-0.0133(2)	-0.0125(2)

Table 4.8: N_2-shift coefficients ($cm^{-1}atm^{-1}$) calculated with the semi-classical approach. [84].

lines	*J*	213 K	233 K	253 K	273 K	296 K	313 K	333 K
R(0)	0	-0.0094	-0.0089	-0.0084	-0.0080	-0.0066	-0.0073	-0.0069
R(1)	1	-0.0093	-0.0088	-0.0084	-0.0079	-0.0068	-0.0072	-0.0068
R(2)	2	-0.0093	-0.0088	-0.0084	-0.0080	-0.0067	-0.0072	-0.0069
R(3)	3	-0.0088	-0.0083	-0.0079	-0.0077	-0.0070	-0.0071	-0.0068
R(4)	4	-0.0082	-0.0080	-0.0076	-0.0073	-0.0078	-0.0066	-0.0064
R(5)	5	-0.0090	-0.0083	-0.0077	-0.0073	-0.0083	-0.0067	-0.0064
R(6)	6	-0.0099	-0.0090	-0.0084	-0.0080	-0.0085	-0.0071	-0.0067
R(7)	7	-0.0105	-0.0099	-0.0092	-0.0085	-0.0089	-0.0074	-0.0071
R(8)	8	-0.0111	-0.0103	-0.0097	-0.0091	-0.0088	-0.0080	-0.0075
R(9)	9	-0.0116	-0.0105	-0.0098	-0.0093	-0.0090	-0.0082	-0.0078
R(10)	10	-0.0120	-0.0111	-0.0102	-0.0094	-0.0091	-0.0083	-0.0080
R(11)	11	-0.0118	-0.0111	-0.0104	-0.0097	-0.0089	-0.0085	-0.0080
R(12)	12	-0.0118	-0.0109	-0.0103	-0.0098	-0.0090	-0.0087	-0.0082
R(13)	13	-0.0120	-0.0111	-0.0103	-0.0097	-0.0090	-0.0086	-0.0082
R(14)	14	-0.0122	-0.0113	-0.0105	-0.0098	-0.0091	-0.0087	-0.0082
R(15)	15	-0.0126	-0.0115	-0.0107	-0.0099	-0.0092	-0.0088	-0.0083
R(16)	16	-0.0129	-0.0118	-0.0109	-0.0101	-0.0094	-0.0089	-0.0084
R(17)	17	-0.0134	-0.0122	-0.0112	-0.0104	-0.0096	-0.0091	-0.0085
R(18)	18	-0.0139	-0.0126	-0.0115	-0.0106	-0.0098	-0.0092	-0.0087
R(19)	19	-0.0144	-0.0130	-0.0119	-0.0109	-0.0100	-0.0095	-0.0089
R(20)	20	-0.0149	-0.0135	-0.0122	-0.0112	-0.0103	-0.0097	-0.0091
R(21)	21	-0.0155	-0.0139	-0.0126	-0.0116	-0.0106	-0.0099	-0.0093
R(22)	22	-0.0161	-0.0144	-0.0130	-0.0119	-0.0109	-0.0102	-0.0095
R(23)	23	-0.0166	-0.0149	-0.0135	-0.0123	-0.0112	-0.0105	-0.0098
R(24)	24	-0.0172	-0.0154	-0.0139	-0.0127	-0.0115	-0.0108	-0.0100
R(25)	25	-0.0178	-0.0159	-0.0143	-0.0130	-0.0118	-0.0110	-0.0103
R(26)	26	-0.0183	-0.0163	-0.0147	-0.0134	-0.0121	-0.0113	-0.0105
R(27)	27	-0.0188	-0.0168	-0.0151	-0.0138	-0.0124	-0.0116	-0.0108
R(28)	28	-0.0193	-0.0173	-0.0155	-0.0141	-0.0128	-0.0119	-0.0110
R(29)	29	-0.0198	-0.0177	-0.0159	-0.0145	-0.0131	-0.0122	-0.0113
R(30)	30	-0.0203	-0.0181	-0.0163	-0.0148	-0.0134	-0.0125	-0.0116
R(31)	31	-0.0208	-0.0185	-0.0167	-0.0152	-0.0137	-0.0128	-0.0118
R(32)	32	-0.0212	-0.0189	-0.0171	-0.0155	-0.0140	-0.0130	-0.0121
R(33)	33	-0.0217	-0.0193	-0.0174	-0.0158	-0.0143	-0.0133	-0.0123

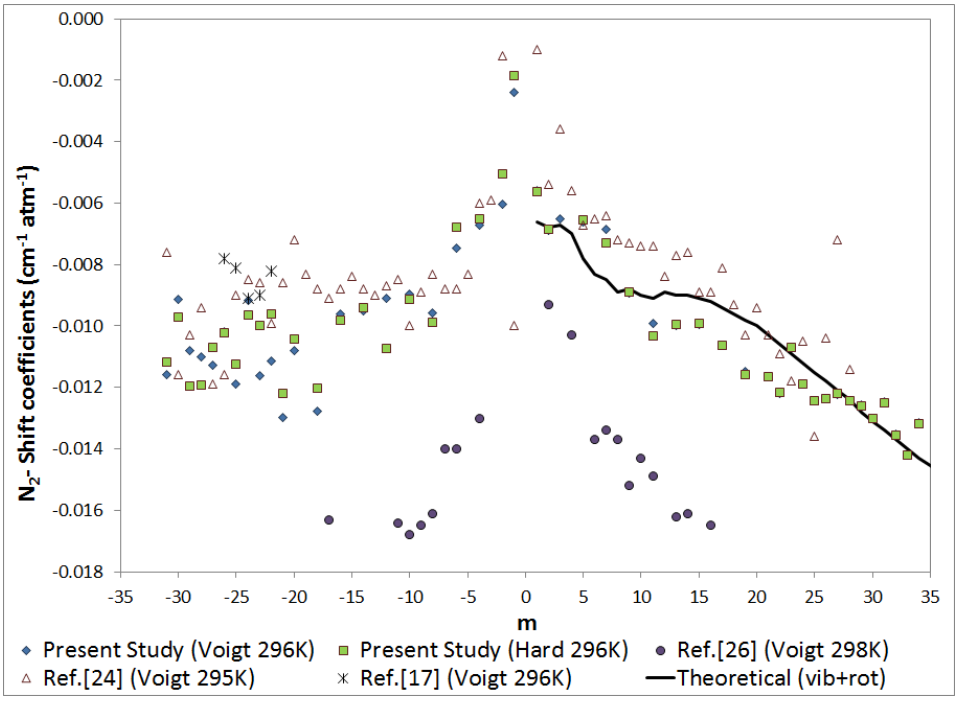

Figure 4.5: Overlaid experimental, theoretical and published room temperature N_2-shift coefficients of C_2H_2 transitions [84].

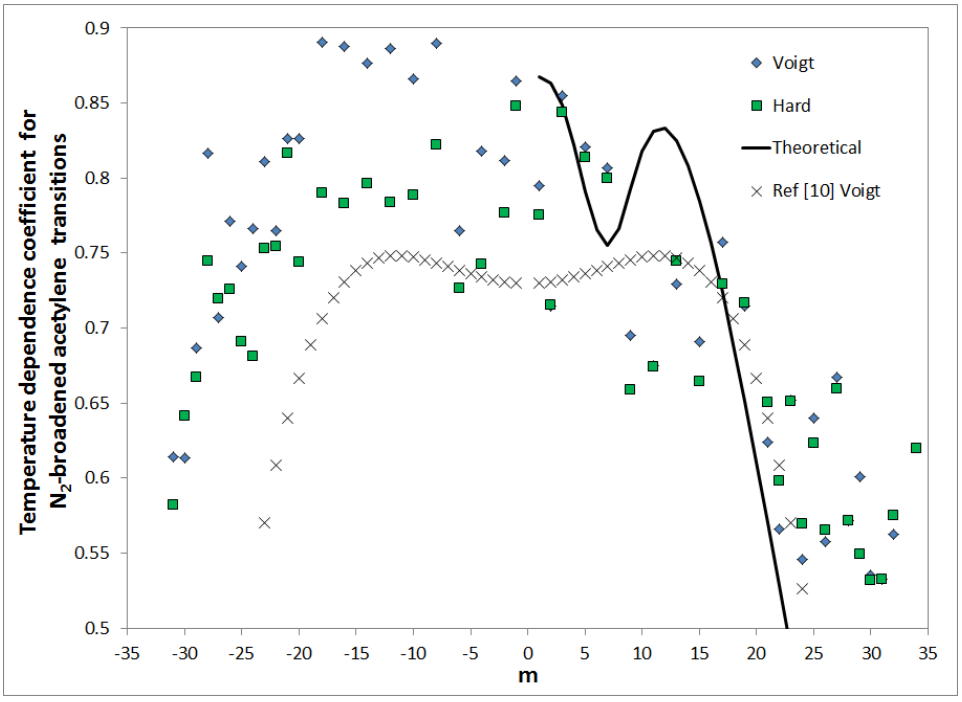

Figure 4.6: Theoretical and experimental temperature dependence exponents, n, for the N_2-broadening coefficients of C_2H_2 transitions obtained from equation (4.1) [84].

Table 4.9: N_2-broadening coefficients $\gamma^0_{N2}(cm^{-1}atm^{-1})$ at 296 K and their temperature dependence exponents *n*. The experimental results are derived from measurements assuming the Voigt and hard-collision lineshapes (values quoted in parentheses correspond to one standard deviation) [84].

Line	*m*	$\gamma^o_{N2\ Voigt}(296)$	$\gamma^o_{N2\ hard}(296)$	$\gamma^o_{N2\ calc}(296)$	n_{Voigt}	n_{hard}	n_{calc}
P(31)	-31	0.0448(3)	0.0416(4)	-	0.6140(3)	0.5820(3)	-
P(30)	-30	0.0507(5)	0.0441(4)	-	0.6133(3)	0.6412(3)	-
P(29)	-29	0.0549(2)	0.0513(5)	-	0.6870(3)	0.6673(3)	-
P(28)	-28	0.0521(3)	0.0541(5)	-	0.8166(4)	0.7446(4)	-
P(27)	-27	0.0606(3)	0.0608(6)	-	0.7070(4)	0.7195(4)	-
P(26)	-26	0.0546(21)	0.0580(6)	-	0.7714(4)	0.7261(4)	-
P(25)	-25	0.0586(3)	0.0613(6)	-	0.7415(4)	0.6910(3)	-
P(24)	-24	0.0523(0)	0.0611(6)	-	0.7662(4)	0.6815(3)	-
P(23)	-23	0.0584(5)	0.0627(6)	-	0.8113(4)	0.7530(4)	-
P(22)	-22	0.0526(2)	0.0632(6)	-	0.7652(4)	0.7546(4)	-
P(21)	-21	0.0538(2)	0.0640(6)	-	0.8265(4)	0.8165(4)	-
P(20)	-20	0.0547(8)	0.0687(7)	-	0.8263(4)	0.7442(4)	-
P(18)	-18	0.0571(7)	0.0715(7)	-	0.8904(4)	0.7902(4)	-
P(16)	-16	0.0595(4)	0.0730(7)	-	0.8878(4)	0.7834(4)	-
P(14)	-14	0.0652(7)	0.0749(7)	-	0.8769(4)	0.7964(4)	-
P(12)	-12	0.0689(2)	0.0783(8)	-	0.8860(4)	0.7837(4)	-
P(10)	-10	0.0730(0)	0.0836(8)	-	0.8663(4)	0.7884(4)	-
P(8)	-8	0.0802(0)	0.0893(9)	-	0.8900(4)	0.8220(4)	-
P(6)	-6	0.0921(0)	0.0964(10)	-	0.7646(4)	0.7262(4)	-
P(4)	-4	0.0960(21)	0.0990(10)	-	0.8179(4)	0.7427(4)	-
P(2)	-2	0.1022(4)	0.1071(11)	-	0.8116(4)	0.7765(4)	-
P(1)	-1	0.1057(19)	0.1080(11)	-	0.8648(4)	0.8476(4)	-
R(0)	1	0.1081(7)	0.1100(11)	0.0973	0.7947(4)	0.7755(4)	0.8673
R(1)	2	0.1053(13)	0.1050(10)	0.0967	0.7145(4)	0.7155(4)	0.8631
R(2)	3	0.0957(9)	0.0958(10)	0.0965	0.8547(4)	0.8438(4)	0.8487
R(4)	5	0.0928(6)	0.0925(9)	0.0939	0.8204(4)	0.8137(4)	0.7905
R(6)	7	0.0902(7)	0.0893(9)	0.0880	0.8070(4)	0.7997(4)	0.7553
R(8)	9	0.0885(3)	0.0882(9)	0.0832	0.6955(3)	0.6590(3)	0.7925
R(10)	11	0.0830(2)	0.0820(8)	0.0815	0.6751(3)	0.6745(3)	0.8315
R(12)	13	0.0817(8)	0.0809(8)	0.0810	0.7290(4)	0.7447(4)	0.8248
R(14)	15	0.0822(4)	0.0821(8)	0.0800	0.6909(3)	0.6645(3)	0.7847
R(16)	17	0.0810(3)	0.0809(8)	0.0782	0.7575(4)	0.7294(4)	0.7238
R(18)	19	0.0723(5)	0.0723(7)	0.0756	0.7150(4)	0.7166(4)	0.6511
R(20)	21	0.0730(3)	0.0737(7)	0.0722	0.6240(3)	0.6503(3)	0.5703
R(21)	22	0.0766(4)	0.0762(8)	0.0703	0.5662(3)	0.5984(3)	0.5282
R(22)	23	0.0638(3)	0.0642(6)	0.0683	0.6521(3)	0.6512(3)	-
R(23)	24	0.0678(3)	0.0676(7)	0.0663	0.5457(3)	0.5698(3)	-
R(24)	25	0.0608(3)	0.0623(6)	0.0642	0.6400(3)	0.6234(3)	-
R(25)	26	0.0626(1)	0.0628(6)	0.0621	0.5578(3)	0.5653(3)	-
R(26)	27	0.0586(2)	0.0592(6)	0.0600	0.6672(3)	0.6593(3)	-
R(27)	28	0.0556(4)	0.0561(6)	0.0580	0.5713(3)	0.5713(3)	-
R(28)	29	0.0545(2)	0.0553(6)	0.0559	0.6008(3)	0.5490(3)	-
R(29)	30	0.0534(1)	0.0540(5)	0.0539	0.5354(3)	0.5316(3)	-
R(30)	31	0.0531(5)	0.0540(5)	0.0519	0.5323(3)	0.5323(3)	-
R(31)	32	0.0505(2)	0.0514(5)	0.0500	0.5622(3)	0.5748(3)	-
R(32)	33	0.0550(7)	0.0557(6)	0.0482			-
R(33)	34	0.0472(3)	0.0482(5)	0.0464	0.6035(3)	0.6197(3)	-

Table 4.10: N_2-shift coefficients δ^0_{N2} ($cm^{-1}atm^{-1}$) at 296 K and their temperature dependence coefficients δ' according to equation (4.3). The experimental results are derived from measurements assuming the Voigt and hard-collision lineshapes (values quoted in parentheses correspond to one standard deviation). The theoretical values are calculated for the *R* branch only (except very low *m*-values, shifts in the *P* and *R* branches are symmetric) [84].

Line	***m***	$\delta^o_{N2\ Voigt}(296)$	$\delta^o_{N2\ hard}(296)$	$\delta^o_{calc}(296)$	$\delta'_{Voigt}\times10^5$	$\delta'_{hard}\times10^5$	$\delta'_{calc}\times10^5$
P(31)	-31	-0.0122(5)	-0.0120(5)	-	1.3(1)	0.8(1)	-
P(30)	-30	-0.0110(5)	-0.0112(5)	-	0.8(1)	0.9(1)	-
P(29)	-29	-0.0122(5)	-0.0124(6)	-	1.3(1)	0.9(1)	-
P(28)	-28	-0.0111(5)	-0.0119(5)	-	0.9(1)	0.1(0)	-
P(27)	-27	-0.0116(5)	-0.0114(5)	-	1.1(1)	1.0(1)	-
P(26)	-26	-0.0113(5)	-0.0117(5)	-	1.1(1)	1.0(1)	-
P(25)	-25	-0.0114(5)	-0.0113(5)	-	1.1(1)	1.1(1)	-
P(24)	-24	-0.0109(5)	-0.0108(5)	-	1.3(1)	1.5(2)	-
P(23)	-23	-0.0113(5)	-0.0107(5)	-	1.4(1)	1.3(1)	-
P(22)	-22	-0.0116(5)	-0.0107(5)	-	1.1(1)	1.6(2)	-
P(21)	-21	-0.0114(5)	-0.0110(5)	-	1.0(1)	1.7(2)	-
P(20)	-20	-0.0105(5)	-0.0107(5)	-	1.2(1)	0.8(1)	-
P(18)	-18	-0.0127(6)	-0.0121(5)	-	1.3(1)	-0.7(0)	-
P(16)	-16	-0.0103(5)	-0.0102(5)	-	1.4(1)	1.8(2)	-
P(14)	-14	-0.0099(4)	-0.0098(4)	-	1.3(1)	1.4(1)	-
P(12)	-12	-0.0098(4)	-0.0101(5)	-	2.1(2)	1.6(2)	-
P(10)	-10	-0.0095(4)	-0.0094(4)	-	1.5(2)	1.7(2)	-
P(8)	-8	-0.0100(4)	-0.0090(4)	-	1.5(2)	2.3(2)	-
P(6)	-6	-0.0074(3)	-0.0084(4)	-	1.3(1)	1.1(1)	-
P(4)	-4	-0.0070(3)	-0.0071(3)	-	1.7(2)	1.4(1)	-
P(2)	-2	-0.0064(3)	-0.0063(3)	-	1.7(2)	1.6(2)	-
P(1)	-1	-0.0059(3)	-0.0058(3)	-	1.7(2)	1.5(2)	-
R(0)	1	-0.0039(2)	-0.0039(2)	-0.0071(3)	0.4(0)	0.4(0)	1.7(2)
R(1)	2	-0.0058(3)	-0.0058(3)	-0.0072(3)	0.2(0)	0.1(0)	1.8(2)
R(2)	3	-0.0062(3)		-0.0072(3)	0.6(1)	0.6(1)	1.8(2)
R(4)	5	-0.0063(3)	-0.0063(3)	-0.0074(3)	0.9(1)	0.9(1)	2.3(2)
R(6)	7	-0.0064(3)	-0.0065(3)	-0.0081(4)	0.7(1)	0.7(1)	2.9(3)
R(8)	9	-0.0075(3)	-0.0075(3)	-0.0087(4)	0.7(1)	0.7(1)	3.0(3)
R(10)	11	-0.0080(4)	-0.0086(4)	-0.009(4)	0.9(1)	0.9(1)	3.0(3)
R(12)	13	-0.0092(4)	-0.0092(4)	-0.0091(4)	1.9(2)	1.9(2)	3.0(3)
R(14)	15	-0.0098(4)	-0.0098(4)	-0.0092(4)	2.7(3)	2.3(2)	3.3(3)
R(16)	17	-0.0106(5)	-0.0106(5)	-0.0095(4)	3.7(4)	3.7(4)	3.7(4)
R(18)	19	-0.0111(5)	-0.0111(5)	-0.0099(4)	4.1(4)	4.0(4)	4.2(4)
R(20)	21	-0.0111(5)	-0.0111(5)	-0.0105(5)	4.4(4)	4.4(4)	4.8(5)
R(21)	22	-0.0119(5)	-0.0118(5)	-0.0108(5)	3.9(4)	3.9(4)	5.1(5)
R(22)	23	-0.0121(5)	-0.0120(5)	-0.0111(5)	4.4(4)	4.5(5)	5.4(5)
R(23)	24	-0.0124(6)	-0.0124(6)	-0.0114(5)	4.2(4)	4.2(4)	5.7(6)
R(24)	25	-0.0123(6)	-0.0123(6)	-0.0117(5)	4.5(5)	4.5(5)	5.9(6)
R(25)	26	-0.0124(6)	-0.0123(6)	-0.012(5)	5.2(5)	5.4(5)	6.2(6)
R(26)	27	-0.0126(6)	-0.0129(6)	-0.0124(6)	4.7(5)	5.3(5)	6.4(6)
R(27)	28	-0.0132(6)	-0.0132(6)	-0.0127(6)	4.8(5)	4.8(5)	6.6(7)
R(28)	29	-0.0130(6)	-0.0132(6)	-0.013(6)	4.6(5)	5.4(5)	6.8(7)
R(29)	30	-0.0139(6)	-0.0139(6)	-0.0133(6)	4.2(4)	4.3(4)	7.0(7)
R(30)	31	-0.0133(6)	-0.0133(6)	-0.0137(6)	4.8(5)	4.9(5)	7.2(7)
R(31)	32	-0.0138(6)	-0.0138(6)	-0.014(6)	4.4(4)	4.4(4)	7.4(7)
R(32)	33	-0.0133(6)	-0.0133(6)	-0.0143(6)	4.6(5)	3.1(3)	7.5(8)
R(33)	34	-0.0140(6)	-0.0140(6)	-0.0146(7)	4.5(5)	4.5(5)	7.7(8)

Table 4.11: N_2-shift coefficients δ^0_{N2} ($cm^{-1}atm^{-1}$) at 296 K and their temperature dependence parameters $\delta'_{1\,N2}$ and $\delta'_{2\,N2}$ according to equation (4.4). The experimental results are derived from measurements assuming the Voigt and hard-collision lineshapes (values quoted in parentheses correspond to one standard deviation). The theoretical values are calculated for the *R* branch only (except very low *m*-values, shifts in the *P* and *R* branches are symmetric) [84].

Lines	m	δ^0 N2 Voigt (296)	δ^0 N2 Hard (296)	δ^0 N2 Calc (296)	δ_1' N2 Voigt $\times10^5$	δ_1' N2 Hard $\times10^5$	δ_1' N2 Calc $\times10^5$	δ_2' N2 Voigt $\times10^7$	δ_2' N2 Hard $\times10^7$	δ_2' N2 Calc $\times10^7$
P31	-31	-0.0121(5)	-0.0118(5)	-	0.87(9)	0.37(4)	-	-0.94(1)	-1.47(1)	-
P30	-30	-0.0104(5)	-0.0107(5)	-	-3.66(37)	-3.14(31)	-	-1.93(2)	-15.37(15)	-
P29	-29	-0.0118(5)	-0.0122(6)	-	0.21(2)	0.21(2)	-	-1.36(1)	-1.44(1)	-
P28	-28	-0.0109(5)	-0.0119(5)	-	3.00(30)	-1.18(12)	-	-0.65(1)	-1.90(2)	-
P27	-27	-0.0115(5)	-0.0112(5)	-	0.37(4)	0.34(3)	-	-0.14(0)	-2.43(2)	-
P26	-26	-0.011(5)	-0.0117(5)	-	0.94(9)	0.31(3)	-	-1.12(1)	-1.07(1)	-
P25	-25	-0.0117(5)	-0.0114(5)	-	1.26(13)	1.14(11)	-	-0.03(0)	0.53(1)	-
P24	-24	-0.0108(5)	-0.0108(5)	-	0.85(8)	1.21(12)	-	-0.97(1)	-0.57(1)	-
P23	-23	-0.0113(5)	-0.0105(5)	-	1.15(12)	1.90(19)	-	0.55(1)	-4.31(4)	-
P22	-22	-0.0111(5)	-0.0105(5)	-	0.44(4)	0.99(10)	-	0.65(1)	-1.14(1)	-
P21	-21	-0.0114(5)	-0.011(5)	-	-0.42(4)	1.64(16)	-	0.63(1)	-0.06(0)	-
P20	-20	-0.0105(5)	-0.0107(5)	-	1.15(12)	0.82(8)	-	0.30(0)	0.040(0)	-
P18	-18	-0.0128(6)	-0.0121(5)	-	4.31(43)	-0.95(9)	-	0.37(0)	-0.49(0)	-
P16	-16	-0.0106(5)	-0.01(5)	-	2.63(26)	1.50(15)	-	2.75(3)	-0.98(1)	-
P14	-14	-0.0101(5)	-0.0101(5)	-	5.49(55)	5.33(53)	-	1.88(2)	8.61(9)	-
P12	-12	-0.0098(4)	-0.0101(5)	-	3.60(36)	3.31(33)	-	1.45(1)	2.55(3)	-
P10	-10	-0.0092(4)	-0.0095(4)	-	4.84(48)	3.43(34)	-	0.82(1)	3.71(4)	-
P8	-8	-0.0096(4)	-0.009(4)	-	10.85(19)	3.53(35)	-	2.03(2)	1.82(2)	-
P6	-6	-0.0075(3)	-0.0951(43)	-	1.70(17)	5.95(60)	-	11.16(11)	10.53(11)	-
P4	-4	-0.007(3)	-0.0071(3)	-	3.07(31)	1.39(14)	-	-0.17(0)	-0.11(0)	-
P2	-2	-0.0064(3)	-0.0025(1)	-	1.68(17)	1.23(12)	-	-0.01(0)	-0.81(1)	-
P1	-1	-0.0056(3)	-0.0051(2)	-	0.38(4)	-1.1(11)	-	-2.90(3)	-5.04(5)	-
R0	1	-0.0035(2)	-0.0035(2)	-0.0071	-1.45(15)	-1.47(15)	1.54	-4.09(4)	-4.07(4)	-0.37
R1	2	-0.0057(3)	-0.0056(3)	-0.0072	-0.56(6)	-0.70(7)	1.57	-1.60(2)	-1.74(2)	-0.43
R2	3	-0.0062(3)		-0.0071	0.49(5)	0.49(5)	1.60	-0.28(0)	-0.28(0)	-0.50
R4	5	-0.0067(3)	-0.0066(3)	-0.0073	2.03(20)	1.89(19)	1.93	5.00(5)	3.66(4)	-0.77
R6	7	-0.0063(3)	-0.0065(3)	-0.0080	0.69(7)	0.73(7)	2.43	0.40(0)	0.27(0)	-0.97
R8	9	-0.0079(4)	-0.0079(4)	-0.0086	2.34(23)	2.28(23)	2.62	3.48(3)	3.49(3)	-0.90
R10	11	-0.0082(4)	-0.0098(4)	-0.0089	1.82(18)	1.93(19)	2.56	3.02(3)	15.76(16)	-0.86
R12	13	-0.0093(4)	-0.0093(4)	-0.0090	2.40(24)	2.39(24)	2.58	1.04(1)	1.02(1)	-0.98
R14	15	-0.0098(4)	-0.0099(4)	-0.0091	2.53(25)	2.67(27)	2.74	0.37(0)	0.91(1)	-1.21
R16	17	-0.0106(5)	-0.0106(5)	-0.0094	3.60(36)	3.57(36)	3.03	-0.25(0)	-0.31(0)	-1.51
R18	19	-0.011(5)	-0.011(5)	-0.0097	3.50(35)	3.40(34)	3.41	-1.28(1)	-1.42(1)	-1.82

Table 4.11: Continued.

Lines	m	δ^0 N2 Voigt (296)	δ^0 N2 Hard (296)	δ^0 N2 Calc (296)	δ_1' N2 Voigt $\times 10^5$	δ_1' N2 Hard $\times 10^5$	δ_1' N2 Calc $\times 10^5$	δ_2' N2 Voigt $\times 10^7$	δ_2' N2 Hard $\times 10^7$	δ_2' N2 Calc $\times 10^7$
R20	21	-0.011(5)	-0.011(5)	-0.0102	3.93(39)	3.84(38)	3.83	-1.07(1)	-1.25(1)	-2.13
R21	22	-0.0182(8)	-0.0118(5)	-0.0105	3.80(38)	3.77(38)	4.05	-0.31(0)	-0.36(0)	-2.27
R22	23	-0.0118(5)	-0.0117(5)	-0.0108	3.08(31)	3.09(31)	4.27	-2.87(3)	-3.05(3)	-2.41
R23	24	-0.0122(5)	-0.0122(5)	-0.0111	3.33(33)	3.33(33)	4.49	-1.97(2)	-1.99(2)	-2.53
R24	25	-0.0124(6)	-0.0124(6)	-0.0114	4.74(47)	4.72(47)	4.70	0.43(0)	0.40(0)	-2.64
R25	26	-0.0124(6)	-0.0123(6)	-0.0117	5.43(54)	5.39(54)	4.90	0.18(0)	0.07(0)	-2.74
R26	27	-0.0129(6)	-0.0127(6)	-0.0121	4.55(45)	4.46(45)	5.09	-1.63(2)	-1.78(2)	-2.84
R27	28	-0.013(6)	-0.013(6)	-0.0124	4.06(41)	4.07(41)	5.28	1.54(2)	-1.57(2)	-2.91
R28	29	-0.0129(6)	-0.0132(6)	-0.0127	5.33(53)	5.36(54)	5.45	-0.09(0)	-0.02(0)	-2.99
R29	30	-0.0137(6)	-0.0137(6)	-0.0130	3.32(33)	3.35(33)	5.62	-1.97(2)	-1.99(2)	-3.04
R30	31	-0.0131(6)	-0.0131(6)	-0.0133	4.02(40)	4.05(41)	5.77	-1.79(2)	-1.75(2)	-3.11
R31	32	-0.0138(6)	-0.0137(6)	-0.0136	4.30(43)	4.18(42)	5.92	-0.25(0)	-0.48(0)	-3.15
R32	33	-0.0132(6)	-0.0132(6)	-0.0139	4.27(43)	4.49(45)	6.06	4.61(5)	-1.36(1)	-3.22
R33	34	-0.014(6)	-0.014(6)	-0.0142	4.55(45)	4.59(46)	6.19	0.15(0)	0.10(0)	-3.26

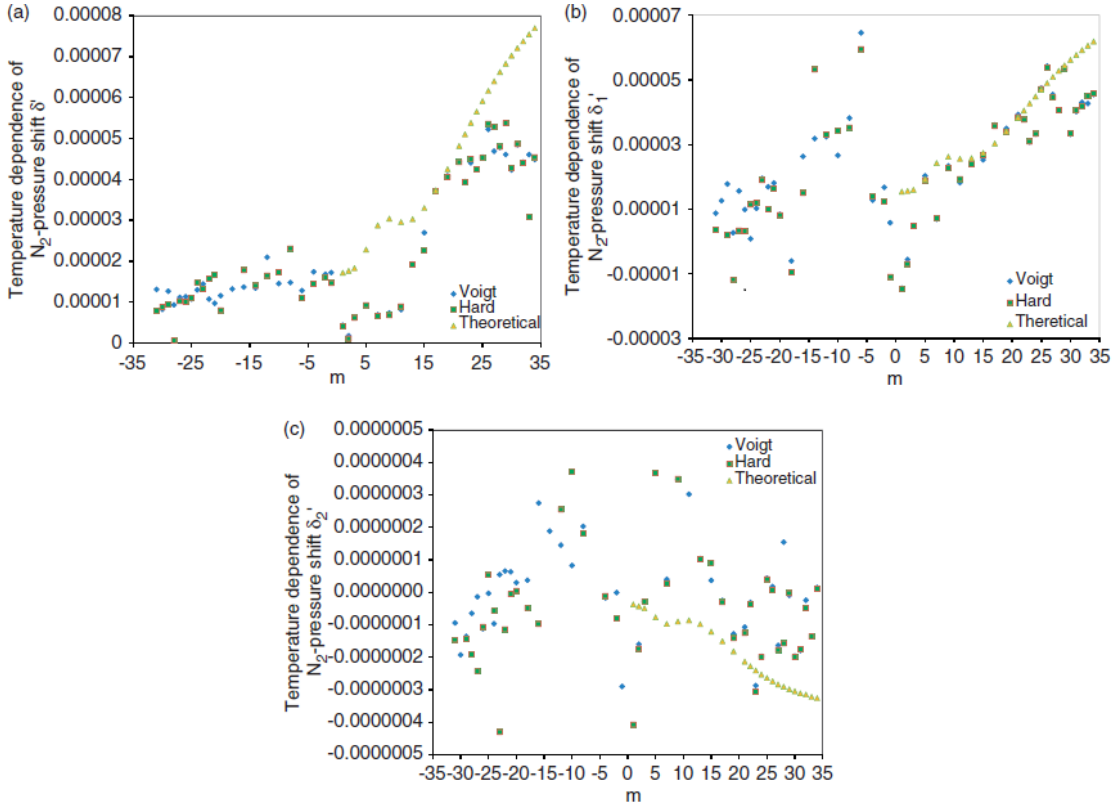

Figure 4.7: Temperature-dependent terms of N_2-shift of C_2H_2 transitions: (a) δ'obtained from equation (4.3), (b) δ_1' and (c) δ_2' obtained from equation (4.4) [84].

To conclude, in this chapter we presented a study of total 47 lines (22 in the *P*- and 25 in the *R*-branch) of C_2H_2 broadened by N_2. This study was carried out also to examine the temperature dependencies of different parameters, and that is why spectra was recoded for over a range of temperatures between 213 and 333 K. N_2-broadening and shift coefficients have been deduced with the Voigt and hard-collision profile models. We have determined the temperature exponents, *n*, for the broadening coefficients as well as the temperature-dependence characteristics for the pressure-shift coefficients. The experimental results have been supported by a Robert–Bonamy type semi-classical calculations of Robert-Bonamy type with exact trajectories. A good agreement has been stated between our experimentally retrieved and theoretically calculated results.

5 Intensity analysis of hot HCN transitions

5.1 Symath

The software employed to carry out the intensity analysis is called Symath [95], developed in Mathematica using as a platform. This spectroscopic analysis software was designed and developed by Georg Mellau [95]. Symath allows the user to "*write*" programs by defining mathematical equations/algorithms that describe the problem under analysis. Using the lineshape analysis feature of the Spectrum Fit module, the user can accurately identify the peak positions for the transitions of interest as well as for the overlapping transitions. The main components of this spectroscopic analysis package are identified as: Molecule, Band Search, and Spectrum fit [80].

The Molecule program has all the information about the molecular structure and symmetry as input. It adds an analytical matrix mechanics module, stores information on the vibrational and rotational states lists, the transition types and the constants [80]. Using the Molecular program, is possible to predict and analyze the molecular transitions and states of any quantum system defining by the analytical formulas of matrix elements. The program is coded for generating the energy levels (Eigen energies) and calculating molecular transition (possible line positions) by inserting the information on molecular symmetry and a molecular Hamiltonian.

The Band Search Program is linked with the Molecular program and use the lineshape parameters such as spectral line position, intensity and line width that are saved in the Spectrum Fit database for each and every peak. This program is modeled to analyses

the spectra in a "*band to band*" and "*peak to peak*" sequence. Band Search Window shows the list of the line position, intensity and width of a selected transition. During the assignment of bands, the user can change the line positions and intensities of the "peaklist", and add or delete lines of the spectrum though a deconvolution procedure. This step can only be performed if the user gains the knowledge and skills of deconvolution during the fit of the band peaks. It is necessary to distinguish all the peaks that are already assigned by marking them with labels, so that it helps to assign the lines of very weak bands and the overlapping transitions present in the dense spectra of HCN [80].

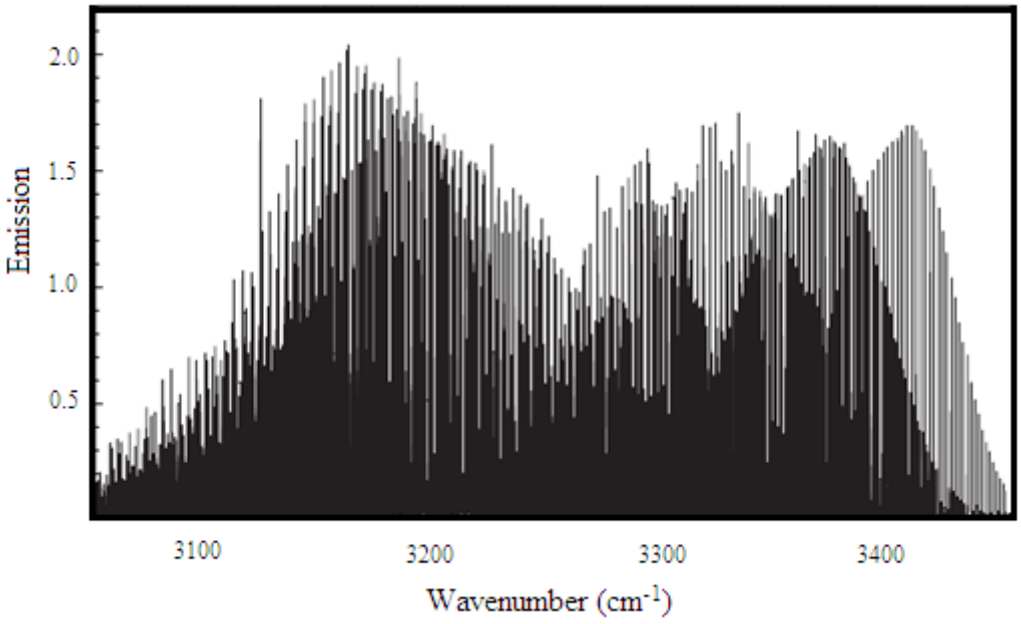

Figure 5.1: The emission spectrum of HCN in the 3000 to 3500 cm-^{1} range.

Figure 5.1 represents highly dense emission spectra of HCN recorded in the 3000 – 3500 cm^{-1} spectral range. The figure shows presence of several strong and weak bands. Spectroscopic parameters of the emission lines were determined using a typical peaklist found after the assignment process.

5.2 Line Intensities of the $1v^{l}_{2}0 \leftarrow 0v^{l}_{2}0$ Band System from the HCN Emission Spectrum

The hot bands occurred in the $1\nu_2^l 0 \leftarrow 0\nu_2^l 0$ transition of HCN molecule for ν_2= 4 and ν_2= 5 are listed in Table 5.1. Due to self-absorption effects, bands below ν_2 = 4 were not considered in this analysis.

Table 5.1: Rovibrational transitions from the emission spectrum

Transition $\nu_1'\nu'_2{}^{l'}\nu_3' \rightarrow \nu_1''\nu''_2{}^{l''}\nu_3''$	Wavenumber range (cm^{-1})
$14^00 \rightarrow 04^00$	2941.96−3399.90
$14^20 \rightarrow 04^20$	2940.91−3402.80
$14^40 \rightarrow 04^40$	2940.44-3406.59
$15^10 \rightarrow 05^10$	**2922.56−3382.36**
$15^30 \rightarrow 05^30$	2921.59−3385.34
$15^50 \rightarrow 05^50$	**2921.31−3389.19**

The spectra in Figure 5.1 is very dense because it contains bands other than the $1\nu_2^l 0 \leftarrow 0\nu_2^l 0$band in the same region. They are $1\nu_2^l 1 \leftarrow 0\nu_2^l 1$ (2971.41 to 3459.60 cm^{-1}), $2\nu_2^l 0 \leftarrow 1\nu_2^l 0$ (2856.88 to 3292.37 cm^{-1}) and $3\nu_2^l 0 \leftarrow 2\nu_2^l 0$ (2824.36 to 3188.18 cm^{-1}) bands, occur with smaller intensity compared to the $1\nu_2^l 0 \leftarrow 0\nu_2^l 0$ band. The line intensities of the above mentions bands are needed to be analyzed prior to the analysis of our band ($1\nu_2^l 0 \leftarrow 0\nu_2^l 0$) because of overlaying that occurs in this band system. This work has already been accomplished [55] using Symath for the lines that are not overlapped.

The intensity of each line was first predicted using equation (2.58) and setting the Hermann-Wallis factor to 0. Simulation of line positions were completed for both weak and strongest peaks using a Doppler line shape and a pseudo Voigt shape respectively. The agreement between the experimental and the modeled spectra was improved through an iteration process after a step of manual checking. All the overlapped peaks were omitted

because of superimposition with other peaks. The predicted intensities of the lines were fitted to the formula (2.58) and the first estimation for their parameters R^2, A_1 and A_2 were found by intensity analysis program [55].

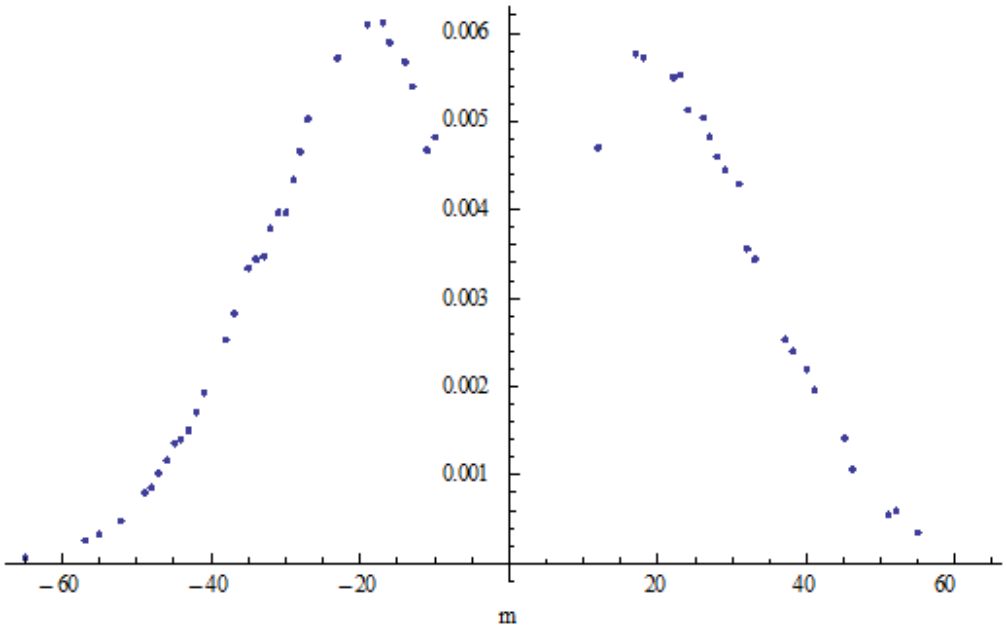

Figure 5.2: The line intensities for the HCN $15^10 \rightarrow 05^10$ band.

In order to calculate the band intensity, we have fitted the line intensity data to the equation (2.58). These line intensities were determined by the SyMath program. In this work I have used an algorithm to find A_1 and A_2 for the calculation of R^2. The line intensity of an emission spectrum has to be calibrated using absorption and *ab initio* line intensities. A linear calibration function

$$2.34(38) * 10^{-18} + 8.5(12) * 10^{-22} * \tilde{\nu} \qquad (5.1)$$

was found [55] and used, where $\tilde{\nu}$ is the wavenumber of the transition. The line intensities extracted from the emission spectrum have been corrected with this calibration factor.

For the analysis of band intensities in the $15^{l}0 \rightarrow 05^{l}0$ band system the temperature was fixed at 1446K with the Boltzmann constant used 0.695038759 cm^{-1}/K. S_R was found from the Honl-London-factor, S_v from equation (2.66) and the transition dipole moment squared μ_v^2 is 1.

Table 5.2: Results of the fits of the HCN $1v^{l}_{2}0 \rightarrow 0v^{l}_{2}0$ band.

Data Source	Transition $v_1' v'^{\,l'}_{2} v_3' \rightarrow v_1'' v''^{\,l''}_{2} v_3''$	T (K)	R^2 (Debye^2)	$A_1 * 10^4$	$A_2 * 10^6$
experimental	$14^{0}0e \rightarrow 04^{0}0e$	1446	0.00573(4)	-16.8(9)	9(5)
experimental	$14^{2}0e \rightarrow 04^{0}0e$	1446	0.00589(2)	-16.7(8)	0
experimental	$14^{2}0f \rightarrow 04^{2}0f$	1446	0.00588(3)	-18.2(10)	0
experimental	$14^{4}0e \rightarrow 04^{4}0e$	1446	0.00523(4)	-17.2(9)	46(5)
experimental	$14^{4}0f \rightarrow 04^{4}0f$	1446	0.00519(4)	-15.1(10)	53(6)
experimental	**$15^{1}0e \rightarrow 05^{1}0e$**	**1446**	**0.005701(10)**	**-8.5(2)**	**-10(6)**
experimental	**$15^{1}0f \rightarrow 05^{1}0f$**	**1446**	**0.005698(8)**	**-0.7(1)**	**-15(4)**
experimental	$15^{3}0e \rightarrow 05^{3}0e$	1446	0.00556(4)	17.0(10)	17(6)
experimental	$15^{3}0f \rightarrow 05^{2}0f$	1446	0.00559(3)	-17.2(8)	16(5)
experimental	**$15^{5}0e \rightarrow 05^{5}0e$**	**1446**	**0.005657(6)**	**-12.4(1)**	**-13(3)**
experimental	**$15^{5}0f \rightarrow 05^{5}0f$**	**1446**	**0.005566(6)**	**-14.1(1)**	**-17(4)**
ab initio	$14^{0}0e \rightarrow 04^{0}0e$	1446	0.0060100(26)	-13.60(7)	-2.46(33)
ab initio	$14^{2}0e \rightarrow 04^{0}0e$	1446	0.0060133(10)	-16.05(3)	0
ab initio	$14^{2}0f \rightarrow 04^{2}0f$	1446	0.00600035(4)	-14.65(2)	0
ab initio	$14^{4}0e \rightarrow 04^{4}0e$	1446	0.0059481(12)	-15.29(3)	1.17(15)
ab initio	$14^{4}0f \rightarrow 04^{4}0f$	1446	0.0059495(8)	-15.22(2)	0.91(9)
ab initio	**$15^{1}0e \rightarrow 05^{1}0e$**	**1446**	**0.0057408(22)**	**-12.49(8)**	**0**
ab initio	**$15^{1}0f \rightarrow 05^{1}0f$**	**1446**	**0.0057333(21)**	**15.08(9)**	**0**
ab initio	$15^{3}0e \rightarrow 05^{3}0e$	1446	0.0057123(20)	14.90(5)	0.78(26)
ab initio	$15^{3}0f \rightarrow 05^{2}0f$	1446	0.0057109(24)	-15.72(5)	2.26(30)
ab initio	**$15^{5}0e \rightarrow 05^{5}0e$**	**1446**	**0.0056568(7)**	**-15.02(2)**	**0**
ab initio	**$15^{5}0f \rightarrow 05^{5}0f$**	**1446**	**0.0056567(6)**	**-15.03(3)**	**0**

The results of $1v_2^l0 \leftarrow 0v_2^l0$ band system of the final fits are shown in the table 5.2. My work was focused on the highlighted bold part for $v_2 = 5$ and $l = 1$ and 5. Rest of the transitions for $v_2 = 4$ and $l = 0, 2, 4$; $v_2 = 5$ and $l = 3$ are available from previous study [55].

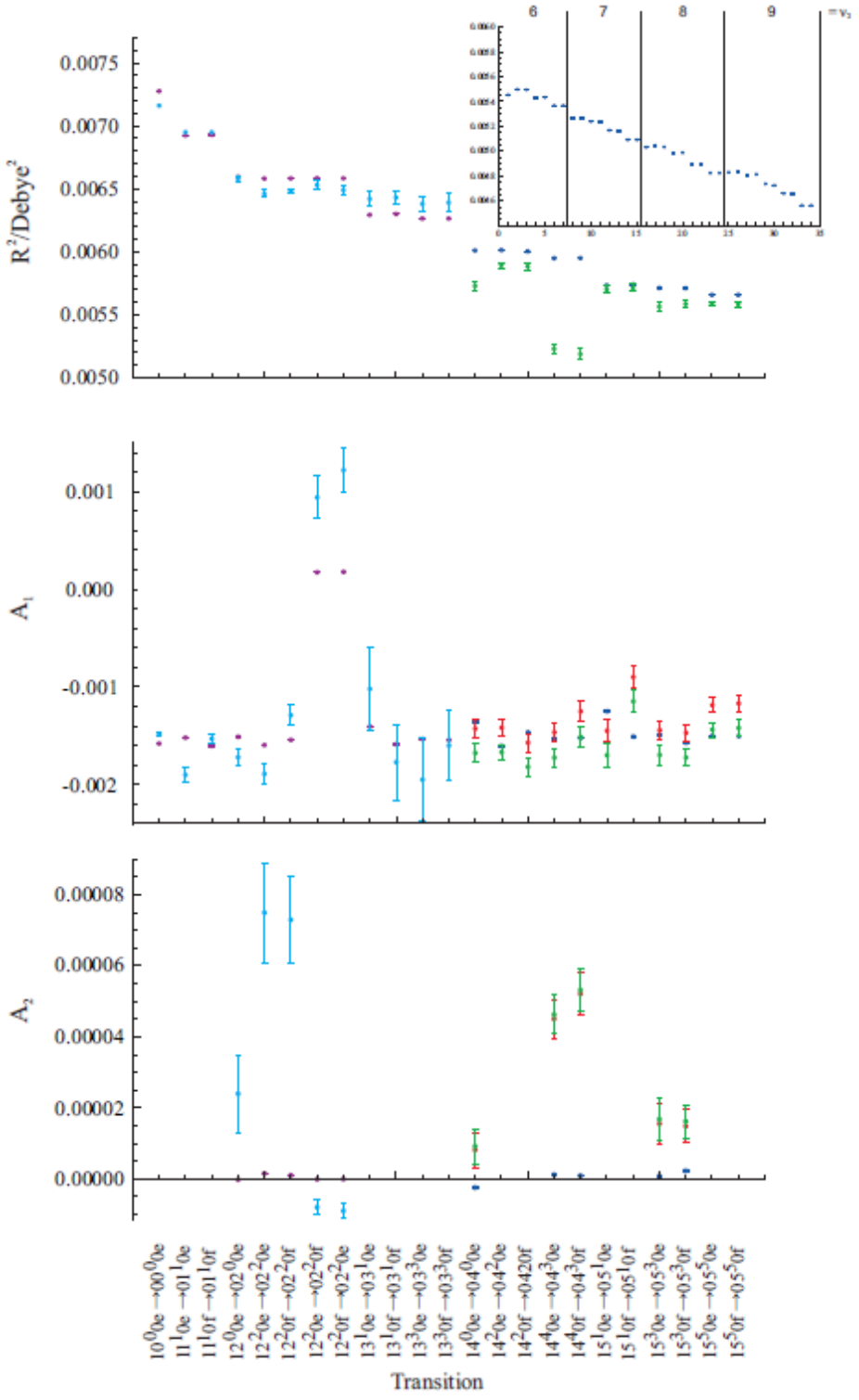

Figure 5.3: Results of the fit of the HCN emission spectrum before calibration (red) and after calibration (green) and *ab initio* data (blue and purple). Also shown are the results from HCN absorption spectrum (Cyan). [55].

The transition dipole moment squared found from the experimental results of the $15^l0 \rightarrow 05^l0$ band and from the line intensity fitting derived using the *ab initio* calculations, are in a good agreement to each other. The experimental results reported in the previous study for the $14^l0 \rightarrow 04^l0$ bands are too small due to self-absorption. The Hermann-Wallis factor shows a maximum of 20% difference while compared between the experimental and *ab initio* line intensities.

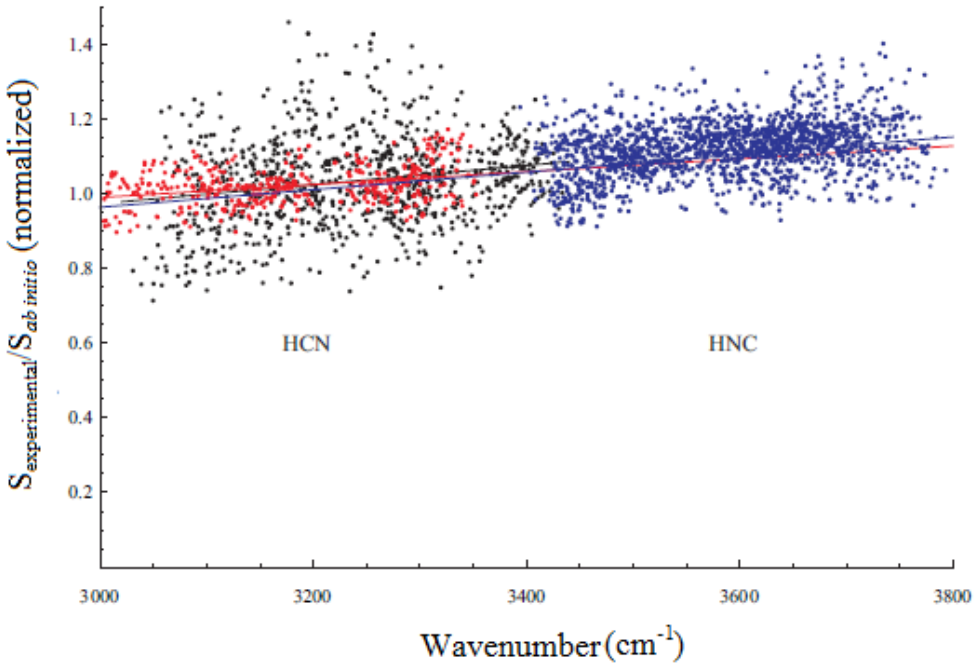

Figure 5.4: Calibration functions are in blue for the $1v^l_20 \rightarrow 0v^l_20$ band of HNC; in black for the $1v^l_21 \rightarrow 0v^l_21$ band and in red for the $1v^l_20 \rightarrow 0v^l_20$ band of HCN. [55].

A calibration function was determined for the $1\nu_2^l0 \rightarrow 0\nu_2^l0$ band of HCN in order to carry out the intensity calibration of the other bands, such as $1\nu_2^l1 \rightarrow 0\nu_2^l1$, $2\nu_2^l0 \rightarrow 1\nu_2^l0$ and $3\nu_2^l0 \rightarrow 2\nu_2^l0$ bands of HCN. All the calibration functions plotted in the figure 5.4 show a very good agreement. The line intensities of these bands were divided by the calibration function of the $1\nu_2^l0 \rightarrow 0\nu_2^l0$ band, obtained in a previous study [55]. The resulting sensitivity functions of the $1\nu_2^l0 \rightarrow 0\nu_2^l0$ and $1\nu_2^l1 \rightarrow 0\nu_2^l1$band for HCN with

the scaling factor 4.942×10^{-18} and $1\nu_2^l0 \rightarrow 0\nu_2^l0$ band for HNC with the scaling factor 4.346×10^{-20} are plotted in Figure 5.4. Sensitivity functions are derived for the sensitivity of the apparatus. For the $1\nu_2^l1 \rightarrow 0\nu_2^l1$, $2\nu_2^l0 \rightarrow 1\nu_2^l0$ and $3\nu_2^l0 \rightarrow 2\nu_2^l0$ bands the second parameter A_2 of the Hermann-Wallis factor has not been fitted due to overlapping.

6 Conclusion

The main purpose of this work was focused on obtaining spectroscopic information on linear polyatomic gas molecules, particularly acetylene (C-H≡H-C) and hydrogen cyanide (HCN). Two types of laser spectrometer have been employed for obtaining high quality spectroscopic data: a diode laser spectrometer (for acetylene) and a Fourier Transform spectrometer (for hydrogen cyanide). For acetylene study, we have examined N_2-broadened acetylene absorption spectra in order to retrieved the line parameters. N_2-broadened widths and pressure-induced N_2-shifts have been retrieved for a wide range of temperatures with the intention to analyse the temperature dependencies of N_2 broadening and shifting coefficients. Spectra were recorded in our laboratory at the Department of Physics and Astronomy, University of Lethbridge, Alberta, Canada. For hydrogen cyanide study, the emission spectra of HCN have previously been recorded at high temperature and low pressure using the Fourier transform spectrometer at the Justus Liebig University, Giessen, Germany. In this study, we have investigated emission line intensities. We did not consider any pressure-induced line shift effects for HCN as the spectra were recorded at very low pressure.

Absorption and emission spectra were recorded using a 3-channel tunable diode laser spectrometer and Fourier Transform laser spectrometer, respectively, as given below:

(i) The absorption experiments have been carried out using a high resolution 3-channel (e.g. sample cell, reference cell and background) tuneable diode laser spectrometer tuned for the infrared region of 1500-1570 nm. This setup is designed to control the temperature and pressure of the sample gas cell.

Therefore, the acetylene gas inside that cell was heated up to 333 K and cooled down to 213 K. As spectra were recorded at various temperatures we were able to determine temperature dependencies of N_2-broadening and N_2-shift coefficients. The cell pressures were selected to be 100, 250, 400 and 500 Torr.

(ii) A High Resolution Fourier Transform Infrared spectrometer was used to record HCN spectra. A quartz made gas cell was mounted inside an oven to be heated up to several hundred Kelvin to record high temperature spectra. Emission spectra of 1400 K temperature were investigated to gather information on band intensity calculated from individual line intensities.

We have compared our results with theoretically obtained results since it is very important to understand the theoretical aspects behind any experimental study. The relation between electromagnetic radiation and its interaction with matter, molecular structures, their normal modes of vibration, transitions between a pair of energy levels, structure, characteristics and the mechanism of band transitions of both acetylene and hydrogen cyanide molecules are described in this thesis in the Theory chapter (Chapter 2).

In the first spectroscopic study, we have analyzed the $\nu_1+\nu_3$ band of acetylene spectra broadened by nitrogen because this is a very strong combination band observable in the infrared region. Before carrying out the experiment, a simulation technique enabled us to select unsaturated transitions (spectral line positions in order to complete the spectral line shape analysis and retrieve the parameters, e.g. N_2- broadening, shifting coefficients and their dependencies on temperature). Our results are presented in chapter 4 where it is shown that they are in good agreement with the theoretical results obtained using a semi-

classical theoretical calculation procedure (calculation details are also discussed in chapter 4).

Each spectrum shows a unique characteristic known as a "fingerprint", summarized in the sets of spectroscopic line parameters. At low pressure, absorption lines are affected only by the natural line broadening effect, this pressure range is called a natural line broadening regime or the Doppler regime. But at elevated pressures, the molecular spectra are mainly affected by collisional line broadening. This effect is modeled using coefficients calculated from the HWHM, pressure-induced line shifting, and Dicke narrowing effects. To model the acetylene spectra, we have used a multispectral fit software called Wproffit2. In the acetylene study we have used the Voigt (convolution of Doppler and Lorentzian line shape models) and the Hard collision (which takes into account the Dicke narrowing effect) line-shape models. We have taken into account the weak line mixing effects and modeled them together with N_2-broadening and N_2-shifting coefficients. For future study, it would be helpful to observe the line mixing coefficients at different temperature and pressure as well as the temperature dependencies. This may have a small effect on the retrieved broadening and shifting coefficient. A future analysis of broadening and shifting effects including line mixing would be very interesting as this will be the first experimental verification for this band of acetylene.

In the second spectroscopic study, we have investigated the $1\nu_2^l0 \leftarrow 0\nu_2^l0$ band system of the HCN emission spectra for $\nu_2 = 5$ and $l = 1, 5$. Using line intensities simulated from *ab initio* intensities [96], the wavelength dependent sensitivity of the apparatus was determined and the emission spectra have been calibrated using this calibration function [55]. For the intensities analysis of the $15^l0 \rightarrow 05^l0$ band, the transition dipole moments

squared and other parameters were in good agreement with the analysis of the *ab initio* data.

Bibliography

[1] C.P. Rinsland and L.L. Strow, Line Mixing Effects in Solar Occultation Spectra of the Lower Stratosphere - Measurements and Comparisons with Calculations for the 1932 cm^{-1} CO_2 Q Branch. Applied Optics, 1989. **28**(3): p. 457-464.

[2] D. Lambot, G. Blanquet, and J.P. Bouanich, Diode-Laser Measurements of Collisional Broadening in the V_5 Band of C_2H_2 Perturbed by O_2 and N_2. Journal of Molecular Spectroscopy, 1989. **136**(1): p. 86-92.

[3] D.H. Rank, D.P. Eastman, W.B. Birtley, and T.A. Wiggins, Shapes and Breadths of Some Molecular Rotation-Vibration Band Lines Perturbed by Rare Gases. Journal of Chemical Physics, 1960. **33**(2): p. 327-328.

[4] M. Herman, The Acetylene Ground State Saga. Molecular Physics, 2007. **105**(17-18): p. 2217-2241.

[5] J.P. Bouanich, G. Blanquet, J.C. Populaire, and J. Walrand, Nitrogen Broadening of Acetylene Lines in the ν_5 Band at Low Temperature. Journal of Molecular Spectroscopy, 1998. **190**(1): p. 7-14.

[6] J.P. Bouanich, G. Blanquet, and J. Walrand, Oxygen Broadening of Acetylene Lines in the ν_5 Band at Low Temperature. Journal of Molecular Spectroscopy, 1999. **194**(2): p. 269-277.

[7] P. Varanasi, Intensity and Linewidth Measurements in the 13.7 μm Fundamental Bands of $^{12}C_2H_2$ and $^{12}C^{13}CH_2$ at Planetary Atmospheric Temperatures. Journal of Quantitative Spectroscopy & Radiative Transfer, 1992. **47**(4): p. 263-274.

[8] D. Lambot, G. Blanquet, J. Walrand, and J.P. Bouanich, Diode-Laser Measurements of H_2-Broadening Coefficients in the ν_5-Band of C_2H_2. Journal of Molecular Spectroscopy, 1991. **150**(1): p. 164-172.

[9] W.E. Blass and V.W.L. Chin, Hydrogen and Nitrogen Broadening of the Lines of C_2H_2 at 14 μm. Journal of Quantitative Spectroscopy & Radiative Transfer, 1987. **38**(3): p. 185-188.

[10] N.T. Campbell, J.D. Cook, B.A. Coombs, E.P. Fuller, J.L. Hardwick, S.M. Hurley, L.K. Ho, P.A. Kovac, E.J. Robertson, E.N. Senning, J.K. Utterback, and R.S. Wiser, Temperature Dependence of Pressure Broadening and Shifts of Acetylene at 1550 nm by N-2. Molecular Physics, 2011. **109**(17-18): p. 2199-2208.

[11] G. Blanquet, J. Walrand, and J.P. Bouanich, Line-Mixing Effects in He- and N_2-Broadened Q Branches of C_2H_2 at Low Temperatures. Journal of Molecular Spectroscopy, 2001. **210**(1): p. 1-7.

[12] M. Dhyne, L. Fissiaux, J.C. Populaire, and M. Lepere, Temperature dependence of the N_2-broadening coefficients of acetylene. Journal of Quantitative Spectroscopy & Radiative Transfer, 2009. **110**(6-7): p. 358-366.

[13] P.F. Bernath, *Spectra of Atoms and Molecules* 1995, New York: Oxford University Press. 400.

[14] P. Varanasi and B.R.P. Bangaru, Intensity and Half-Width Measurements in the 1·525 μm Band of Acetylene. Journal of Quantitative Spectroscopy and Radiative Transfer, 1975. **15**(3): p. 267-273.

[15] D. Lambot, A. Olivier, G. Blanquet, J. Walrand, and J.P. Bouanich, Diode-Laser Measurements of Collisional Line Broadening in the Upsilon-5 Band of C_2H_2. Journal of Quantitative Spectroscopy & Radiative Transfer, 1991. **45**(3): p. 145-155.

[16] A.S. Pine, Self-Broadening, N_2-Broadening and Ar-Broadening and Line Mixing in HCN And C_2H_2. Journal of Quantitative Spectroscopy & Radiative Transfer, 1993. **50**(2): p. 149-166.

[17] P. Minutolo, C. Corsi, F. D'Amato, and M. De Rosa, Self- and Foreign-Broadening and Shift Coefficients for C_2H_2 lines at 1.54 μm. European Physical Journal D, 2001. **17**(2): p. 175-179.

[18] C. Povey, A. Predoi-Cross, and D.R. Hurtmans, Line Shape Study of Acetylene Transitions in the $\nu_1+\nu_2+\nu_4+\nu_5$ Band Over a Range of Temperatures. Journal of Molecular Spectroscopy, 2011. **268**(1-2): p. 177-188.

[19] J.P. Bouanich, D. Lambot, G. Blanquet, and J. Walrand, N_2-Broadening and O_2-Broadening Coefficients of C_2H_2 IR Lines. Journal of Molecular Spectroscopy, 1990. **140**(2): p. 195-213.

[20] A. Babay, M. Ibrahimi, V. Lemaire, B. Lemoine, F. Rohart, and J.P. Bouanich, Line Frequency Shifting in the ν_5 Band of C_2H_2. Journal of Quantitative Spectroscopy & Radiative Transfer, 1998. **59**(3-5): p. 195-202.

[21] J.P. Bouanich, G. Blanquet, and J. Walrand, Line-Mixing Effects in He- and N_2-Broadened $\Sigma <- \Pi$ Infrared Q Branches of C_2H_2. Journal of Molecular Spectroscopy, 2000. **203**(1): p. 41-48.

[22] V.M. Devi, D.C. Benner, C.P. Rinsland, M.A.H. Smith, and B.D. Sidney, Tunable Diode-Laser Measurements of N_2- and Air-Broadened Halfwidths - Lines in the $(\nu_4+\nu_5)^0$ Band of $^{12}C_2H_2$ near 7.4μm. Journal of Molecular Spectroscopy, 1985. **114**(1): p. 49-53.

[23] M. Dhyne, P. Joubert, J.C. Populaire, and M. Lepere, Collisional Broadening and Shift Coefficients of Lines in the $\nu_4+\nu_5$ Band of $^{12}C_2H_2$ Diluted in N_2 from Low to Room Temperatures. Journal of Quantitative Spectroscopy & Radiative Transfer, 2010. **111**(7-8): p. 973-989.

[24] S.W. Arteaga, C.M. Bejger, J.L. Gerecke, J.L. Hardwick, Z.T. Martin, J. Mayo, E.A. McIlhattan, J.M.F. Moreau, M.J. Pilkenton, M.J. Polston, B.T. Robertson, and E.N. Wolf, Line Broadening and Shift Coefficients of Acetylene at 1550 nm. Journal of Molecular Spectroscopy, 2007. **243**(2): p. 253-266.

[25] C.P. McRaven, M.J. Cich, G.V. Lopez, T.J. Sears, D. Hurtmans, and A.W. Mantz, Frequency Comb-Referenced Measurements of Self- and Nitrogen-Broadening in the $\nu_1+\nu_3$ Band of Acetylene. Journal of Molecular Spectroscopy, 2011. **266**(1): p. 43-51.

[26] H. Valipour and D. Zimmermann, Investigation of J Dependence of Line Shift, Line Broadening, and Line Narrowing Coefficients in the $\nu_1+3\nu_3$ Absorption Band of Acetylene. Journal of Chemical Physics, 2001. **114**(8): p. 3535-3545.

[27] D. Biswas, B. Ray, S. Dutta, and P.N. Ghosh, Diode Laser Spectroscopic Measurement of Line Shape of ($\nu_1+3\nu_3$) Band Transitions of Acetylene. Applied Physics B: Lasers and Optics, 1999. **68**(6): p. 1125-1130.

[28] G.C. Mellau, Highly Excited Rovibrational States of HNC. Journal of Molecular Spectroscopy, 2011. **269**(1): p. 77-85.

[29] J.M. Bowman, Chemistry - Beyond Platonic Molecules. Science, 2000. **290**(5492): p. 724-725.

[30] R.J. Barber, G.J. Harris, and J. Tennyson, Temperature Dependent Partition Functions and Equilibrium Constant for HCN and HNC. Journal of Chemical Physics, 2002. **117**(24): p. 11239-11243.

[31] A. Maki, W. Quapp, S. Klee, G.C. Mellau, and S. Albert, Infrared Transitions of $H^{12}C^{14}N$ and $H^{12}C^{15}N$ Between 500 and 10000 cm^{-1}. Journal of Molecular Spectroscopy, 1996. **180**(2): p. 323-336.

[32] A.G. Maki, G.C. Mellau, S. Klee, M. Winnewisser, and W. Quapp, High-Temperature Infrared Measurements in the Region of the Bending Fundamental of $H^{12}C14N$, $H^{12}C^{15}N$, and $H^{13}C^{14}N$. Journal of Molecular Spectroscopy, 2000. **202**(1): p. 67-82.

[33] J. M. Hollas, *Modern Spectroscopy* 2004, 4th edition, John Wiley & Sons, Ltd, The Atrium, Southern Gate, Chicheter, West Sussex PO19 8SQ, England

[34] W. Demtröder, *Laser Spectroscopy : Basic Principles*. 4th ed1989, Berlin: Springer-Verlag.

[35] N. Allard and J. Kielkopf, The Effect of Neutral Non-Resonant Collisions on Atomic Spectral-Lines. Reviews of Modern Physics, 1982. **54**(4): p. 1103-1182.

[36] P. Duggan, P.M. Sinclair, R. Berman, A.D. May, and J.R. Drummond, Testing Lineshape Models: Measurements for ν=1-0 CO Broadened by He and Ar. Journal of Molecular Spectroscopy, 1997. **186**(1): p. 90-98.

[37] R. H. Dicke, The Effect of Collisions Upon The Doppler Width of Spectral Lines. Physical Review, 1953. 89, 472-473.

[38] C. Povey, A. Predoi-Cross, and D. Hurtmans, Low-pressure line shape study of acetylene transitions in the $\nu_1+\nu_2+\nu_4+\nu_5$ band over a range of temperatures Molecular Physics. 2012. **110**(21-22): p. 2633-44

[39] P.R. Berman, Speed-Dependent Collisional Width and Shift Parameters in Spectral Profiles. Journal of Quantitative Spectroscopy & Radiative Transfer, 1972. **12**, 1331-&.

[40] V.M. Devi, D.C. Benner, L.R. Brown, C.E. Miller, R.A. Toth, Line mixing and speed dependence in CO2 at 6348 cm(-1): Positions, intensities, and air- and selfbroadening derived with constrained multispectrum analysis. Journal of Molecular Spectroscopy 242, 90-117 (2007).

[41] V.M. Devi, D.C. Benner, L.R. Brown, C.E. Miller, R.A. Toth, Line mixing and speed dependence in CO2 at 6227.9 cm(-1) Constrained multispectrum analysis of intensities and line shapes in the 30013 <- 00001 band. Journal of Molecular Spectroscopy 245, 52-80 (2007).

[42] G. Birnbaum, Microwave Pressure Broadening and Its Application to Intermolecular Forces. Advances in Chemical Physics: Intermolecular Forces, Volume 12 487-548 (2007).

[43] J. Bonamy, D. Robert, and C. Boulet, Simplified Models for the Temperature-Dependence of Linewidths at Elevated-Temperatures and Applications to CO Broadened By Ar and N_2. Journal of Quantitative Spectroscopy & Radiative Transfer, 1984. **31**(1): p. 23-34.

[44] T. Nakazawa and M. Tanaka, Intensities, Half-Widths and Shapes of Spectral-Lines in the Fundamental-Band of CO at Low-Temperatures. Journal of Quantitative Spectroscopy & Radiative Transfer, 1982. **28**(6): p. 471-480.

[45] T. Drascher, T.F. Giesen, T.Y. Wang, N. Schmucker, R. Schieder, G. Winnewisser, P. Joubert, and J. Bonamy, Temperature-Dependent Line Shift and Broadening of CO Infrared Transitions. Journal of Molecular Spectroscopy, 1998. **192**(2): p. 268-276.

[46] M.F. Lemoal and F. Severin, N_2 and H_2 Broadening Parameters in the Fundamental-Band of CO. Journal of Quantitative Spectroscopy & Radiative Transfer, 1986. **35**(2): p. 145-152.

[47] A. Predoi-Cross, C. Hnatovsky, K. Strong, J.R. Drummond, and D.C. Benner, Temperature Dependence of Self- and N_2-Broadening and Pressure-Induced Shifts in the 3 <– 0 band of CO. Journal of Molecular Structure, 2004. **695**: p. 269-286.

[48] A. Predoi-Cross, A.R.W. McKellar, D.C. Benner, V.M. Devi, R.R. Gamache, C.E. Miller, R.A. Toth, L.R. Brown, Temperature dependences for air-broadened Lorentz half-width and pressure shift coefficients in the 30013 <- 00001 and 30012 <-00001 bands of CO2 near 1600 nm. Canadian Journal of Physics, 2009 87, 517-535.

[49] C. Povey, *High resolution spectroscopy and applications*, Department of Physics and Astronomy 2013, University of Lethbridge.

[50] N.B. Colthup, Daly, L. H., Wiberley, S. E., *Introduction to Infrared and Raman Spectroscopy* 1964, (3rd print 1968). New York: Academic Press Inc.

[51] W. Quapp, M. Hirsch, G.C. Mellau, S. Klee, M. Winnewisser, and A. Maki, Climbing the Bending Vibrational Ladder in $D^{13}C^{15}N$ by Hot Gas Emission Spectroscopy. Journal of Molecular Spectroscopy, 1999. **195**(2): p. 284-298.

[52] R.R. Gamache and L.S. Rothman, Extension of the HITRAN Database to Non-LTE Applications. Journal of Quantitative Spectroscopy & Radiative Transfer, 1992. **48**(5-6): p. 519-525.

[53] M. Simeckova, D. Jacquemart, L.S. Rothman, R.R. Gamache, and A. Goldman, Einstein A-Coefficients and Statistical Weights for Molecular Absorption Transitions in the HITRAN Database. Journal of Quantitative Spectroscopy & Radiative Transfer, 2006. **98**(1): p. 130-155.

[54] L.S. Rothman, C.P. Rinsland, A. Goldman, S.T. Massie, D.P. Edwards, J.M. Flaud, A. Perrin, C. Camy-Peyret, V. Dana, J.Y. Mandin, J. Schroeder, A. McCann, R.R. Gamache, R.B. Wattson, K. Yoshino, K.V. Chance, K.W. Jucks, L.R. Brown, V. Nemtchinov, and P. Varanasi, The HITRAN Molecular Spectroscopic Database and HAWKS (HITRAN Atmospheric Workstation): 1996 Edition. Journal of Quantitative Spectroscopy & Radiative Transfer, 1998. **60**(5): p. 665-710.

[55] J. Schostag, *Intensity Analysis of Transitions Between Highly Excited Rovibrational States, in physical chemistry* 2011, Justus-Liebig-University Gießen.

[56] R. Herman and R.F. Wallis, Influence of Vibration-Rotation Interaction on Line Intensities in Vibration-Rotation Bands of Diatomic Molecules. Journal of Chemical Physics, 1955. **23**(4): p. 637-646.

[57] J.K.G. Watson, Quadratic Herman-Wallis Factors in the Fundamental Bands of Linear-Molecules. Journal of Molecular Spectroscopy, 1987. **125**(2): p. 428-441.

[58] A. Maki, W. Quapp, and S. Klee, Intensities of Hot-Band Transitions - HCN Hot Bands. Journal of Molecular Spectroscopy, 1995. **171**(2): p. 420-434.

[59] J.C. Grecu, B.P. Winnewisser, and M. Winnewisser, Absolute Rovibrational Line-Intensities in the ν_5 Band System of Cyanogen, *NCCN*. Journal of Molecular Spectroscopy, 1993. **159**(2): p. 551-571.

[60] JENSEN., P., Theroretische Spektroskopie1995.

[61] I.W.M. Smith, Integrated-Intensities for Some Infrared-Absorption Bands of HCN. Journal of the Chemical Society-Faraday Transactions Ii, 1981. **77**: p. 2357-2363.

[62] K.N. Rao, Molecular Spectroscopy: Modern Research III.1985: Academic Press.

[63] D. Mondelain, C. Camy-Peyret, A.W. Mantz, E. Tang, and A. Valentin, Performance of a Herriott cell, Designed for Variable Temperatures Between 296 and 20 K. Journal of Molecular Spectroscopy, 2007. **241**(1): p. 18-25.

[64] Z. El Helou, B. Erba, S. Churassy, G. Wannous, M. Neri, R. Bacis, and E. Boursey, Design and Performance of a Low-Temperature-Multi-Pass-Cell for Absorbance Measurements of Atmospheric Gases. Application to Ozone. Journal of Quantitative Spectroscopy & Radiative Transfer, 2006. **101**(1): p. 119-128.

[65] D. Lambot, J.C. Populaire, J. Walrand, G. Blanquet, and J.P. Bouanich, Diode-Laser Measurements of Self-Broadening Coefficients in the ν_5-Band of C_2H_2 at Low-Temperature. Journal of Molecular Spectroscopy, 1994. **165**(1): p. 1-11.

[66] D. Jacquemart, J.Y. Mandin, V. Dana, L. Regalia-Jarlot, X. Thomas, and P. Von der Heyden, Multispectrum Fitting Measurements of Line Parameters for 5 μm Cold Bands of Acetylene. Journal of Quantitative Spectroscopy & Radiative Transfer, 2002. **75**(4): p. 397-422.

[67] A.R.W. McKellar, Long-Path Equilibrium IR-Spectra of Weakly-Bound Complexes at Low-Temperatures. Faraday Discussions, 1994. **97**: p. 69-80.

[68] A.R.W. McKellar, J.K.G. Watson, and B.J. Howard, The No Dimer - N-15 Isotopic Infrared-Spectra, Line-Widths, and Force-Field. Molecular Physics, 1995. **86**(2): p. 273-286.

[69] J. Ballard, K. Strong, J.J. Remedios, M. Page, and W.B. Johnston, A Coolable Long Path Absorption Cell for Laboratory Spectroscopic Studies of Gases. Journal of Quantitative Spectroscopy & Radiative Transfer, 1994. **52**(5): p. 677-691.

[70] R.A. McPheat, D.A. Newnham, R.G. Williams, and J. Ballard, Large-Volume, Coolable Spectroscopic Cell for Aerosol Studies. Applied Optics, 2001. **40**(36): p. 6581-6586.

[71] A. Valentin, A. Henry, C. Claveau, C. Camy-Peyret, D. Hurtmans, and A.W. Mantz, Development of a stabilized low temperature infrared absorption cell for use in low temperature and collisional cooling experiments. Spectrochimica Acta Part a-Molecular and Biomolecular Spectroscopy, 2004. **60**(14): p. 3477-3482.

[72] V.S.I. Sprakel, M.C. Feiters, R.J.M. Nolte, P. Hombergen, A. Groenen, and H.J.R. De Haas, A Cell for Combined UV-Visible and X-Ray Absorption Spectroscopy Studies Under Low-Temperature and Air Exclusion Conditions. Review of Scientific Instruments, 2002. **73**(8): p. 2994-2998.

[73] R.D. Schaeffer, J.C. Sproul, J. Oconnell, C. Vanvloten, and A.W. Mantz, Multipass Absorption Cell Designed for High-Temperature UHV Operation. Applied Optics, 1989. **28**(9): p. 1710-1713.

[74] M.A.H. Smith, C.P. Rinsland, V.M. Devi, and D.C. Benner, Temperature-Dependence of Broadening and Shifts of Methane Lines in the ν_4 Band. Spectrochimica Acta Part a-Molecular and Biomolecular Spectroscopy, 1992. **48**(9): p. 1257-1272.

[75] M.W.P. Cann, An Optical Absorption Cell with Variable Path Length and Temperature. Review of Scientific Instruments, 1969. **40**(4): p. 595-&.

[76] R.E. Shetter, J.A. Davidson, C.A. Cantrell, and J.G. Calvert, Temperature Variable Long Path Cell for Absorption-Measurements. Review of Scientific Instruments, 1987. **58**(8): p. 1427-1428.

[77] L.S. Rothman, I.E. Gordon, A. Barbe, D.C. Benner, P.E. Bernath, M. Birk, V. Boudon, L.R. Brown, A. Campargue, J.P. Champion, K. Chance, L.H. Coudert, V. Dana, V.M. Devi, S. Fally, J.M. Flaud, R.R. Gamache, A. Goldman, D. Jacquemart, I. Kleiner, N. Lacome, W.J. Lafferty, J.Y. Mandin, S.T. Massie, S.N. Mikhailenko, C.E. Miller, N. Moazzen-Ahmadi, O.V. Naumenko, A.V. Nikitin, J. Orphal, V.I. Perevalov, A. Perrin, A. Predoi-Cross, C.P. Rinsland, M. Rotger, M. Simeckova, M.A.H. Smith, K. Sung, S.A. Tashkun, J. Tennyson, R.A. Toth, A.C. Vandaele, and J. Vander Auwera, The HITRAN 2008 Molecular Spectroscopic Database. Journal of Quantitative Spectroscopy & Radiative Transfer, 2009. **110**(9-10): p. 533-572.

[78] A.A. Madej, A.J. Alcock, A. Czajkowski, J.E. Bernard, and S. Chepurov, Accurate Absolute Reference Frequencies from 1511 to 1545 nm of the $\nu_1+\nu_3$ Band of $^{12}C_2H_2$ Determined with Laser Frequency Comb Interval Measurements. Journal of the Optical Society of America B-Optical Physics, 2006. **23**(10): p. 2200-2208.

[79] D. Hurtmans, G. Dufour, W. Bell, A. Henry, A. Valentin, and C. Camy-Peyret, Line Intensity of R(0) and R(3) of the $^{12}CH_4$ $2\nu_3$ Band from Diode Laser Spectroscopy. Journal of Molecular Spectroscopy, 2002. **215**(1): p. 128-133.

[80] A. Predoi-Cross, E. Jonson, D. Hemsing, H. Rozario and Georg Ch. Mellau, Climbing up the vibrational ladder of $HC^{15}N$: High-temperature near-infrared emission measurements. Journal of Molecular Spectroscopy, 2013. **293-294**: p. 27-32.

[81] G.C. Mellau, Complete Experimental Rovibrational Eigenenergies of HCN up to 6880 cm^{-1} Above the Ground State. Journal of Chemical Physics, 2011. **134**(23).

[82] A. Maki, W. Quapp, S. Klee, G.C. Mellau, and S. Albert, The CN Mode of HCN: A Comparative Study of the Variation of the Transition Dipole and Herman-Wallis Constants for Seven Isotopomers and the Influence of Vibration-Rotation Interaction. Journal of Molecular Spectroscopy, 1995. **174**(2): p. 365-378.

[83] G.C. Mellau, *Fourier-Transform-Spektroskopie and HCN: Beobachtung und Interpretation neuer Infrarotübergänge zwischen hochangeregten Zuständen.*, 2003, Justus-Liebig-University: Gießen.

[84] H. Rozario, J. Garber, C. Povey, D. Hurtmans, J. Buldyreva and A. Predoi-Cross Experimental and theoretical study of N_2-broadened acetylene line parameters in the $\nu_1+\nu_3$ band over a range of temperatures. Molecular Physics. 2012. **110**(21-22): p. 2645-63.

[85] L. Fissiaux, M. Dhyne, and M. Lepère, Diode-Laser Spectroscopy: Pressure Dependence of N_2-Broadening Coefficients of Lines in the Band of C_2H_2. Journal of Molecular Spectroscopy, 2009. **254**(1): p. 10-15.

[86] J. Buldyreva, J. Bonamy, M.C. Weikl, F. Beyrau, T. Seeger, A. Leipertz, F. Vestin, M. Afzelius, J. Bood, and P.E. Bengtsson, Linewidth Modelling of C_2H_2-N_2 Mixtures Tested by Rotational CARS Measurements. Journal of Raman Spectroscopy, 2006. **37**(6): p. 647-654.

[87] D. Jacquemart, A. Laraia, F.K. Tchana, R.R. Gamache, A. Perrin, and N. Lacome, Formaldehyde Around 3.5 and 5.7 μm: Measurement and Calculation of Broadening Coefficients. Journal of Quantitative Spectroscopy & Radiative Transfer, 2010. **111**(9): p. 1209-1222.

[88] D. Robert and J. Bonamy, Short-Range Force Effects in Semi-Classical Molecular Line Broadening Calculations. Journal De Physique, 1979. **40**(10): p. 923-943.

[89] L.D. Landau and E.M. Lifshits, *Course of Theoretical Physics v.1 Mechanics* 1976: Pergamon, Oxford.

[90] F. Thibault, B. Corretja, A. Viel, D. Bermejo, R.Z. Martinez, and B. Bussery-Honvault, Linewidths of C_2H_2 Perturbed by H_2: Experiments and Calculations from

an ab initio Potential. Physical Chemistry Chemical Physics, 2008. **10**(35): p. 5419-5428.

[91] J. Buldyreva and L. Nguyen, Extension of the Exact Trajectory Model to the Case of Asymmetric Tops and its Application to Infrared Nitrogen-Broadened Linewidths of Ethylene. Physical Review A, 2008. **77**(4).

[92] D.E. Stogryn and A.P. Stogryn, Molecular Multipole Moments. Molecular Physics, 1966. **11**(4): p. 371-&.

[93] H. Yasuda and T. Yamamoto, 2-Center Expansion of an Arbitrary Function. Progress of Theoretical Physics, *1*971. **45**(5): p. 1458-&.

[94] W.H. Flygare and R.C. Benson, Molecular Zeeman Effect in Diamagnetic Molecules and Determination of Molecular Magnetic Moments (G-Values), Magnetic Susceptibilities, and Molecular Quadrupole Moments. Molecular Physics, 1971. **20**(2): p. 225-&.

[95] G.Ch. Mellau, B. P. Winnewisser, and M. Winnewisser, Near infrared emission spectrum of HCN. Journal of Molecular Spectroscopy, 2007. **249**(1): p. 23-42.

[96] G.J. Harris, O.L. Polyansky, and J. Tennyson, Ab initio Rotation-Vibration Spectra of HCN and HNC. Spectrochimica Acta Part a-Molecular and Biomolecular Spectroscopy, 2002. **58**(4): p. 673-690.

Appendix A

Table A.1: Character table

$C_{\infty v}$	I	$2C_{\infty}^{\phi}$	…	$\infty\sigma_v$		
$A_1 \equiv \Sigma^+$	1	1	…	1	T_z	$\alpha_{xx}+\alpha_{yy}, \alpha_{zz}$
$A_2 \equiv \Sigma^-$	1	1	…	-1	R_z	
$E_1 \equiv \Pi$	2	$2\cos\phi$	…	0	$(T_x, T_y), (R_x, R_y)$	α_{xz}, α_{yz}
$E_2 \equiv \Delta$	2	$2\cos 2\phi$	…	0		$\alpha_{xx}-\alpha_{yy}, \alpha_{xy}$
$E_1 \equiv \Phi$	3	$2\cos 3\phi$	…	0		
⋮	⋮	⋮	…	⋮		